Investigating structural network disruption in multiple sclerosis

Thalis Charalambous

Thesis presented for the degree of

Doctor of Philosophy

of the

University College London

Department of Neuroinflammation

Queen Square Multiple Sclerosis Centre

Institute of Neurology

University College London

I, Thalis Charalambous, confirm that the work presented in this thesis is my own. Where information has been derived from other sources, I confirm that this has been indicated in the thesis.

_____

Abstract

Multiple sclerosis (MS) is an inflammatory, demyelinating and neurodegenerative disease of the central nervous system (CNS). Conventional whole brain magnetic resonance imaging (MRI) measures do not sufficiently explain disability in MS. Network science provides a powerful approach to study brain organizational principles and in combination with graph theory has revealed fundamental connectivity patterns in neurological conditions including MS.

The overarching aim of this thesis is to investigate structural network disruption in MS evaluating the potential of brain networks analyses as novel biomarkers in MS pathology.

The results of this thesis add to the current scientific knowledge. In particular, by applying an optimised structural network reconstruction pipeline we demonstrated that network metrics explain disability better in MS over and above conventional non-network metrics. In addition, in the absence of any longitudinal network studies, we developed a longitudinal network pipeline which we then applied to our longitudinal data. These findings demonstrated for the first time that baseline structural network metrics are predictors of future deep grey matter atrophy and increased lesion load. Finally, we applied a data-driven network decomposition approach detecting progressive weakening of connections that is linked to the severity of MS subtypes suggesting that these techniques are sensitive to pathology.

The results presented here highlight the potential of network-based approaches as complementary methods for disease biomarkers to better predict disease course and monitor treatment effects. We believe that these findings may provide a framework for future studies with the aim to bridge the gap between imaging and symptomatology.

Impact Statement

Conventional magnetic resonance imaging (MRI) measures do not sufficiently explain disability in multiple sclerosis (MS). This condition is characterised by focal and widespread pathology and it is the leading cause of chronic neurological disability in young adults. MRI-derived network-based measures provide an integrative framework to gain new insights into pathological processes. However, there is no standard pipeline to reconstruct a structural brain network as methods to map the human brain are still in their infancy.

The methodological work presented here can pave the way for future applications in academia. We developed and optimised a structural network reconstruction pipeline applying the latest methodological techniques that resulted in a robust and biologically plausible brain network. These results make the methods section of a currently under review revised paper in the *Journal of Neurology, Neurosurgery and Psychiatry (JNNP)*. Although this work has focused on MS, the fact that it yields at a network which is biologically relevant constitutes this pipeline transferrable across neurological diseases including Alzheimer's, Parkinson's and Frontotemporal dementia. Moreover, there have been hitherto limited longitudinal structural network studies and none in MS. Therefore, in collaboration with the Translational Imaging Group (TIG), Centre for Medical Image Computing (CMIC) at University College London (UCL), we extended our optimised pipeline to accommodate brain structural investigations with more than one time-point. This work has been peer reviewed and published as a book chapter in *Computational Diffusion MRI* (2017). With the increasing need for longitudinal studies to gain insights into network dynamics and how these are affected in pathology, we anticipate that this framework will have a wide range of application not only in MS but also in many neurological conditions with longitudinal data.

The use of data from people with MS in our studies strengthens the likelihood of our findings being translatable into future clinical practice to help understand disease neurobiology, inform prognosis and develop imaging biomarkers to monitor therapies. We demonstrated distinct network organisation in a cohort with various MS subtypes; results to be submitted for publication in the *Multiple Sclerosis Journal (MSJ)*. We also showed for the first time that network metrics explain disability better than non-network metrics such as lesion load and tissue atrophy. These results are currently under review in the *Journal of Neurology, Neurosurgery and Psychiatry* (*JNNP).* Additionally, network metrics can predict future tissue damage either at the macroscopic level (increased lesion volume), or at the microscopic level causing deep grey matter volume loss. These findings will be submitted to *Human Brain Mapping (HBM)* journal for publication. Collectively, all of the above results highlight the clinical importance of network analysis and the potential of network metrics as outcome measures for disease diagnosis, prognosis and for assessing treatment effects in clinical trials.

To conclude, this multidisciplinary translational research spanned across computer and medical sciences and developed techniques that are transferrable across neurological disorders. Additionally, our findings extend our current scientific knowledge, they will result in four first-author publications and could help to inform future clinical practice.

Αφιερωμένο στη γιαγιά Ηλέκτρα (1940–2014)

'Σοφώτατον χρόνος· ἀνευρίσκει γὰρ πάντα'

--- Θαλής ο Μιλήσιος ---

Acknowledgments

I would like to express my deep gratitude to my supervisors and mentors Professor Alan Thompson, Dr. Ahmed Toosy, Professor Claudia Wheeler-Kinsghott and Dr. Jonathan Clayden for their constant and unconditional support. When it comes to multidisciplinary studies there are not enough words that can describe and acknowledge the time and effort that experts of the multiple disciplines put together to achieve a shared goal. I, personally, had the honour to be mentored by the best:

Professor Alan Thompson, an inspiring clinician and scientist with his contribution to multiple sclerosis being well recognised that I had the privilege to have as a supervisor and as a mentor in particular.

Dr. Ahmed Toosy, always supportive and encouraging even when things were not working as expected. Your clinical approach to the project was motivating not only for this thesis but also for future aspirations.

Professor Claudia Wheeler-Kingshott, a world leader in MR physics, who I consider myself lucky to have as a supervisor. Your insights into MR physics are truly invaluable while your positive outlook gave me the confidence to produce this thesis.

Dr. Jonathan Clayden, a world expert in diffusion MRI and connectivity analysis with excellent programming/technical skills; they have all been critical components for the success of this thesis. I have benefited from your advice particularly when exploring new techniques.

Thank you all for your endless time, support and guidance.

There are some people without whom this thesis would have not been possible. I would like to thank Professor David Miller and Dr. Declan Chard for providing the MRI data, Dr. Carmen Tur for her continuous support, advice and assistance in the statistical analysis, Dr. Ferran Prados for his help with image analysis and registration processes, Dr. Baris Kanber for his help on XNAT and Elizabeth Powell for her help on the connectivity analysis.

I would like to thank the members of the Physics team who accepted me in their group (despite my non-Physics background) and patiently eased me into the amazing world of MRI. Special thanks to Dr. Marco Battiston for the various conversations about things that “matter” when there was “absolutely nothing”. I would also like to thank Dr. Rebecca Samson for her help/tips regarding (non)science topics, Dr. Francesco Grussu also known as the diffusion expert, Dr. Adnan Alahmadi with his fMRI persuasion strategy, Dr. Arman Eshaghi, the machine learning expert and finally our radiographer Dr. Marios Yiannakas. Our discussions over meetings and beers were very much appreciated.

Thanks to everyone in Queen Square Multiple Sclerosis Research Centre for making the office such a supportive working environment over the last few years.

Thanks to Leonard Wolfson Experimental Neurology Centre for funding me.

Thanks to Elizbeth Halton for helping with travel expenses and administrative tasks.

I would also like to thank Sophia Sklavounos for her endless patience and support throughout this time. She was there during the ups and downs, listening carefully to random thoughts and structured presentations. Indeed, “high global efficiency is a characteristic of intact structural connectivity”. Thank you, Sophia.

I would like to conclude thanking my family: my father Andreas, my mother Olya and my brothers Christofis and Kypros. Although in different counties, they all made sure that the distance was never an obstacle to show their unconditional love and support which meant a lot to me during my time in London. Blessed to have you all.

Κλείνοντας και λίγα λόγια στα Ελληνικά για κάποιους ξεχωριστούς ανθρώπους. Θέλω να ευχαριστήσω την οικογένεια μου για την ανελλιπή αγάπη και στήριξη καθόλη τη διάρκεια όχι μόνο του διδακτορικού αλλά και της διαμονής μου στο Λονδίνο. Αυτό το έργο είναι το επιστέγασμα των δικών σας προσπαθειών. Πατέρα, μητέρα, Χριστοφή και Κύπρο αισθάνομαι τυχερός που σας έχω δίπλα μου. Σας ευχαριστώ για όλα.

9th August 2018, London

Thalis Charalambous

᾽***Γηράσκω δ' αἰεὶ πολλά διδασκόμενος***᾽

--- Σόλων ο Αθηναίος ---

Tables of contents

List of figures

List of tables

List of abbreviations

ACT	Anatomically constrained tractography
ADC	Apparent diffusion coefficient
CGM	Cortical grey matter
CIS	Clinically isolated syndrome
CNS	Central nervous system
CSD	Constrained spherical deconvolution
CSF	Cerebrospinal fluid
DGM	Deep grey matter
DTI	Diffusion tensor imaging
DWI	Diffusion-weighted imaging
ED	Edge density
EDSS	Expanded disability status scale
EPI	Echo planar imaging
FA	Fractional anisotropy
FLAIR	Fluid attenuated inversion recovery
FOD	Fibre orientation distribution
GE	Global efficiency
GIF	Geodesic Information Flows
GM	Grey matter
HARDI	High angular resolution diffusion-weighted imaging
HC	Healthy controls

HLA	Human leucocyte antigen
IR	Inversion recovery
IL	Interleukin
LL	Lesion load
mCC	Mean clustering coefficient
mLE	Mean local efficiency
MRI	Magnetic resonance imaging
MS	Multiple sclerosis
MTR	Magnetization transfer ratio
NAWM	Normal appearing white matter
NABV	Normal appearing brain volume
PPMS	Primary progressive multiple sclerosis
PSIR	Phase sensitive inversion recovery
RF	Radio-frequency
ROI	Region of interest
RRMS	Relapsing remitting multiple sclerosis
SE	Spin echo
SDMT	Symbol digit modalities test
SIFT	Spherical-deconvolution informed filtering of tractograms
SPMS	Secondary progressive multiple sclerosis
TDI	Track density imaging
TI	Inversion time
TR	Repetition time
WM	White matter

List of publications

Journal publications

Charalambous Thalis, Carmen Tur, Ferran Prados, Baris Kanber, Declan Chard, Sebastien Ourselin, Jonathan Clayden, Claudia Wheeler-Kingshott, Alan Thompson, Ahmed Toosy. **Network disruption explains disability in multiple sclerosis.** [revised manuscript under review in *Journal of Neurology, Neurosurgery and Psychiatry*].

Charalambous Thalis, Carmen Tur, Elizabeth Powell, Ferran Prados, Baris Kanber, Declan Chard, Sebastien Ourselin, Jonathan Clayden, Claudia Wheeler-Kingshott, Alan Thompson, Ahmed Toosy. **Baseline whole brain network measures predict future volumetric changes in multiple sclerosis.** [in preparation to be submitted in *Human Brain Mapping*].

Charalambous Thalis, Elizabeth Powell, Jonathan Clayden, Ferran Prados, Carmen Tur, Baris Kanber, Declan Chard, Sebastien Ourselin, Claudia Wheeler-Kingshott, Alan Thompson, Ahmed Toosy. **Distinct topological organisation of structural brain networks in multiple sclerosis.** [in preparation to be submitted in *Multiple Sclerosis Journal*].

Tur Carmen, Arman Eshaghi, Daniel Altmann, Tom Jenkins, Ferran Prados, Francesco Grussu, Thalis **Charalambous**, Sebastien Ourselin, Jonathan Clayden, Claudia Wheeler-Kingshott, David Miller, Alan Thompson, Olga Ciccarelli, Ahmed

Toosy. **Structural cortical network reorganization associated with early conversion to multiple sclerosis.** 2018. *Scientific reports.*

Tur Carmen, Francesco Grussu, Ferran Prados, Thalis **Charalambous**, Sara Collorone, Baris Kanber, Niamh Cawley, Daniel R Altmann, Sebastien Ourselin, Frederik Barkhof, Jonathan D Clayden, Ahmed T Toosy, Claudia A Gandini Wheeler-Kingshott, Olga Ciccarelli. **Experimental considerations for clinically feasible diffusion-based connectivity and microstructural assessments in multiple sclerosis.** [in preparation to be submitted in *Annals of Clinical and Translational Neurology*].

Review papers

Declan Chard, Adnan Alahmadi, Bertrand Audoin, Thalis **Charalambous**, Christien Enzinger, Hanneke Hulst, Mara Rocca, Alex Rovira, Jaume Sastre-Garriga, Betty Tijms, Carmen Tur, Claudia Wheeler-Kingshott, Alle-Meije Wink, Olga Ciccarelli, Frederik Barkhof on behalf of MAGNIMS. **Mind the gap: From neurons to networks to outcomes in multiple sclerosis.** [in preparation to be submitted in *Lancet* review]

- Invited speaker in MAGNIMS meeting (European network of academics that share a common interest in the study of multiple sclerosis using magnetic resonance imaging techniques)

Book chapters

Charalambous Thalis, Ferran Prados, Carmen Tur, Baris Kanber, Declan Chard, Sebastien Ourselin, Jonathan Clayden, Claudia Wheeler-Kingshott, Alan Thompson, Ahmed Toosy. **Longitudinal analysis framework of DWI data for reconstructing structural brain networks with application to multiple sclerosis**. *Computational Diffusion MRI (2017)*

Conference abstracts

Charalambous Thalis, Elizabeth Powell, Jonathan Clayden, Ferran Prados, Carmen Tur, Baris Kanber, Declan Chard, Sebastien Ourselin, Claudia Wheeler-Kingshott, Alan Thompson, Ahmed Toosy. **Differential topological organisation of brain networks in multiple sclerosis.** *OHBM (2018), Singapore*

Charalambous Thalis, Carmen Tur, Ferran Prados, Baris Kanber, Declan Chard, Sebastien Ourselin, Jonathan Clayden, Claudia Wheeler-Kingshott, Alan Thompson, Ahmed Toosy. **The clinical relevance of the network-derived metrics in multiple sclerosis**. *33nd conference of ECTRIMS (2017)*, Paris, France

Charalambous Thalis, Carmen Tur, Ferran Prados, Baris Kanber, Declan Chard, Sebastien Ourselin, Jonathan Clayden, Claudia Wheeler-Kingshott, Alan Thompson, Ahmed Toosy. **The relationship between network measures and magnetic resonance imaging metrics in multiple sclerosis**. *33nd conference of ECTRIMS (2017)*, Paris, France

Ooi Joshua, Francesco Grussu, Sara Collorone, Thalis **Charalambous**, Ferran Prados, Baris Kanber, Sebastien Ourselin, Ahmed Toosy, Claudia Wheeler-Kingshott, Olga Ciccarelli, Carmen Tur. **Brain network organisation and cognitive performance in the clinically isolated syndromes.** *33nd conference of ECTRIMS (2017)*, Paris, France

Charalambous Thalis, Carmen Tur, Ferran Prados, Steven van de Pavert, Declan Chard, David Miller, Sebastien Ourselin, Jonathan Clayden, Claudia Wheeler-Kingshott, Alan Thompson, Ahmed Toosy. **Graph theoretical measures predict volumetric changes in multiple sclerosis**. *Proceedings of 25th Annual Meeting of ISMRM (2017)*, Honolulu, USA

Tur Carmen, Francesco Grussu, Ferran Prados, Thalis **Charalambous**, Sara Collorone, Niamh Cawley, Baris Kanber, Daniel R Altmann, Sébastien Ourselin, Frederik Barkhof, Jonathan D Clayden, Ahmed T Toosy, Claudia AM Gandini Wheeler-Kingshott, Olga Ciccarelli**. Impact of acquisition strategies and spherical deconvolution algorithms on brain connectivity mapping in early multiple sclerosis.** *Proceedings of 25th Annual Meeting of ISMRM (2017)*, Honolulu, USA

Powell Elizbeth, Thalis **Charalambous**, Ferran Prados, Tur Carmen, Daniel Altman, Declan Chard, Sebastien Ourselin, Ahmed Toosy, Jonathan Clayden, Claudia Wheeler-Kingshott. **The role of node strength in investigating pathology**. *Proceedings of 25th Annual Meeting of ISMRM (2017)*, Honolulu, USA

Charalambous Thalis, Carmen Tur, Jonathan Clayden, Ferran Prados, Steven van de Pavert, Declan Chard, David Miller, Claudia Wheeler-Kingshott, Alan Thompson, Ahmed Toosy **Changes in diffusion-based structural network in relapsing-remitting multiple sclerosis.** *32nd conference of ECTRIMS (2016)*, London, UK

Tur Carmen, Arman Eshaghi, Tom Jenkins, Daniel Altmann, Ferran Prados, Thalis **Charalambous**, Jonathan Clayden, Sebastien Ourselin, Claudia Wheeler-Kingshott, David Miller, Alan Thompson, Olga Ciccarelli, Ahmed Toosy. **Structural cortical networks in optic neuritis (early CIS).** *32nd conference of ECTRIMS (2016)*, London, UK

Tur Carmen, Arman Eshaghi, Zhaleh Khaleeli, Daniel Altmann, Ferran Prados, Thalis **Charalambous**, Jonathan Clayden, Sebastien Ourselin, Claudia Wheeler-Kingshott, David Miller, Alan Thompson, Ahmed Toosy, Olga Ciccarelli. **Longitudinal changes in structural cortical networks in early PPMS.** *32nd conference of ECTRIMS (2016)*, London, UK

Chapter 1

1. Introduction

1.1. Problem statement

Multiple sclerosis (MS) is an inflammatory, demyelinating and neurodegenerative disease of the central nervous system (CNS). It is the most common cause of neurological disability in young adults, yet its cause and the mechanisms of the underlying long-term disability remain uncertain. Magnetic resonance imaging (MRI) is now established as a key tool in diagnosing and monitoring MS. Conventional MRI techniques such as detection of number and volume of white matter (WM) lesions and reduced brain volume (atrophy) are useful outcome measures, but alone do not capture the widespread effects of MS pathology, and explain disability only moderately.

1.2. Aims

The interplay between inflammation, demyelination and neurodegeneration necessitates the application of more advanced techniques that could integrate these pathological features and better predict disease course and monitor treatment effects. One proposed method is network analysis, which provides a framework to study whole brain connectivity patterns and their disruptions, incorporating data beyond focal pathology. Network analysis has been recently applied to many neurological disorders including MS, revealing some common organisational and connectivity patterns. This supports the potential that such an approach might hold, which we further sought to explore in this thesis. Therefore, the overarching aim of this work was to investigate structural network disruption in MS (taking into consideration the different disease

subtypes), evaluating the potential of structural brain network analyses as new biomarkers in MS pathology. Our specific aims are:

1. to develop and validate a structural network analysis pipeline
2. to evaluate whether structural network metrics can explain disability better than conventional imaging measures
3. to propose and validate a longitudinal network analysis pipeline
4. to assess whether baseline structural network metrics can predict future volumetric changes
5. to investigate the effect of pathology on key subnetworks applying a novel data-driven network decomposition method

1.3. Remaining thesis structure

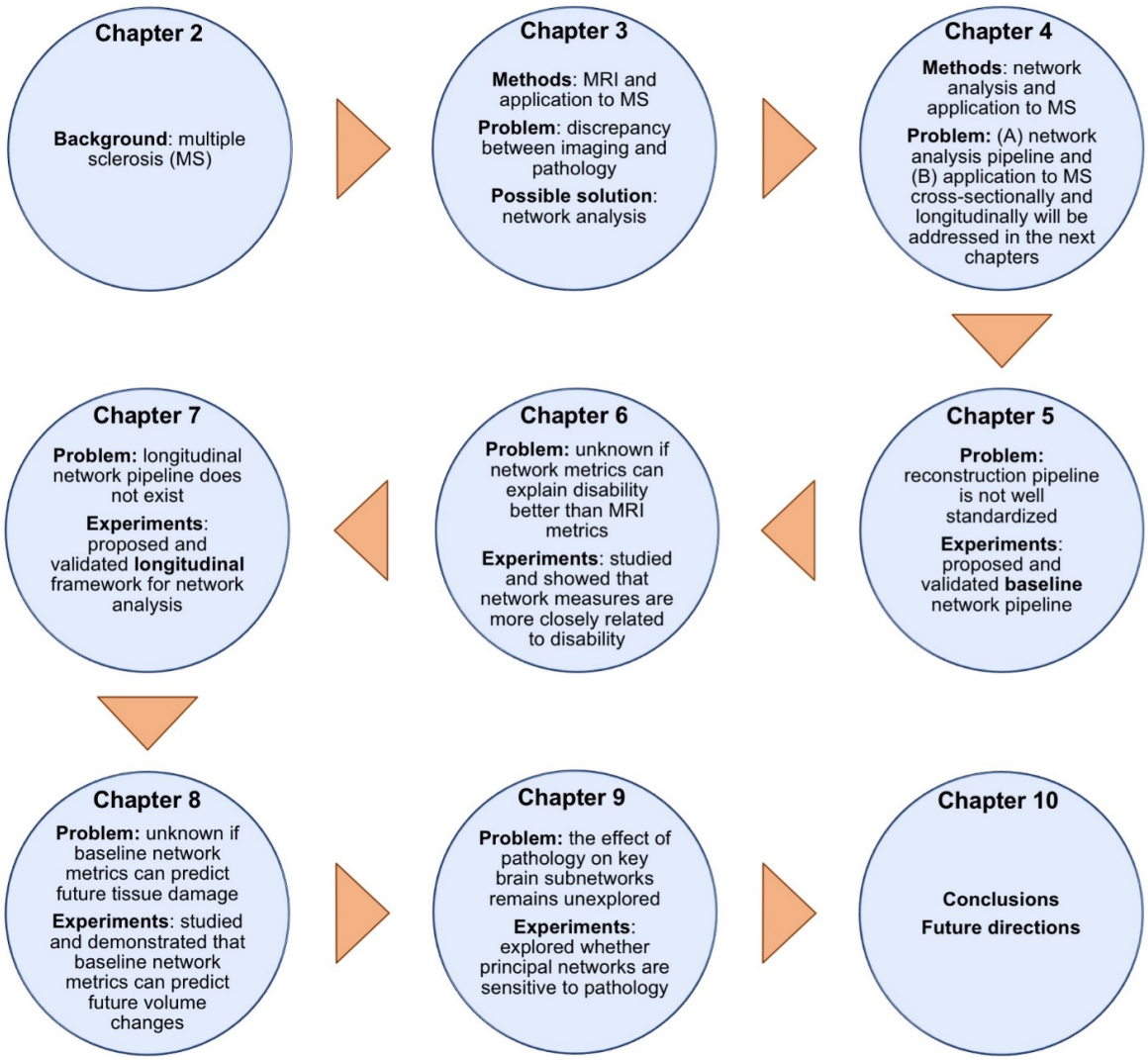

Chapter 2

2. Multiple Sclerosis

2.1. Multiple sclerosis overview

MS is a chronic demyelinating and neurodegenerative disease of the CNS and is the most common neurological cause of disability in young adults (Calabrese et al., 2015). It is estimated that approximately 2.3 million people have MS worldwide, while women are twice as likely to develop the disease (Thompson et al., 2018b). The cause of the disease is currently unknown, although it is suggested that multiple susceptibility genes and several environmental factors contribute to the disease manifestation (Thompson et al., 2018b; Reich et al., 2018). Pathological characterization of MS consists of inflammation, demyelination and axonal damage. Modern imaging techniques such as MRI have revolutionised our understating of brain phenotypic features *in vivo* and how pathology evolves over time. In this chapter, I provide a brief overview of MS, followed by **chapter 3** which will introduce MRI fundamentals and its usage in the context of MS. The final introductory chapter, **chapter 4,** will introduce network analysis and how its usage in MS has helped us gain further insights into pathological processes that relate to disability.

2.2. Multiple sclerosis subtypes

MS is categorized into four main subtypes per its clinical course **(Fig 2.1)**. Since 2013, clinically isolated syndrome (**CIS**) is considered as the first clinical representation of a disease that shows characteristics of inflammation and demyelination (loss of myelin) suggestive of MS, but still should fulfil the criteria of dissemination in time (for more details on diagnostic criteria see **chapter 3**). Relapsing-remitting MS **(RRMS)** is the most common form of MS, possibly around 85%. It is characterized by clearly defined attacks (relapses), followed by partial or complete recovery periods (remission). During remission, there is no obvious progression of the disease. Approximately 10% of the RRMS patients become secondary-progressive MS **(SPMS)** within a decade after the initial diagnosis and the conversion point is currently very poorly understood. After conversion, SPMS is characterized by a steadier progression of disability combined with an increase in neurodegeneration. Primary progressive MS **(PPMS)** is characterized by steadily worsening of neurologic function from onset, although the rate of progression changes over time. Approximately 10% of patients with MS are diagnosed with PPMS (Thompson et al., 2018a)

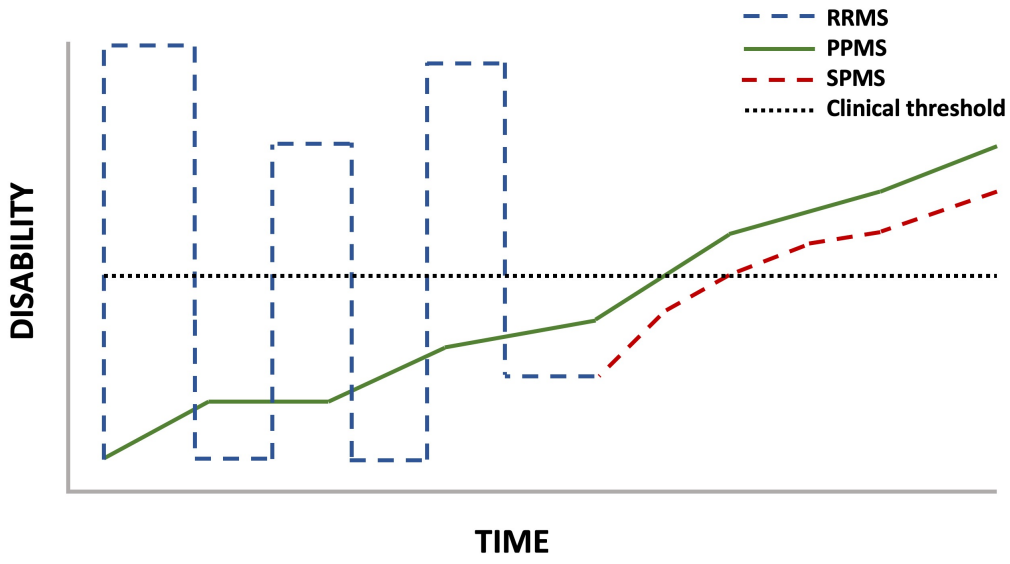

Figure 2.1 Progression of disability in multiple sclerosis over time

RRMS is marked by relapses (appearance of symptoms) and remission (recovery). Initially, disability remains relatively low and it accumulates over time. In **PPMS**, there is a steady increase of disability from disease onset without any relapses. In **SPMS**, the initial relapses disappear, and the physical disability accumulates rapidly. In this diagram **CIS** is not depicted. Relapse and remission are not in temporal scale.

2.3. Causes

The main factors currently thought to play causal roles in MS manifestation can be divided into the environmental and the genetic.

Environmental factors

Environmental risk factors such as vitamin D deficiency, which is related to reduced exposure to sunlight, diet, obesity in early life and cigarette smoking are known to play a part in MS development (Marrie, 2004). It is important to state that low vitamin D and cigarette smoking are the most critical known causes (Ramanujam et al., 2015; Ascherio et al., 2014) and although correction of vitamin D insufficiency could be important for disease prevention, there is no evidence of association between neonatal vitamin D levels and disease risk (Ueda et al., 2014). In addition, exposure to infectious agents in early adulthood might decrease the risk of developing autoimmune and allergic diseases (Bach, 2002) while specific infections in young adults such as the Epstein-Barr virus increase the risk of developing the disease (Levin et al., 2005).

Genetics

The fact that MS seems to occur within families provides evidence of the existence of genetic causative factors. For example, carriers of specific alleles within the human leucocyte antigen (HLA) region are three times more likely to develop MS than non-carriers. In addition, a genome-wide association study (GWAS) identified some non-HLA variants such as interleukin 2 receptor alpha (IL2RA) and interleukin 7 receptor alpha (IL7RA), that have some minor effects on disease development (for comprehensive review see Thompson et al. (2018b)). These results highlight the existence of the genetic component in MS and thus invite subsequent studies to

identify determinants of disease progression that could result in more personalized patient treatment.

2.4. From causes to pathology

Currently, there are two main hypotheses that relate to the root of the disease: the outside-in and inside-out models **(Fig. 2.2)**. The former takes the view that MS is an autoimmune disorder, during which the T-cells from the periphery cross the blood brain barrier and together with the B-cells destroy key components of the CNS such as myelin and axons (Lassmann et al., 2007). This, in turn, causes additional inflammatory reaction such as microglia activation and production of reactive species, resulting in demyelination and tissue damage (Haider et al., 2011). The outside-in model is challenged by the inside-out model, according to which the problem is initiated within the CNS in a manner similar to other neurodegenerative conditions. The idea is that primary degeneration, possibly involving the oligodendrocyte-myelin complex (Stys et al., 2012), releases antigenic components that in turn trigger the immune cascade (Trapp and Nave, 2008). Irrespective of the underlying sequence of events that lead to disease manifestation, it is becoming evident that during the progressive phases the intensity of the inflammatory response declines over time, while demyelination and neurodegeneration remains throughout the disease duration (Frischer et al., 2009).

The hallmarks of MS pathology are neuroaxonal loss, demyelination and astrocytic gliosis (Thompson et al., 2018b). Neuroaxonal loss (also known as neurodegeneration) is particularly relevant as it is strongly associated with permanent clinical disability. *In vivo*, the pathogenic events such as inflammation, demyelination, axonal loss and gliosis can be studied using both conventional and advanced imaging

techniques. For example, neurodegeneration is observed as reduced brain volume (or brain atrophy) by volumetric MRI (Thompson et al., 2018b). More detailed role of MRI in MS prognosis and diagnosis will be discussed in **chapter 3**.

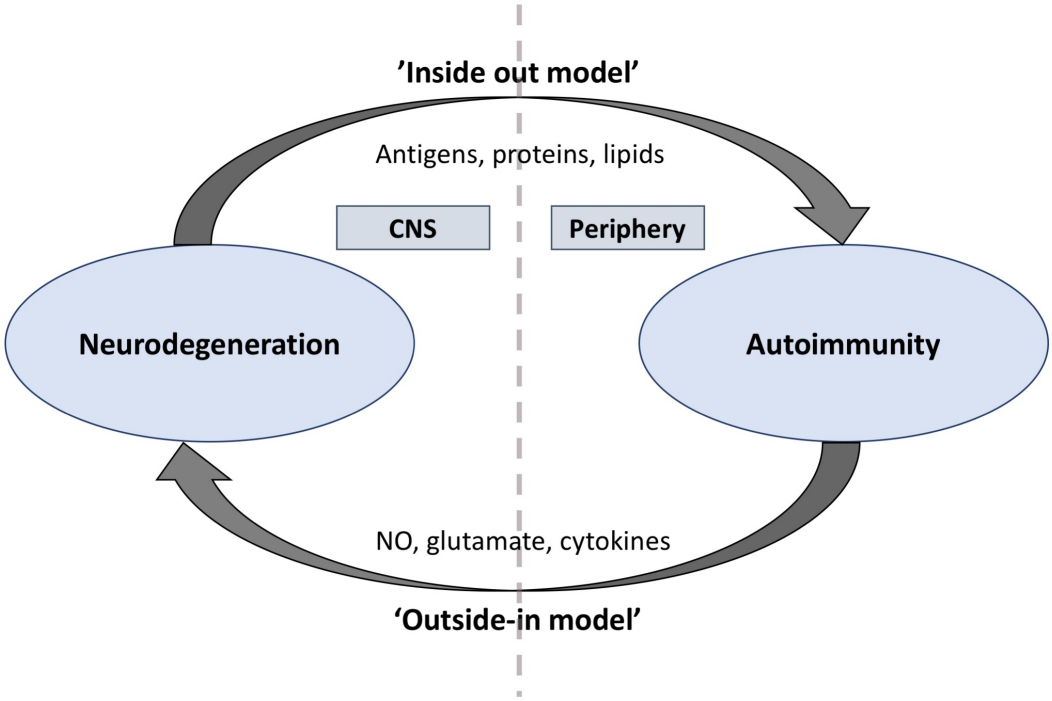

Figure 2.2. Schematic diagram depicting the two hypothetical models in multiple sclerosis

The "outside-in model" suggests that T-cells from the periphery cross the blood brain barrier and along with macrophages and B-cells, destroy components of the Central Nervous System (CNS) causing neurodegeneration. To the contrary, the "inside-out model" argues that cytodegeneration is the first event in MS similarly to other neurodegenerative diseases and the release of several antigenic components causes an inflammatory cascade which possibly causes further degeneration. NO: nitric oxide (Figure modified from Stys et al. (2012))

2.5. From pathology to clinical features

Physical symptoms may vary depending on the location of the lesion. For example, a common presentation of MS is optic neuritis, in which the affected individual experiences loss of vision. Other recognised symptoms in MS are sensory and/or motor disturbances (e.g. numbness, tingling, weakness in arm or leg), sphincter or brainstem dysfunction (Lublin et al., 2014). Physical disability also varies depending on the MS subtype. For example, symptoms tend to resolve after a relapse at earlier stages of the disease whereas accumulation of disability and exacerbation of symptoms is observed at later stages of the RRMS or in SPMS subtype (Lublin et al., 2014).

2.6. Treatment

Treatments are not curative but can modify the course of the disease. For example, immune response modulators such as interferon beta (Bertolotto and Gilli, 2008) or glatiramer acetate (Huntley, 2006) are moderately effective and slow the incidence of relapses by around 30% (Palace et al., 2015). Newer pharmacological agents such as natalizumab (Polman et al., 2006) and fingolimod (Sanford, 2014) aim to reduce inflammation completely either by preventing the entrance of immune cells into the brain or by blocking departure from the lymph nodes. Even though these treatments seem to reduce the relapses by approximately 70%, they can be associated with significant side effects (Huntley, 2006), highlighting the importance of close monitoring. Interestingly, while disease modifying treatments seem to be effective with respect to the inflammatory component of the disease, it is not yet clear what the effects are, if any, on the neurodegenerative aspect of the disease. Recently, a phase III clinical trial reported that Ocrelizumab was associated with lower rates of clinical

progression in patients with PPMS (Montalban et al., 2017) and although the reasons that Ocrelizumab slows down disease activity remains uncertain it still signifies a positive step towards treatment for the progressive phases.

2.7. Strategies to study multiple sclerosis *in vivo*

The non-invasive study of the brain has given new insights into brain structure and function how these are affected in disease conditions. Given the critical importance of MRI in monitoring the disease course and in evaluating treatment effects *in vivo*, **chapter 3** will introduce MRI and discuss how its application has advanced our understanding of MS pathology.

Bibliography

Ascherio A, Munger KL, White R, et al. (2014) Vitamin D as an early predictor of multiple sclerosis activity and progression. *JAMA Neurol* 71: 306-314.

Bach JF. (2002) The effect of infections on susceptibility to autoimmune and allergic diseases. *N Engl J Med* 347: 911-920.

Bertolotto A and Gilli F. (2008) Interferon-beta responders and non-responders. A biological approach. *Neurol Sci* 29 Suppl 2: S216-217.

Calabrese M, Magliozzi R, Ciccarelli O, et al. (2015) Exploring the origins of grey matter damage in multiple sclerosis. *Nat Rev Neurosci* 16: 147-158.

Frischer JM, Bramow S, Dal-Bianco A, et al. (2009) The relation between inflammation and neurodegeneration in multiple sclerosis brains. *Brain* 132: 1175-1189.

Haider L, Fischer MT, Frischer JM, et al. (2011) Oxidative damage in multiple sclerosis lesions. *Brain* 134: 1914-1924.

Huntley A. (2006) A review of the evidence for efficacy of complementary and alternative medicines in MS. *Int MS J* 13: 5-12, 14.

Lassmann H, Bruck W and Lucchinetti CF. (2007) The immunopathology of multiple sclerosis: an overview. *Brain Pathol* 17: 210-218.

Levin IL, Murger LK, Rubertone MV, et al. (2005) Temporal Relationship Between Elevation of Epstein-Barr Virus Antibody Titers
and Initial Onset of Neurological Symptoms in Multiple Sclerosis. *JAMA Neurol* 293.

Lublin FD, Reingold SC, Cohen JA, et al. (2014) Defining the clinical course of multiple sclerosis: the 2013 revisions. *Neurology* 83: 278-286.

Marrie RA. (2004) Environmental risk factors in multiple sclerosis aetiology. *Lancet Neurol* 3: 709-718.

Montalban X, Hauser SL, Kappos L, et al. (2017) Ocrelizumab versus Placebo in Primary Progressive Multiple Sclerosis. *N Engl J Med* 376: 209-220.

Palace J, Duddy M, Bregenzer T, et al. (2015) Effectiveness and cost-effectiveness of interferon beta and glatiramer acetate in the UK Multiple Sclerosis Risk Sharing Scheme at 6 years: a clinical cohort study with natural history comparator. *Lancet Neurol* 14: 497-505.

Polman CH, O'Connor PW, Havrdova E, et al. (2006) A randomized, placebo-controlled trial of natalizumab for relapsing multiple sclerosis. *N Engl J Med* 354: 899-910.

Ramanujam R, Hedstrom AK, Manouchehrinia A, et al. (2015) Effect of Smoking Cessation on Multiple Sclerosis Prognosis. *JAMA Neurol* 72: 1117-1123.

Reich DS, Lucchinetti CF and Calabresi PA. (2018) Multiple Sclerosis. *N Engl J Med* 378: 169-180.

Sanford M. (2014) Fingolimod: a review of its use in relapsing-remitting multiple sclerosis. *Drugs* 74: 1411-1433.

Stys K, Zamponi G, Minnen J, et al. (2012) Will the real multiple sclerosis please stand up? *NATURE REVIEWS | NEUROSCIENCE*.

Thompson AJ, Banwell BL, Barkhof F, et al. (2018a) Diagnosis of multiple sclerosis: 2017 revisions of the McDonald criteria. *The Lancet Neurology* 17: 162-173.

Thompson AJ, Baranzini SE, Geurts J, et al. (2018b) Multiple sclerosis. *The Lancet*.

Trapp BD and Nave KA. (2008) Multiple sclerosis: an immune or neurodegenerative disorder? *Annu Rev Neurosci* 31: 247-269.

Ueda P, Rafatnia F, Baarnhielm M, et al. (2014) Neonatal vitamin D status and risk of multiple sclerosis. *Ann Neurol* 76: 338-346.

Chapter 3

3. Magnetic resonance imaging and application to multiple sclerosis

3.1. Magnetic resonance imaging overview

The development of biomarkers for MS has been limited by the slow rate of disease progression and the heterogeneous pathological mechanisms (Reich et al., 2018). The most important diagnostic and prognostic tool for assessing MS *in vivo* is MRI. Since MRI's invention, several MRI acquisition methods have been developed aiming to improve the quality of the acquired images and therefore provide further insights into the pathological processes. For instance, in MS, T1-weighted imaging (Eshaghi et al., 2018), fluid attenuated inversion recovery (FLAIR) (Ge, 2006), phase sensitive inversion recovery (PSIR) (Sethi et al., 2012), magnetization transfer ratio (MTR) (Bodini et al., 2016), diffusion-weighted imaging (DWI) (Bodini et al., 2009) and functional MRI (fMRI) (Rocca et al., 2005) are advanced MRI techniques that are commonly used either as diagnostic or research tools. This section will provide a very brief overview of the basis of MR technology. Since this thesis focuses on diffusion-based connectivity, a brief introduction of DWI will be given and some common biases in MRI processing will be introduced. The final section will discuss how MRI has helped advance our understanding in MS pathology.

3.2. Electromagnetic basis of magnetic resonance technology

MRI takes advantage of protons that are highly abundant in the neural tissue. All protons possess a 'spin', which generates a local magnetic field. In general, the proton spins in a tissue orient in random directions. However, when the tissue is placed in an external magnetic field, the protons align along the axis of the main magnetic field, B_0. Even though, it is likely that some protons will align "antiparallel" to B_0, it is energetically favourable to orient parallel to B_0 so there is a net magnetic field vector, M_0, in the parallel direction. Additionally, protons in a magnetic field do not stay stationary but they precess around their axis at an angular frequency, ω_0, that is proportional to the gyromagnetic ratio, γ, of the nuclei and the external magnetic field, B_0 (given in Tesla) and is referred to as the Larmor frequency (**Fig. 3.1)**:

$$\omega_0 = \gamma B_0$$

Eq. 3.1

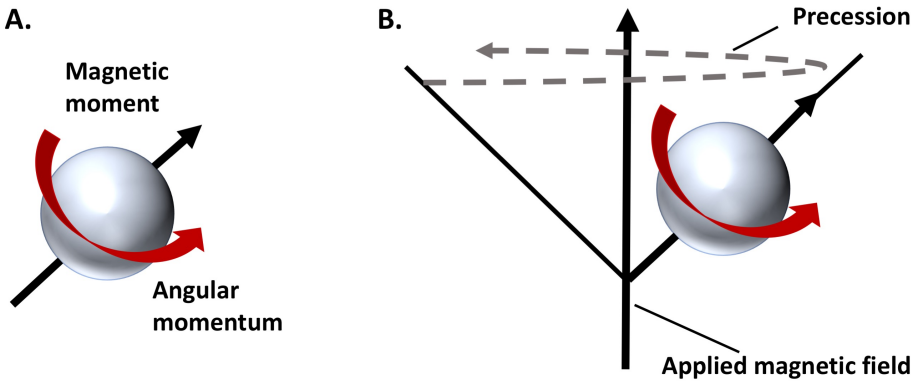

Figure 3.1. Magnetic properties of the hydrogen atom.

(A) Protons have an angular momentum ("spin") that generates a local magnetic field. **(B)** The spinning proton precesses around the externally applied magnetic field at a very well-defined frequency, the Larmor frequency.

To obtain the MR signal for which the images are reconstructed, M_0 must be disturbed from its equilibrium state and this is achieved by exposing the tissue to radiofrequency (RF) pulses, B_1. If the RF pulses are oscillating at the Larmor frequency and are applied in a direction orthogonal to B_0, then there are two main outcomes: a) decrease in the net magnetization, $M_{//} < M_0$, as protons will absorb energy from the RF and reorient themselves precessing around the direction of B_1 and b) the generation of a new magnetic field vector, $M_{\perp}$, in the transverse plane of the main magnetic field. Switching off the RF allows the protons to relax and go back to equilibrium, thus the net magnetic field, $M_{//}$, to reach again its maximum value, M_0, and the transverse magnetization, $M_{\perp}$, to decrease to zero (**Fig. 3.2**). The time needed for protons to realign to the longitudinal direction is measured by T1 while the time constant governing the transverse relaxation decay is referred to as T2.

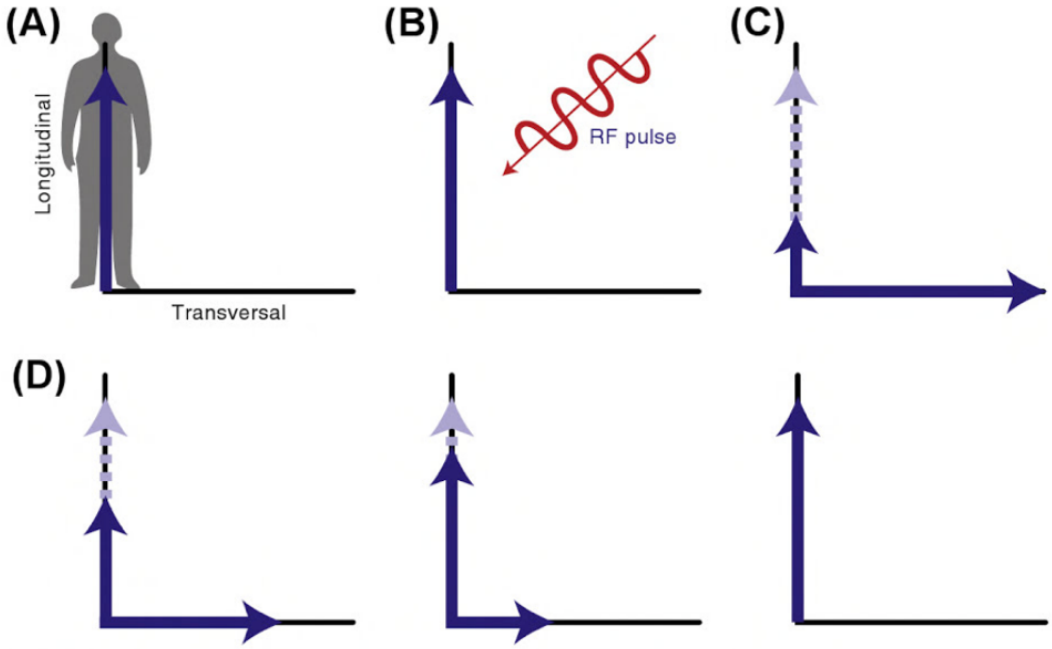

Figure 3.2. Radiofrequency pulses and net magnetic field

(A) A net magnetization, M_0, is present along the longitudinal axis. Application of radiofrequency (RF) pulse **(B)** causes a decrease in the net longitudinal magnetization $M_{//}$, **(C)**. Also, a new net magnetization, $M_{\perp}$, is generated along the transverse axis **(C)**. **(D)** Switching off the RF pulse causes increase of the net magnetization, $M_{//}$, along the longitudinal axis and decrease in the transverse component, $M_{\perp}$, until the net magnetic field returns to the original state, M_0. (Figure adopted from Carter and Shieh (2009))

The MR image contrast can be manipulated using “sequences”, i.e. the programme that controls the scanner, including for example when to start and stop the RF pulses. The two most important parameters are the repetition time (TR) and echo time (TE). The TR is the time between consecutive slice excitation due to RF pulses or excitation of the same slice due to refocusing RF pulses. Refocusing RF pulses are needed to refocus the spins so that sufficient signal is generated to produce an image (see next paragraph). On the other hand, TE is the time between the excitation RF pulse and the measured signal (that is called the “echo”).

In image reconstruction, the classification of each voxel (3-dimensional pixel) depends on both the signal intensity and its position within the brain. For instance, in a T1-weighted image, cerebrospinal fluid (CSF), WM and grey matter (GM) have the lowest, the highest and the intermediate signal intensity respectively due to their difference in fat and water composition. For instance, fat has a shorter T1 relaxation time than water, which means that fat will recover its longitudinal magnetization. After the second RF pulse is given at 90^{o}, fat would have fully recovered in the longitudinal plane while water would have not. The higher the transverse magnetization the more signal is received (in this case in WM due to the high composition to myelin) (Larvie and Fischl, 2016). These differences in signal intensity can be exploited by several post-processing algorithms to delineate the various tissue types. Once delineated, the volumes of these tissues can be estimated, which allows to assess tissue loss in MS pathology for example (Eshaghi et al., 2014).

3.3. Diffusion-weighted imaging

DWI provides image contrast based on the diffusion of water molecules in the brain. At the microscopic level, water molecules are in constant motion due to their thermal energy, a phenomenon called Brownian motion (Huisman, 2003). In unconstrained medium, such as in CSF, water molecules are free to diffuse in any possible direction (isotropic diffusion) whereas in the presence of barriers such as neural tracts, the diffusion is hindered and the water molecules are more likely to diffuse in the direction parallel to the barriers (**Fig. 3.3.**) (Huisman, 2010; Clayden, 2013).

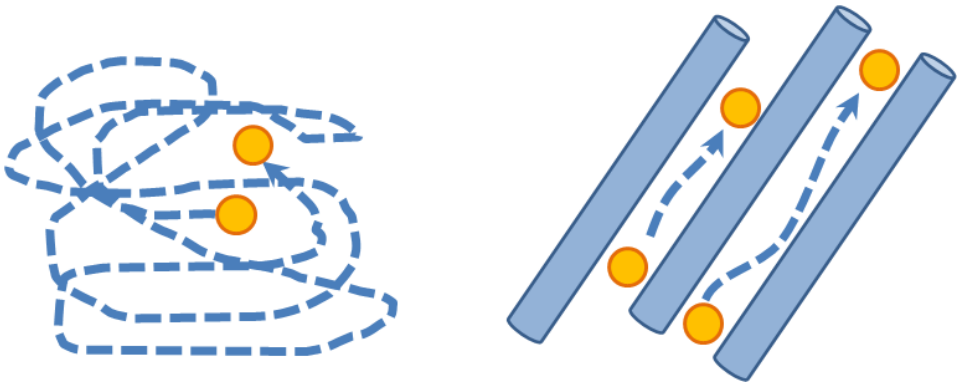

Figure 3.3. Diffusion of water molecules.

Schematic diagram showing the diffusion of water molecule in a free environment **(left)** and in a restricted environment **(right)**. Water molecules are depicted as orange dots. (Figure adapted from García-Martí et al. (2013))

From MR perspective, diffusion-weighed sequences are developed that are sensitive to this motion **(Fig 3.4.)**. This is achieved with the application of strong magnetic field gradients (variation of the magnetic field with respect to one direction). In DWI, equal gradients are applied on either side of a 180º RF in a sequence often called Stejskal-Tanner (Stejskal and Tanner, 1965). This is a spin echo type sequence that is used to refocus the spin magnetisation by a pulse of resonant electromagnetic radiation. These gradient pulses are designed to cancel each other's effect out if the spins do not move. Diffusing spins though move into different positions between the first and second diffusion gradient falling out of phase and eventually losing signal (signal attenuation). The position change happens along different directions, depending on the microstructure. The amount of signal attenuation depends on the amplitude and direction of the applied diffusion gradients. Diffusion gradients can be applied along any combination of the main Cartesian axis of the scanner, i.e. X, Y, Z axes, and combined to produce a single diffusion-weighted image (Alexander et al., 2011).

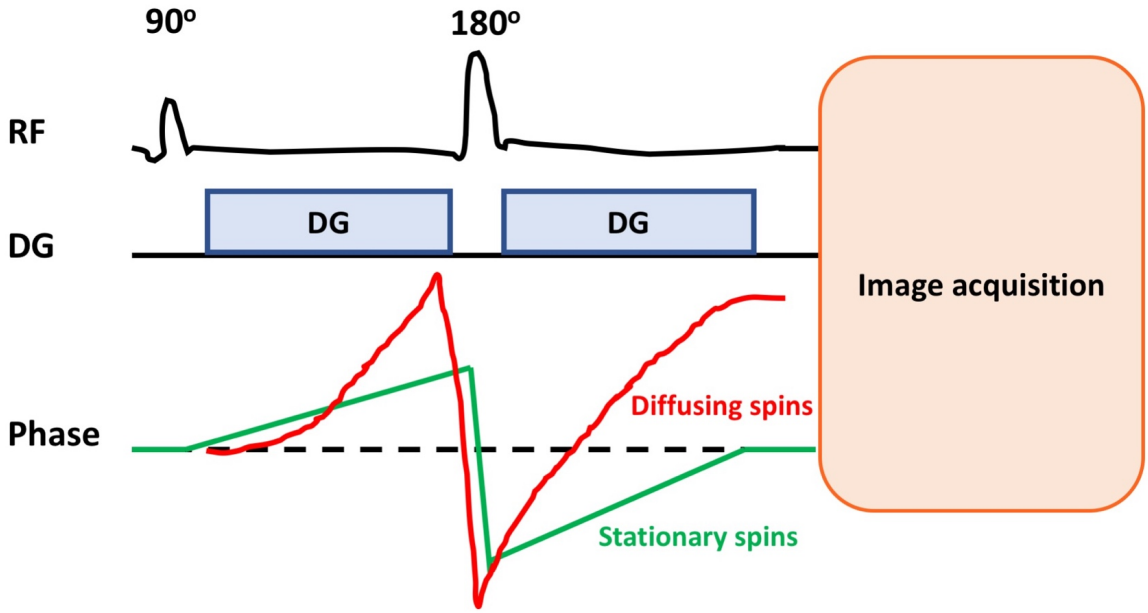

Figure 3.4. Gradient spin echo technique.

Stationary spins are not affected by the gradients applied on either side of the 180º RF while diffusing spins are dephased. Diffusion gradients are applied along the X, Y, Z axes, or any of their combinations, so that the signal can reflect the structure presented in each voxel. RF = radiofrequency; DG = diffusion gradients;

The signal loss from the net movement of particles is given by the Stejskal-Tanner equation

$$S = S_0 e^{-bD}$$

Eq. 2.2

where *S* is the signal received at any particular gradient value (b value) and S_0 is the signal without any diffusion-weighting gradients (b0 s/mm^2) and D is the apparent diffusion coefficient (ADC) (Le Bihan et al., 1991; Stejskal and Tanner, 1965). The b-value or 'b' is given by the equation below:

$$b = (\gamma G \delta)^2 (\Delta - \frac{\delta}{3})$$

Eq. 2.3

where γ is the gyromagnetic ratio (MHz/T), G is the amplitude of the diffusion gradients (mT/m), δ is the width of the diffusion gradient pulses (ms) and Δ is the time between two diffusion gradients (ms). From the **Eq. 2.2** and **2.3** we can see that the signal loss depends on the time between the pulses, strength and duration of gradients applied. Exploiting thus the signal dependency on particle motion we are able to generate image contrast based on the water molecules diffusion properties in tissues (Chilla et al., 2015).

Clinically, several DW images can be obtained by altering the strength and magnitude of the applied gradient (b-value). DWI has been particularly useful in cases in which conventional MR technique does not show significant changes in images due pathological effects. For example, in stroke followed ischaemia (inadequate blood supply) DWI changes are detected as early as 30 mins followed the event compared to T2-weighted imaging (classically considered as conventional imaging) which changes 8 hours after stroke onset (Srinivasan et al., 2006). Further DWI development led to the diffusion tensor model (the simplest model that assumes that diffusion follows a Gaussian (normal) distribution), allowing quantification of water diffusion in each voxel. The most used metric is fractional anisotropy (FA), which quantifies the fraction of the diffusion that is anisotropic and takes values between 0 and 1. If, for instance, FA close to 1 means that water molecules are mainly diffusing in a single direction which is suggestive of underlying structures where no crossing fibres are present. Diffusion tensor is rotationally invariant meaning that it defines three orthogonal axis and their diffusivities reflecting the underlying tissue independently of

the position of the subject in the scanner (Alexander et al., 2011). Additionally, diffusion MRI can be used to reconstruct the putative trajectories of the neural tracts using various tractography algorithms and this constitutes the basis of structural connectivity, which will be discussed in **chapter 4** of this thesis.

3.4. Common MRI acquisition-related artifacts

MRI artifacts are features that present in the image that are not present in the original object. During image acquisition many artifacts can occur which need to be corrected so they do not affect diagnostic and research quality. Some of the common artifacts that we corrected in this thesis are introduced below.

Bias field

Bias field is also known as intensity inhomogeneity occurring within tissue of the same physical properties mainly due to sensitivity of the receiver coil (Despotovic et al., 2015). Mapping out and removing intensity variation is most commonly performed in structural scans as subsequent algorithms to delineate various tissue types rely on intensity homogeneity within tissue of the same properties.

Motion artefact

Motion artefacts are caused by voluntary or involuntary subject movements e.g. from physiological sources like respiration, cardiac motion and blood flow, as well as from macroscopic motion such as swallowing or change in position of the head that can happen despite stabilisation in the coil with padding. These result in image blurring or shading. Techniques such as cardiac gating aim to synchronise the involuntary movements with image acquisition minimising thus motion artefacts (Barrett and Keat, 2004).

Eddy currents

For diffusion weighting, additional strong magnetic field gradients are added, and acquisition is very fast (usually the entire image for a certain slice is acquired in a single shot using echo planar imaging (EPI). This means that rapidly changing magnetic field gradients are applied during the acquisition. These gradients are inducing additional currents that are known as eddy currents. Eddy currents cause unwanted time-varying gradients and shifts in the main magnetic field which ultimately cause image shearing, shading and blurring (Spees et al., 2011). Image post-processing techniques have been developed that aim to minimise the effects of the eddy currents (Andersson and Sotiropoulos, 2015).

Echo planar imaging distortions

As mentioned above, EPI is an MR acquisition method that allows fast image acquisition that significantly shortens MR imaging times and can thus reduce motion artefacts. However, EPI is sensitive to magnetic field inhomogeneities and in particular in anatomic structures at the interface between air, tissue and fluid due to the differences in their magnetic susceptibility (the extent to which a substance become magnetised when placed in an external magnetic field) (Poustchi-Amin et al., 2001). This can cause image geometric distortion at areas between CSF, brain tissue and skull.

3.5. Image registration

One particular concept in image analysis is image registration. It is defined as the process of overlaying (spatially aligning) two or more images that are taken at different time points or using different modalities (pulse sequences). Briefly, image registration

relies on the finding of common image features so that corresponding images can be spatially aligned. There are two types of spatial alignment:

Rigid transformation

It is considered a 6-parameter transformation because it includes translation along the X, Y, Z dimensions and rotation along the X, Y, Z axis. These preserve the shape of the object but they move it around in space. In neuroimaging, rigid body transformations are typically used to align scans belonging to the same person but acquired at different times or using different pulse sequences.

Affine transformation

It is considered a 12-parameter transformation as it includes 6 more parameters i.e. stretching along the X, Y, Z axes and shearing or skewing along the XY, YZ, XZ, planes. It is most commonly used for inter-subject registration (different subjects) or the same subjects but for different stages of their development (Despotovic et al., 2015).

Specific to MS inter-subject registration problems are due to brain lesions that make it difficult to match the same structures between healthy and diseased brains in a common coordinate space (Chard et al., 2010). Therefore, some techniques have been proposed to overcome this issue by filling WM lesions with intensities similar to those of WM before any post-processing steps (Magon et al., 2014; Valverde et al., 2015). Such approach is most commonly applied in T1-weighted scans but not for DWI scans as changing the intensity in DWI data will significantly alter the underlying derived diffusivity impacting subsequent analysis.

3.6. Application of magnetic resonance imaging in multiple sclerosis

MRI is now firmly established as a key tool in the diagnosis of MS due to its ability to identify mainly WM lesion distribution. According to the 2017 revised McDonald's criteria: dissemination in space requires the presence of two or more lesions in specific locations: periventricular, juxta-cortical, infra-tentorial and spinal cord. Dissemination in time can be established by the a) presence of a lesion when compared with a previous scan and b) simultaneous presence of gadolinium (pharmacological agent used in MRI to improve image contrast) enhancing and non-enhancing lesion (Thompson et al., 2018a).

MRI is also an important research tool to assess further mechanisms of MS as well as prediction of disease progression. This is particularly important because the number and volume of WM lesions alone can only explain a fraction of the diverse clinical outcomes. This mismatch has been termed as **clinico-radiological paradox** (Barkhof, 2002). This led to the usage of more advanced techniques including diffusion-weighted methods to investigate normal appearing brain tissue. These techniques have been successful in detecting changes outside visible WM pathology such as reduced tissue integrity, suggesting **disconnection** as a potential mechanism of cognitive dysfunction (Dineen et al., 2009). In addition to WM pathology, studies have also investigated grey matter (GM) revealing a relationship between GM atrophy and cognitive deficits (Fisniku et al., 2008b; Fisher et al., 2008; Steenwijk et al., 2016) in an attempt to study disease mechanisms. In addition, in a large multicentre study Eshaghi et al. (2018) demonstrated that deep grey matter (DGM) volume loss drives disability accumulation in MS highlighting the importance of quantitative MRI measures for disease progression, too.

3.7. Motivation for the methods used in this thesis

The interplay between inflammation, demyelination and neurodegeneration throughout the brain, and even more generally in the CNS, points towards the necessity of more advanced techniques that would be able to integrate across space pathological features, forecast the disease course and monitor treatment effects. One possible way is the use of network analysis which can incorporate data from the interconnecting regions beyond focal pathology aiming to provide a more holistic characterization between localised damage and diffused pathology. **Chapter 4** will introduce network analysis and discuss current application to MS.

Bibliography

Alexander AL, Hurley SA, Samsonov AA, et al. (2011) Characterization of cerebral white matter properties using quantitative magnetic resonance imaging stains. *Brain Connect* 1: 423-446.

Andersson JL and Sotiropoulos SN. (2015) Non-parametric representation and prediction of single- and multi-shell diffusion-weighted MRI data using Gaussian processes. *Neuroimage* 122: 166-176.

Barkhof F. (2002) The clinico-radiological paradox in multiple sclerosis revisited. *Curr Opin Neurol* 15: 239-245.

Barrett JF and Keat N. (2004) Artifacts in CT: recognition and avoidance. *Radiographics* 24: 1679-1691.

Bodini B, Chard D, Altmann DR, et al. (2016) White and gray matter damage in primary progressive MS: The chicken or the egg? *Neurology* 86: 170-176.

Bodini B, Khaleeli Z, Cercignani M, et al. (2009) Exploring the relationship between white matter and gray matter damage in early primary progressive multiple sclerosis: an in vivo study with TBSS and VBM. *Hum Brain Mapp* 30: 2852-2861.

Carter M and Shieh J. (2009) *Guide to Research Techniques in Neuroscience* Eslevier.

Chard DT, Jackson JS, Miller DH, et al. (2010) Reducing the impact of white matter lesions on automated measures of brain gray and white matter volumes. *J Magn Reson Imaging* 32: 223-228.

Chilla GS, Tan CH, Xu C, et al. (2015) Diffusion weighted magnetic resonance imaging and its recent trend-a survey. *Quant Imaging Med Surg* 5: 407-422.

Clayden JD. (2013) Imaging connectivity: MRI and the structural networks of the brain. *Funct Neurol* 28: 197-203.

Despotovic I, Goossens B and Philips W. (2015) MRI segmentation of the human brain: challenges, methods, and applications. *Comput Math Methods Med* 2015: 450341.

Dineen RA, Vilisaar J, Hlinka J, et al. (2009) Disconnection as a mechanism for cognitive dysfunction in multiple sclerosis. *Brain* 132: 239-249.

Eshaghi A, Bodini B, Ridgway GR, et al. (2014) Temporal and spatial evolution of grey matter atrophy in primary progressive multiple sclerosis. *Neuroimage* 86: 257-264.

Eshaghi A, Prados F, Brownlee W, et al. (2018) Deep grey matter volume loss drives disability worsening in multiple sclerosis. *Ann Neurol*.

Fisher E, Lee JC, Nakamura K, et al. (2008) Gray matter atrophy in multiple sclerosis: a longitudinal study. *Ann Neurol* 64: 255-265.

Fisniku LK, Chard DT, Jackson JS, et al. (2008b) Gray matter atrophy is related to long-term disability in multiple sclerosis. *Ann Neurol* 64: 247-254.

García-Martí G, Alberich-Bayarri A and Martí-Bonmati L. (2013) *Brain Structure MR Imaging Methods: Morphometry and Tractography*.

Ge Y. (2006) Multiple sclerosis: the role of MR imaging. *AJNR Am J Neuroradiol* 27: 1165-1176.

Huisman TA. (2003) Diffusion-weighted imaging: basic concepts and application in cerebral stroke and head trauma. *Eur Radiol* 13: 2283-2297.

Huisman TA. (2010) Diffusion-weighted and diffusion tensor imaging of the brain, made easy. *Cancer Imaging* 10 Spec no A: S163-171.

Larvie M and Fischl B. (2016) Volumetric and fiber-tracing MRI methods for gray and white matter. *Handb Clin Neurol* 135: 39-60.
Le Bihan D, Turner R, Moonen CT, et al. (1991) Imaging of diffusion and microcirculation with gradient sensitization: design, strategy, and significance. *J Magn Reson Imaging* 1: 7-28.
Magon S, Gaetano L, Chakravarty MM, et al. (2014) White matter lesion filling improves the accuracy of cortical thickness measurements in multiple sclerosis patients: a longitudinal study. *BMC Neurosci* 15: 106.
Poustchi-Amin M, Mirowitz SA, Brown JJ, et al. (2001) Principles and applications of echo-planar imaging: a review for the general radiologist. *Radiographics* 21: 767-779.
Reich DS, Lucchinetti CF and Calabresi PA. (2018) Multiple Sclerosis. *N Engl J Med* 378: 169-180.
Rocca MA, Colombo B, Falini A, et al. (2005) Cortical adaptation in patients with MS: a cross-sectional functional MRI study of disease phenotypes. *Lancet Neurol* 4: 618-626.
Sethi V, Yousry TA, Muhlert N, et al. (2012) Improved detection of cortical MS lesions with phase-sensitive inversion recovery MRI. *J Neurol Neurosurg Psychiatry* 83: 877-882.
Spees WM, Buhl N, Sun P, et al. (2011) Quantification and compensation of eddy-current-induced magnetic-field gradients. *J Magn Reson* 212: 116-123.
Srinivasan A, Goyal M, Al Azri F, et al. (2006) State-of-the-art imaging of acute stroke. *Radiographics* 26 Suppl 1: S75-95.
Steenwijk MD, Geurts JJ, Daams M, et al. (2016) Cortical atrophy patterns in multiple sclerosis are non-random and clinically relevant. *Brain* 139: 115-126.
Stejskal EO and Tanner JE. (1965) Spin Diffusion Measurements: Spin Echoes in the Presence of a Time-Dependent Field Gradient. *The Journal of Chemical Physics* 42: 288-292.
Thompson AJ, Banwell BL, Barkhof F, et al. (2018a) Diagnosis of multiple sclerosis: 2017 revisions of the McDonald criteria. *The Lancet Neurology* 17: 162-173.
Valverde S, Oliver A, Roura E, et al. (2015) Quantifying brain tissue volume in multiple sclerosis with automated lesion segmentation and filling. *Neuroimage Clin* 9: 640-647.

"In biology, if seeking to understand function, it is usually a good idea to study structure" (Crick and Koch).

Chapter 4

4. Brain network analysis and application to multiple sclerosis

4.1. Brain network overview

As discussed in **chapter 3**, the sensitivity of MRI to acute and chronic WM lesions has made this tool essential for diagnosis (Thompson et al., 2018b). However, conventional MRI techniques do not necessarily represent processes of brain reorganisation in pathology and poorly reflect the long-term course of the disease (Filippi and Agosta, 2010; Fisniku et al., 2008a). Besides, current techniques that follow anatomical region-of-interest approaches (Bodini et al., 2009) can capture localized pathological mechanisms but not widespread pathology, thus it is quite difficult to predict the effect of localized damage to the broader functional domain (Barkhof, 2002).

Network analysis offers an alternative approach to study the brain. The human brain is essentially a network of neurons or brain regions and knowledge about their interconnections is limited. The interest in human brain mapping goes back to Santiago Ramón y Cajal, over a century ago (Ramón y Cajal, 1892), who for many is considered the father of modern neuroscience, and whose drawings of the neuronal cells shed light on the fundamental components of the CNS. Subsequent research focused on studying the neurons as a system to understand higher order functions

(Hebb, 1949). Disruption of the system gave rise to the “disconnection syndrome” concept (Catani and Mesulam, 2008). For example, a lesion in the corpus callosum, the brain region which connects the left and right hemispheres, could interrupt inter-hemispheric connections, i.e. disconnect the two hemispheres; an anomaly that at the beginning of the century would have been found surgically (i.e. craniotomy) (Geschwind and Kaplan, 1962). In the late 1970s, the first human being was MRI examined signifying a new era in diagnostic medicine. With the use of MRI and its specialised methods i.e. tractography, to visualise the connection pathways (Jones, 2008) in combination with fMRI (Rocca et al., 2005) we could non-surgically identify function-specific pathways providing practical evidence of the disconnection syndrome. Using MRI as a tool, Sporns proposed a conceptual framework where the entire brain connectivity was modelled as a network, also known as a connectome (Sporns et al., 2005). This integrative approach aims to provide a map of the brain connections so that we can better appreciate how these are affected in pathology.

Brain connectivity can be sub-divided into three scales and in three modes. The scales include microscale connectivity, looking at the synaptic connections of individual neurons (Lichtman et al., 2014), mesoscale connectivity, studying the connectivity between neuronal populations or cellular assemblies (Oh et al., 2014), and macroscale connectivity, where large populations of neurons forming distinct brain regions are studied (Hagmann et al., 2008). The modes or patterns of connectivity refer to several interrelated facets of brain organization. For example, structural connectivity refers to the physical links between brain regions, functional connectivity studies the statistical dependencies between the activity of different brain regions whereas effective connectivity investigates the causal interactions between distinct units in the CNS (Park and Friston, 2013). The main method used in this thesis from

an analysis perspective is macroscale structural connectivity and hence this chapter will focus on this type of connectivity, which will also be referred to as a structural brain network.

4.2. Structural network reconstruction

The brain network comprises nodes (brain regions) connected by edges and it can be represented as a matrix known as a connectivity matrix. Nodes, edges and the connectivity matrix are the main topics discussed in this section.

Network nodes

For a brain network, nodes are the different brain regions. Typically, a high resolution (1x1x1 mm^3) structural T1-weighed scan is used to parcellate the brain into anatomically distinct subregions (parcellations). There are many ways that such parcellation can be performed and there is no consensus as to what the criteria should be when parcellating the brain (**Fig. 4.1**) (Arslan et al., 2018). Ideally, both brain structure-function information should be taken into account (Craddock et al., 2013). Some of the popular atlases (reference image with a prior defined anatomical information (Evans et al., 2012)) are Automated Anatomical Labelling (AAL) and Harvard-Oxford which are based on anatomical landmarks, while Talairarch is based on cytoarchitecture as derived from post-mortem studies (Sotiropoulos and Zalesky, 2017). The subsequent connectome is built through two approaches a) tractography-based connectivity or b) cortical thickness-based correlation. Tractography is a method that allows us to reconstruct the neural pathways (see nodes subsection below). Cortical thickness correlation networks are based on the assumption that

connected brain areas share similar characteristics: neuronal and synaptic density, myelination and architecture (He et al., 2007).

Geodesic Information Flows (GIF) software was recently developed for brain segmentation and parcellation. According to Cardoso et al. (2015), GIF calculates the voxel probabilities of GM, WM and CSF using an atlas propagation and label fusion strategy and showed statistically improved segmentation of the different tissue types when compared to other techniques (Cardoso et al., 2015). The parcellation was in accordance to the Desikan-Killiany-Tourville atlas protocol that it the largest manually labelled human brain images based on anatomical characteristics (http://neuromorphometrics.org:8080/seg/) (Klein and Tourville, 2012). In this thesis, GIF was used to define the network nodes **(chapter 5).**

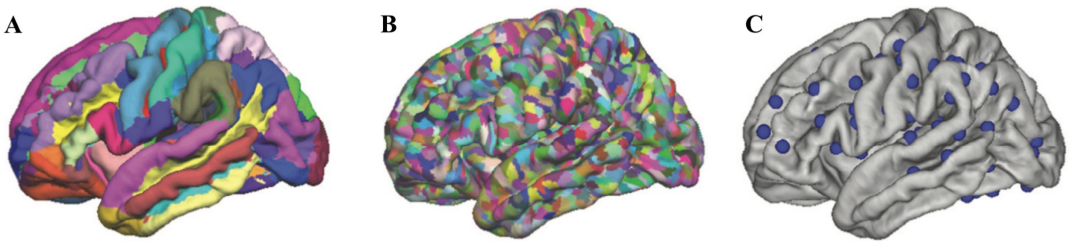

Figure 4.1. Examples of brain parcellations

Basic brain parcellation strategies include **(A)** prior anatomical templates **(B)** random division **(C)** functionally defined regions of interest (Figure adopted from Filippi et al. (2013)).

Network edges

Comparable to nodes, there are alternative ways to define the network edges. If the method that is chosen to build the network is cortical thickness connectivity, then edges represent the correlation coefficient between each pair of nodes. On the other hand, if the tractography-based connectivity was chosen from diffusion-weighted imaging, then tractography algorithm is performed which estimates the WM trajectories *in vivo* (Kaiser, 2011).

As discussed in **chapter 3**, DWI is capable of characterising tissue microstructure *in vivo*. This is achieved by acquiring several images to measure the magnitude of water diffusion in different directions oriented around the sphere. The magnitude and direction of water diffusion within each voxel is inferred through the measured signal. For example, diffusion tensor imaging (DTI) measurements acquired along the different directions are fitted to the three-dimensional ellipsoid represented mathematically by 3x3 matrix, known as a tensor. Then the diffusion in this tensor can be fully characterised by three orthogonal eigenvalues that represent the magnitude of diffusion along the longest, middle and shortest axes of the ellipsoid and the eigenvectors that represent the orientation of these axes (Alexander et al., 2011) (**Fig. 4.2 B**).

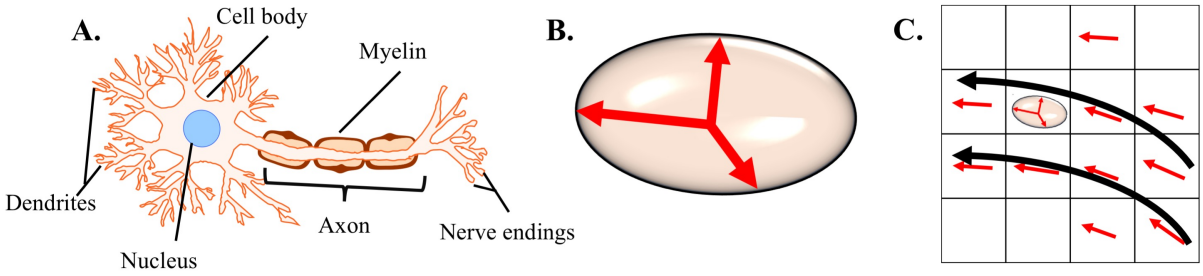

Figure 4.2. Diffusion tensor model

(A) Schematic representation of a neuron. **(B)** Ellipsoid corresponding to a magnetic resonance voxel. The red arrows correspond to the three orthogonal eigenvectors on the major, medium and minor axis. **(C)** Fibres may be traced using the principal direction in each voxel. A single ellipsoid representing the principal direction is demonstrated in one of the voxels (voxels are shown here as a grid).

As each voxel contains thousands of neurons, diffusion MRI can infer the underlying fibre orientation indirectly by estimating the diffusion of water molecules in each voxel (Herculano-Houzel, 2009; Lent et al., 2012). When axons are homogeneously aligned within each voxel, then the DTI model offers a good approximation of the principal direction of the diffusion of water molecules and consequently the fibre orientation (Alexander et al., 2011). However, fibres are known to disperse, cross or merge, known as “crossing fibres”. The proportion of the WM voxels that contains multiple fibre orientations approaches 90% (Jeurissen et al., 2013). Hence more advanced algorithms have been developed that aim to better estimate fibre trajectories. One such method is constrained spherical deconvolution (CSD) that can estimate fibre orientation from diffusion data directly. With this method, the response function could be estimated which basically represents the signal of a single coherently oriented fibre bundle (Tournier et al., 2007; Tournier et al., 2004).

This method can robustly determine the fibre orientation distribution within acceptable clinical time (under 10 minutes) (Farquharson et al., 2013). Recent studies have demonstrated the superiority of this technique over DTI in corticospinal tracks (Farquharson et al., 2013; Mormina et al., 2015).

After the voxel-wise estimation of axonal fibres, tractography approaches are used to estimate the putative connections based on the estimated principal directions **(Fig. 4.2C**). There are two main approaches: a) deterministic in which only one streamline emanates from each voxel and b) probabilistic tractography which estimates a probability for any given streamline (**Fig. 4.3**). A number of studies have assessed the test-retest reliability of tractography methods for connectome reconstruction. In general, probabilistic tractography shows greater connectome reproducibility while reducing the effect of potential misalignment errors (Zalesky et al., 2016). However, it could result to more spurious connections due to the greater spatial dispersion of the streamline trajectories (Cote et al., 2013). On the other hand, deterministic tractography results in lower connections but it shows greater variation both within and across subjects (Sotiropoulos and Zalesky, 2017). In general, there is a paradigm shift from deterministic to probabilistic tractography methods owing to the development of advanced models for streamline reconstruction.

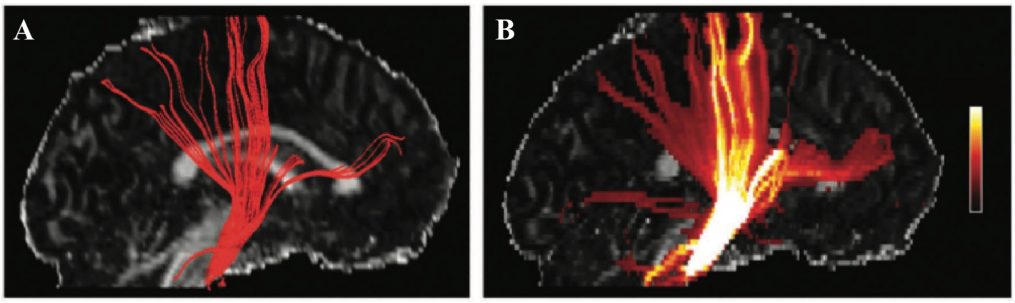

Figure 4.3. Examples of tractography

(A) Deterministic and **(B)** probabilistic tractography of the pyramidal tract overlaid on fractional anisotropy image. Colour bar represents the probability for the presence of the tract (Figure adopted from Craddock et al. (2013)).

Once the tractogram is generated between all pairs of nodes, several measures of connectivity strength are then derived. The simplest measure is the number of streamlines between two regions. However, streamlines are not really axons but rather a mathematical representation of the putative tracts thus do not really relate to connectivity strength (Jones et al., 2013). Other connectivity measures based on water diffusion in each voxel such as fractional anisotropy (FA) and apparent diffusion coefficient (ADC) are used to weight the edges of the network. FA and ADC are measures extensively used in medical research and reflect different microstructural changes. However, the use of those measures in network analysis has some intrinsic limitations including lack of sensitivity as localized disruption in one part of the tract might be masked when values are averaged across the whole tract (Jones et al., 2013; Colby et al., 2012). **Fig. 4.4** shows an example of a weighted graph in which the edges have different thickness reflecting differences in the weights.

The development of methods that improve the interpretability of streamline count as reliable measure for connectivity strength is an active research area. Such methods include anatomically constrained tractography (ACT) which provides anatomical priors that are shown to reduce known false positives (Smith et al., 2012) and spherical-deconvolution informed filtering of tractograms (SIFT2) that reweights the generated streamlines so that streamline count correlates to WM density (Smith et al., 2015b; Smith et al., 2015a). Other methods include unsupervised tractogram reconstruction using reference tracts (Clayden et al., 2009) while more recently a hierarchical clustering of streamline tractography algorithm has been proposed so that streamlines are clustered based on their anatomical neighbourhood, thus minimising random variability between subjects (Siless et al., 2018).

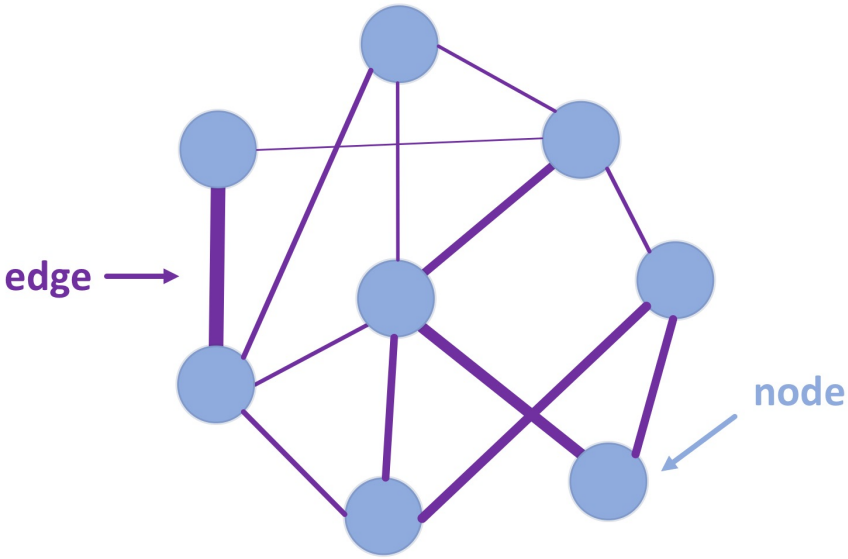

Figure 4.4. Example of a graph

A model graph demonstrating the nodes and the edges. The thickness of the connections corresponds to the weight of the connection i.e. thicker lines mean higher weights.

Connectivity matrix

Finally, irrespective of the choice of edges, the brain network is usually visualized as a connectivity matrix whose links between each pair of nodes can be shown as a binary number considering only the presence (1) or absence (0) of a connection, or as a weighted number taking a range of values (Rubinov and Sporns, 2010). In addition, there are several weighting strategies that are used to reflect the type of the pairwise connection, the most common being FA and the number of streamlines, to represent connection integrity or connection density respectively. **Fig. 4.5.** shows an example of a weighted connectivity matrix. **Fig. 4.6.** summarises the connectome reconstruction pipeline.

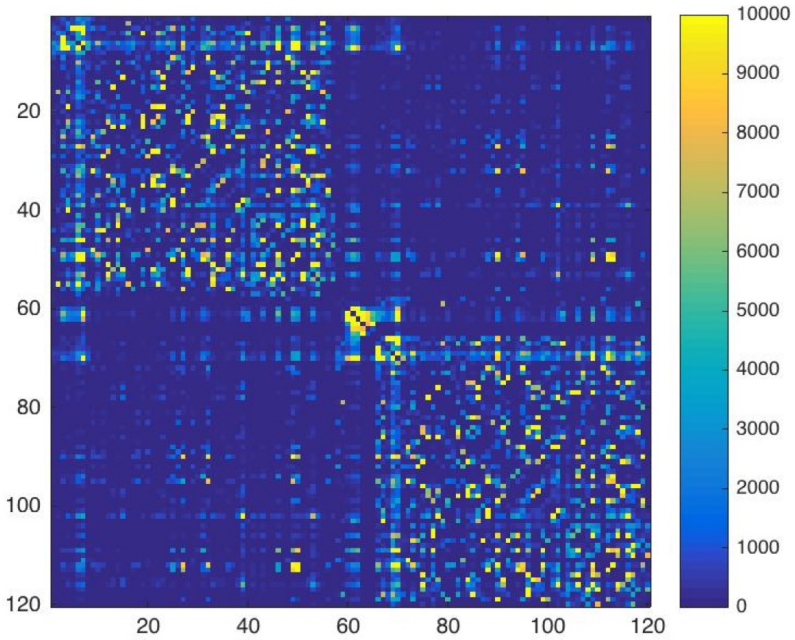

Figure 4.5. Example of a weighted connectivity matrix

The numbers on the rows and columns correspond to the nodes and the element in the matrix correspond to the number of streamlines between a pair of nodes.

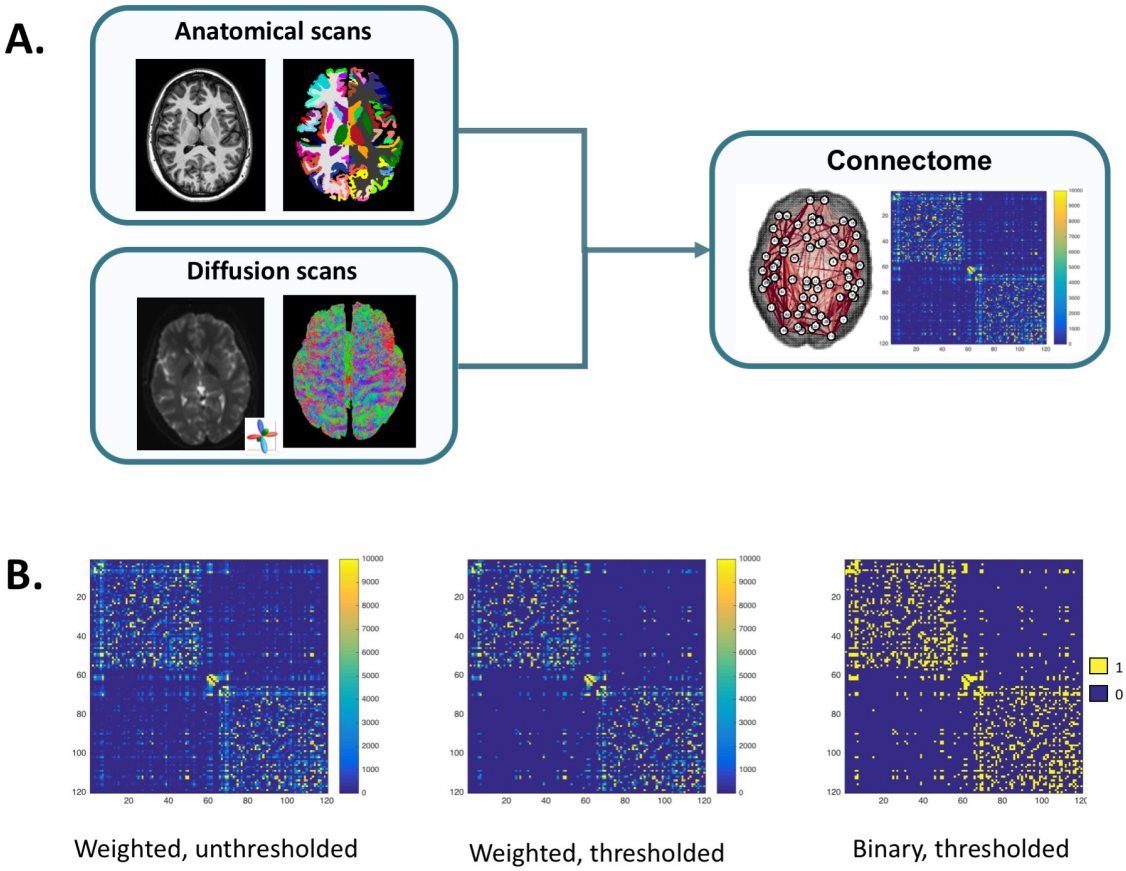

Figure 4.6. Network reconstruction pipeline

(A) Basic workflow showing the different steps for brain network (also termed as connectome) reconstruction. The anatomical and diffusion images are processed as different streams and are finally compiled into a brain connectome. **(B)** For visualization purposes the brain connectome is represented as a matrix encoding the strength and the type of connection between two brain region pairs. These pairwise connections can either be weighted (taking a range of values), unthresholded **(left)** or thresholded **(middle)** to remove spurious connections and then binarised **(right)** taking values between 0 and 1.

4.3. Graph theory in brain networks

Following brain network reconstruction, metrics from the well-established field of mathematics, graph theory, are usually derived to quantitatively summarise brain organization. Graph theory is the study of mathematical objects used to model pairwise relations between objects. It is a very broad theme with several applications in biological, physical and social systems (Rubinov and Sporns, 2010). This subsection aims to briefly introduce some popular concepts of graph theory when studying brain networks. Since in this thesis, we used weighted networks (compared to binary; see **chapter 5**) the equations for the weighted forms are provided.

The human brain is structurally and functionally organised into a complex network to facilitate integration and segregation of information processing. An integrated network is one in which each node is easily accessible by any other node. Global efficiency and characteristic path length are measures used to quantify network integration (Rubinov and Sporns, 2010). More specifically, global efficiency is defined as the average of inverse shortest path lengths and it is inversely related to the characteristic path length – that is the minimum number of steps required to travel from one node to another (Rubinov and Sporns, 2010). It corresponds to the structural capacity of information transfer between parts of the network and it is mainly associated with the long-range connections. The equation is as follows:

$$E_G^w = \frac{1}{n}\sum_{i\in N}\frac{\sum_{j\in N, j\neq i}\left(d_{ij}^w\right)^{-1}}{n-1}$$

Eq. 4.1

where n is the number of nodes and *i,j* are the nodes of the graph. $(d_{ij}^{w})^{-1}$ corresponds to the distance of the weighted shortest path length between *i,j*. This equation is a generalization from the definition of the binary unweighted networks as proposed by Latora and Marchiori (2001).

By contrast, segregation is the propensity of the network to form highly interconnected local cliques which are sparsely connected with the rest of the network and can be measured in terms of local efficiency and clustering coefficient. Local efficiency, similar to global efficiency, is defined as the average of the inverse distance matrix but in a sub-cluster of the network (Latora and Marchiori, 2001). It is considered a measure of the local information flow. As this is a node-specific measure we average over all the nodes to get the mean local efficiency metric. In this study, we used the following generalization algorithm,

$$E_l^w = \frac{1}{n}\sum_{i\in N}\frac{1}{k_i\,(k_i\,-1)}\sum_{i\in N}a_{ij}a_{ih}\left[d_{jh}^{w}(N_i)\right]^{-1}$$

Eq. 4.2

where $[d_{jh}^{w}\,(N_i)]^{-1}$ is the inverse weight of the shortest path between nodes *j* and *h* which are immediate neighbours of node *i* and a_{ij} is the connection status between *i* and *j*: a_{ij}=1 when a link *(i,j)* exists and a_{ij}=0 otherwise. k_i is the strength of the node *i* (the sum of the weight of the edges connected to it)

In addition, the clustering coefficient is a measure of local organization reflecting how well the neighbour's nodes are connected (Rubinov and Sporns, 2010).

$$C^w = \frac{1}{n}\sum_{i\in N}\frac{2t_i^w}{k_i\,(k_i\,-1)}$$

Eq. 4.3

where

$$k_i = \sum_{j\in N} a_{ij}, \qquad t_i^w = \frac{1}{2}\sum_{j,h\in N}\sqrt[3]{w_{ij}w_{ih}w_{jh}}$$

Eq. 4.4

N is the overall number nodes (for which there are n). k_i is the strength of the node *i* (the sum of the weight of the edges connected to it) and t_i^w is the sum of the geometric mean of the weights in each triangle[1].

Another concept that is used in this thesis is edge density and it is known as the connectivity of the network. It is defined as the percentage of the connections that exist relative to the potential number of connections. The equation is:

$$\rho = \frac{2E}{N(N-1)}$$

Eq. 4.5

[1] In the unweighted form, number of triangles around node *i* correspond to the number of pairs of neighbours of that node that are connected to it.

where E is the number of edges and N is the overall number of nodes. Since the derived network is undirected we divide the denominator by 2 so that any potential pairwise edge is counted once and not twice.

Further graph theory concepts have also received a lot of interest. For example, so-called “hubs” are brain regions that have higher degree (binary graph) or strength (weighted graph) (van den Heuvel and Sporns, 2013). Brain regions that are consistently identified as network hubs are the precuneus, anterior and posterior cingulate cortex, insular cortex, superior frontal cortex, temporal and lateral parietal cortex (van den Heuvel et al., 2010). Further studies have also demonstrated that brain networks can be decomposed into different modules (Meunier et al., 2009) while van den Heuvel and Sporns (2011) showed that hubs have the tendency to be more closely connected among themselves rather than nodes of lower connectivity, known as “rich-club” (**Fig. 4.5**).

Another interesting framework for brain network decomposition was introduced by Clayden et al. (2013), who showed that the network can be decomposed into stable, meaningful and reproducible “principal networks”. This data-driven approach identifies subnetworks with strong internal connectivity, allowing multiple layers of connectivity to be considered separately. Thus, principal network analysis provides a framework to study the effects of pathology on key subnetworks. This technique has been used in **chapter 9** to investigate topological organisation in MS.

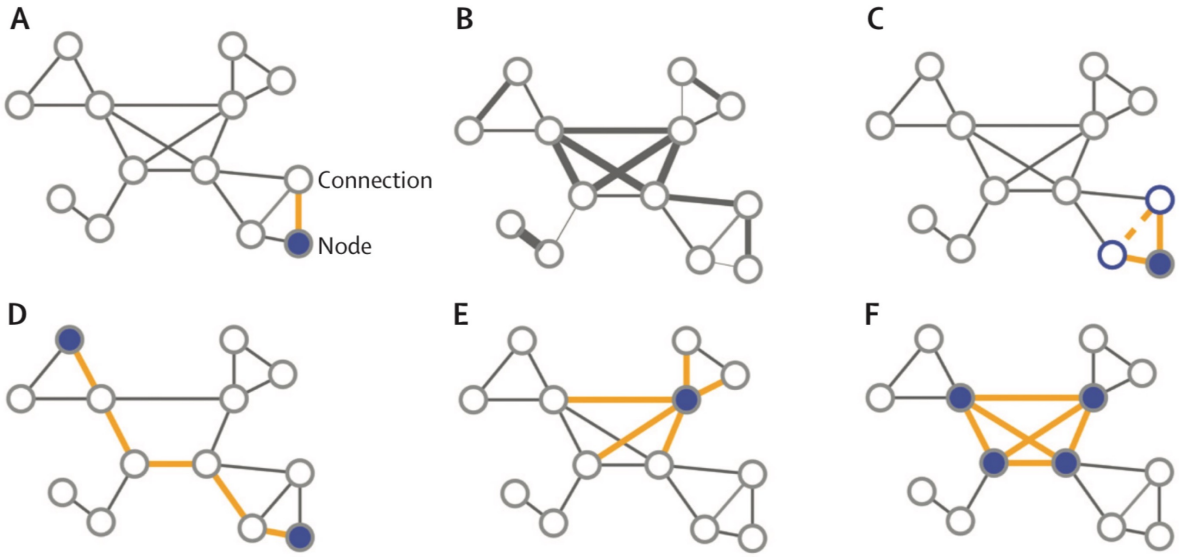

Figure 4.7. Summary of the main measures derived with graph analysis

(A) A graph is composed of nodes and edges (connections). **(B)** A weighted graph provides information regarding the strength of the connection. Higher connection weights are represented by thicker lines **(C)** The clustering coefficient describes the tendency of the nodes to form local triangles and it is a measure of local connectivity. **(D)** The shortest path length describes the minimum number of steps required to communicate between two nodes and it provides insights into the communication efficiency between those nodes. **(E)** The degree of the node describes the number of existing connections of that node. A node with many connections will have a more central role in the network and it may suggest the existence of hub nodes. **(F)** The "rich-club" organization describes the tendency of hub nodes to be more closely connected among themselves. (For each metric the node and edge of interest is always highlighted (Figure adopted from Filippi et al. (2013)).

4.4. Application of network analysis in multiple sclerosis

The preceding sections introduced the concept of the structural brain network, its reconstruction and graph theory analysis. In this section, we discuss the main findings emerging from the application of network analysis in MS. Even though several imaging modalities and methods have been used, such as cortical thickness (He et al., 2009) and electroencephalography (Van Schependom et al., 2014), here we focus on DWI-based networks.

One of the first studies looking at networks constructed with DWI data was conducted by Shu et al. (2011). The authors constructed FA-weighted and number of streamlines-weighted brain networks and showed decreased global and local network efficiencies in 39 RRMS patients compared to healthy volunteers. These differences were correlated with WM LL, EDSS scores (disability score) and disease duration (Shu et al., 2011). Going a step further, Li and colleagues introduced a new metric, namely "communicability", that accounts for "both direct and indirect connections" in an attempt to quantify network differences that are not "lesion-related". They showed decreased communicability in several brain areas, whereas increases in this metric were observed in DGM structures suggestive of "compensatory mechanisms" in early RRMS (Li et al., 2013).

Recent studies have further investigated network changes in MS and subtypes. Pardini and colleagues showed that global efficiency of the motor network, derived from composite measures (FA, MTR and tract volume), correlates better than conventional imaging metrics with EDSS score in RRMS and SPMS patients (Pardini et al., 2015). Other studies showed further network alterations that highlight the possibility of structural adaptations at early stages of the disease in order to preserve

cognitive function (Muthuraman et al., 2016; Fleischer et al., 2016; Llufriu et al., 2016). Finally, two independent studies developed a method that allowed the automatic classification of MS patients into different clinical profiles (Muthuraman et al., 2016; Kocevar et al., 2016), highlighting the fact that MS subtypes share different underlying network properties.

Longitudinal studies are imperative to investigate disease progression. For instance, Bodini et al. (2016) have reported evidence that cortical damage is the sequence of normal appearing WM pathology, which in turn is predicted by abnormalities within WM lesions, while a study by Tur et al. (2016) provided longitudinal evidence of anterograde trans-synaptic degeneration in optic neuritis patients. Both studies used diffusion-weighted imaging for their investigation. Currently, there are no longitudinal studies from a network perspective. Longitudinal network approaches hold the potential to study dynamics of network function over time, evaluate network alterations in disease and investigate whether these constitute processes that partially or fully compensate for tissue loss in the absence of any clinical decline.

To conclude this chapter, we can appreciate the variability of the techniques that lead to network reconstruction in the absence of any standardised pipelines: from node selection to modelling crossing fibres, and from the various tractography algorithms to the various weighting schemes (i.e. FA or number of streamlines) of the network. And finally, the resulting matrix can be thresholded and/or binarised in a subjective way. Each of these steps/techniques has been developed and used with the goal of improving the biological basis of the resulting network. Despite the plethora of choices, which might be paradoxically considered as caveats as the results are not easily generalisable, some interesting patterns have emerged. With the ongoing,

active research in the field, acknowledging the current limitations, it will not be long until we see some further developments that could lead to more widespread usage of network analysis, especially in clinical practise.

4.5. Remaining questions and research aims of this thesis

The brain connectome is a conceptual framework that allows a holistic rather than reductionist study of the brain. This is particularly important in diseases such as MS where diffused pathogenic processes cannot be captured by conventional imaging techniques. As discussed, network analysis is a multistep procedure with no consensus on optimal network construction, and several decisions should be made during the process which can influence subsequent analysis. In **chapter 5**, we are going to present the various steps taken during the network reconstruction pipeline that was optimised and used in this thesis, using advanced techniques that aimed to minimise tracking biases thus making the resulting network more biologically plausible. Using this pipeline, we then investigated whether network metrics can explain disability over and above brain atrophy and lesional metrics in **chapter 6**. In the absence of any longitudinal network studies, in **chapter 7,** we developed and validated a longitudinal network framework which we then applied in **chapter 8** to investigate whether baseline network metrics can predict future brain damage. Up to this stage, network metrics were derived from the whole brain and thus in **chapter 9** we used a novel data-driven brain decomposition method to study whether brain different topological organisation exists in MS subtypes.

Bibliography

Alexander AL, Hurley SA, Samsonov AA, et al. (2011) Characterization of cerebral white matter properties using quantitative magnetic resonance imaging stains. *Brain Connect* 1: 423-446.

Arslan S, Ktena SI, Makropoulos A, et al. (2018) Human brain mapping: A systematic comparison of parcellation methods for the human cerebral cortex. *Neuroimage* 170: 5-30.

Barkhof F. (2002) The clinico-radiological paradox in multiple sclerosis revisited. *Curr Opin Neurol* 15: 239-245.

Bodini B, Chard D, Altmann DR, et al. (2016) White and gray matter damage in primary progressive MS: The chicken or the egg? *Neurology* 86: 170-176.

Bodini B, Khaleeli Z, Cercignani M, et al. (2009) Exploring the relationship between white matter and gray matter damage in early primary progressive multiple sclerosis: an in vivo study with TBSS and VBM. *Hum Brain Mapp* 30: 2852-2861.

Cardoso MJ, Modat M, Wolz R, et al. (2015) Geodesic Information Flows: Spatially-Variant Graphs and Their Application to Segmentation and Fusion. *IEEE Trans Med Imaging* 34: 1976-1988.

Catani M and Mesulam M. (2008) What is a disconnection syndrome? *Cortex* 44: 911-913.

Clayden JD, Dayan M and Clark CA. (2013) Principal networks. *PLoS ONE* 8: e60997.

Clayden JD, Storkey AJ, Munoz Maniega S, et al. (2009) Reproducibility of tract segmentation between sessions using an unsupervised modelling-based approach. *Neuroimage* 45: 377-385.

Colby JB, Soderberg L, Lebel C, et al. (2012) Along-tract statistics allow for enhanced tractography analysis. *Neuroimage* 59: 3227-3242.

Cote MA, Girard G, Bore A, et al. (2013) Tractometer: towards validation of tractography pipelines. *Med Image Anal* 17: 844-857.

Craddock RC, Jbabdi S, Yan CG, et al. (2013) Imaging human connectomes at the macroscale. *Nat Methods* 10: 524-539.

Crick CF and Koch C. (2005) What is the Function of the Claustrum. *Philosophical Transactions: Biological Sciences* 360.

Evans AC, Janke AL, Collins DL, et al. (2012) Brain templates and atlases. *Neuroimage* 62: 911-922.

Farquharson S, Tournier JD, Calamante F, et al. (2013) White matter fiber tractography: why we need to move beyond DTI. *J Neurosurg* 118: 1367-1377.

Filippi M and Agosta F. (2010) Imaging biomarkers in multiple sclerosis. *J Magn Reson Imaging* 31: 770-788.

Filippi M, van den Heuvel MP, Fornito A, et al. (2013) Assessment of system dysfunction in the brain through MRI-based connectomics. *The Lancet Neurology* 12: 1189-1199.

Fisniku LK, Brex PA, Altmann DR, et al. (2008a) Disability and T2 MRI lesions: a 20-year follow-up of patients with relapse onset of multiple sclerosis. *Brain* 131: 808-817.

Fleischer V, Groger A, Koirala N, et al. (2016) Increased structural white and grey matter network connectivity compensates for functional decline in early multiple sclerosis. *Mult Scler*.
Geschwind N and Kaplan E. (1962) A human cerebral deconnection syndrome; a preliminary report. *Neurology*.
Hagmann P, Cammoun L, Gigandet X, et al. (2008) Mapping the structural core of human cerebral cortex. *PLoS Biol* 6: e159.
He Y, Chen ZJ and Evans AC. (2007) Small-world anatomical networks in the human brain revealed by cortical thickness from MRI. *Cereb Cortex* 17: 2407-2419.
He Y, Dagher A, Chen Z, et al. (2009) Impaired small-world efficiency in structural cortical networks in multiple sclerosis associated with white matter lesion load. *Brain* 132: 3366-3379.
Hebb D. (1949) *The Organization of Behavior,* New York Wiley & Sons.
Herculano-Houzel S. (2009) The human brain in numbers: a linearly scaled-up primate brain. *Front Hum Neurosci* 3: 31.
Jeurissen B, Leemans A, Tournier JD, et al. (2013) Investigating the prevalence of complex fiber configurations in white matter tissue with diffusion magnetic resonance imaging. *Hum Brain Mapp* 34: 2747-2766.
Jones DK. (2008) Studying connections in the living human brain with diffusion MRI. *Cortex* 44: 936-952.
Jones DK, Knosche TR and Turner R. (2013) White matter integrity, fiber count, and other fallacies: the do's and don'ts of diffusion MRI. *Neuroimage* 73: 239-254.
Kaiser M. (2011) A tutorial in connectome analysis: topological and spatial features of brain networks. *Neuroimage* 57: 892-907.
Klein A and Tourville J. (2012) 101 labeled brain images and a consistent human cortical labeling protocol. *Front Neurosci* 6: 171.
Kocevar G, Stamile C, Hannoun S, et al. (2016) Graph Theory-Based Brain Connectivity for Automatic Classification of Multiple Sclerosis Clinical Courses. *Front Neurosci* 10: 478.
Latora V and Marchiori M. (2001) Efficient behavior of small-world networks. *Phys Rev Lett* 87: 198701.
Lent R, Azevedo FA, Andrade-Moraes CH, et al. (2012) How many neurons do you have? Some dogmas of quantitative neuroscience under revision. *Eur J Neurosci* 35: 1-9.
Li Y, Jewells V, Kim M, et al. (2013) Diffusion tensor imaging based network analysis detects alterations of neuroconnectivity in patients with clinically early relapsing-remitting multiple sclerosis. *Hum Brain Mapp* 34: 3376-3391.
Lichtman JW, Pfister H and Shavit N. (2014) The big data challenges of connectomics. *Nat Neurosci* 17: 1448-1454.
Llufriu S, Martinez-Heras E, Solana E, et al. (2016) Structural networks involved in attention and executive functions in multiple sclerosis. *NeuroImage: Clinical*.
Meunier D, Lambiotte R, Fornito A, et al. (2009) Hierarchical modularity in human brain functional networks. *Front Neuroinform* 3: 37.
Mormina E, Longo M, Arrigo A, et al. (2015) MRI Tractography of Corticospinal Tract and Arcuate Fasciculus in High-Grade Gliomas Performed by Constrained Spherical Deconvolution: Qualitative and Quantitative Analysis. *AJNR Am J Neuroradiol* 36: 1853-1858.

Muthuraman M, Fleischer V, Kolber P, et al. (2016) Structural Brain Network Characteristics Can Differentiate CIS from Early RRMS. *Front Neurosci* 10: 14.
Oh SW, Harris JA, Ng L, et al. (2014) A mesoscale connectome of the mouse brain. *Nature* 508: 207-214.
Pardini M, Yaldizli O, Sethi V, et al. (2015) Motor network efficiency and disability in multiple sclerosis. *Neurology* 85: 1115-1122.
Park HJ and Friston K. (2013) Structural and functional brain networks: from connections to cognition. *Science* 342: 1238411.
Ramón y Cajal S. (1892) *The Structure of the Retina,* Illinois: Springfield.
Rocca MA, Colombo B, Falini A, et al. (2005) Cortical adaptation in patients with MS: a cross-sectional functional MRI study of disease phenotypes. *Lancet Neurol* 4: 618-626.
Rubinov M and Sporns O. (2010) Complex network measures of brain connectivity: uses and interpretations. *Neuroimage* 52: 1059-1069.
Shu N, Liu Y, Li K, et al. (2011) Diffusion tensor tractography reveals disrupted topological efficiency in white matter structural networks in multiple sclerosis. *Cereb Cortex* 21: 2565-2577.
Siless V, Chang K, Fischl B, et al. (2018) AnatomiCuts: Hierarchical clustering of tractography streamlines based on anatomical similarity. *Neuroimage* 166: 32-45.
Smith RE, Tournier JD, Calamante F, et al. (2012) Anatomically-constrained tractography: improved diffusion MRI streamlines tractography through effective use of anatomical information. *Neuroimage* 62: 1924-1938.
Smith RE, Tournier JD, Calamante F, et al. (2015a) The effects of SIFT on the reproducibility and biological accuracy of the structural connectome. *Neuroimage* 104: 253-265.
Smith RE, Tournier JD, Calamante F, et al. (2015b) SIFT2: Enabling dense quantitative assessment of brain white matter connectivity using streamlines tractography. *Neuroimage* 119: 338-351.
Sotiropoulos SN and Zalesky A. (2017) Building connectomes using diffusion MRI: why, how and but. *NMR Biomed*.
Sporns O, Tononi G and Kotter R. (2005) The human connectome: A structural description of the human brain. *PLoS Comput Biol* 1: e42.
Thompson AJ, Baranzini SE, Geurts J, et al. (2018b) Multiple sclerosis. *The Lancet*.
Tournier JD, Calamante F and Connelly A. (2007) Robust determination of the fibre orientation distribution in diffusion MRI: non-negativity constrained super-resolved spherical deconvolution. *Neuroimage* 35: 1459-1472.
Tournier JD, Calamante F, Gadian DG, et al. (2004) Direct estimation of the fiber orientation density function from diffusion-weighted MRI data using spherical deconvolution. *Neuroimage* 23: 1176-1185.
Tur C, Goodkin O, Altmann DR, et al. (2016) Longitudinal evidence for anterograde trans-synaptic degeneration after optic neuritis. *Brain* 139: 816-828.
van den Heuvel MP, Mandl RC, Stam CJ, et al. (2010) Aberrant frontal and temporal complex network structure in schizophrenia: a graph theoretical analysis. *J Neurosci* 30: 15915-15926.
van den Heuvel MP and Sporns O. (2011) Rich-club organization of the human connectome. *J Neurosci* 31: 15775-15786.
van den Heuvel MP and Sporns O. (2013) Network hubs in the human brain. *Trends Cogn Sci* 17: 683-696.

Van Schependom J, Gielen J, Laton J, et al. (2014) Graph theoretical analysis indicates cognitive impairment in MS stems from neural disconnection. *Neuroimage Clin* 4: 403-410.
Zalesky A, Fornito A, Cocchi L, et al. (2016) Connectome sensitivity or specificity: which is more important? *Neuroimage*.

Chapter 5

5. Optimization of the structural network pipeline for baseline analysis

Summary

In this chapter, we present the work performed to optimise the network reconstruction pipeline to be used in subsequent clinical studies (presented in chapters 6-9). We employed the latest advances in the field of connectomics, which include anatomically constrained tractography and spherical-deconvolution informed filtering of tractograms for diffusion processing in order to minimise structural connectivity biases. This chapter presents the main output steps during the reconstruction process in a small cohort that constitutes healthy subjects and multiple sclerosis patients. Additionally, it demonstrates that the optimised pipeline is highly reproducible and remains stable across subjects. The yielded network shares features with previous studies that employed techniques similar to the ones applied here. This chapters concludes that the proposed pipeline minimises the reconstruction biases and constitutes the derived network biologically plausible, suitable for structural connectivity studies.

Scientific contribution

The contents of this chapter are included in the methods section in a manuscript that is currently under review in *Journal of Neurology, Neurosurgery and Psychiatry*: **"Structural network disruption markers explain disability in multiple sclerosis".**

5.1. Introduction

As discussed in **chapter 4**, brain networks derived from DWI can be reconstructed by compiling pre-processed diffusion MRI images with pre-processed structural MRI images. DWI and tractography techniques can be used to indirectly reconstruct the trajectories and estimate microstructural properties of WM fibre bundles. Despite promising applications in many neurological disorders including MS, many problems are associated with structural connectome quantification (Jones et al., 2013; Sotiropoulos and Zalesky, 2017) some of which are associated with the processing steps themselves. Network reconstruction is a multistep process and each step needs to be carefully examined otherwise it could become a potential source of error (bias) that might have negative effects in the final analysis (Griffa et al., 2013).

Additionally, for the brain network reconstructions to provide biologically meaningful information, the derived network should provide metrics that are biologically relevant such as density of WM connection between brain regions (Sporns et al., 2005). However, due to the fact that raw streamline counts provide an unreliable quantitative marker of fibre connectivity (Jones et al., 2013), diffusion metrics such as FA are usually employed. However, such metrics are rather indirect (Jones et al., 2013) or they become unreliable in regions where fibre distribution is complex, i.e. ‘crossing fibres’ which represent up to 90% of WM voxels (Jeurissen et al., 2013). Therefore, the focus of recent studies was to eliminate abnormal streamline termination in WM and CSF, which is not biologically plausible (Smith et al., 2012), and to make streamline density a reliable measure of WM density (Smith et al., 2015a).

With these in mind, the aims of work presented in this chapter were:

1. to use the recently developed state-of-art techniques that minimise tracking biases to optimize a connectome pipeline
2. to quality assess the output of each processing step in healthy controls (HC) and MS patients and
3. to validate the generated network.

5.2. Methods

5.2.1. Participants

For this study, we chose five healthy controls and five MS patients from an existing database. Subjects were selected randomly, although for the five chosen MS patients one was RRMS, one was PPMS and three were SPMS to ensure a representative range of the disease spectrum. Each optimization step was evaluated by visual inspection for the subjects. After this, 12 HC were analysed in order to validate the generated pipeline. This work has been approved by the local institutional ethics committee and written consent was obtained from all the patients.

5.2.2. MRI data acquisition

Brain MRI data were acquired using a Philips Achieva 3T MR scanner (Philips Healthcare, Best, Netherlands) using a 32-channel coil. The high angular resolution diffusion imaging (HARDI) scan consisted of a cardiac-gated spin-echo (SE) sequence with echo planar imaging (EPI) readout (resolution = 2x2x2 mm^3, repetition time (TR) = 24000 ms; echo time (TE) = 68 ms; 61 isotropically distributed diffusion-weighted directions, b-value = 1200 s/mm^2, 7 b = 0 volumes, matrix size 112 x 112, number of slices 72). In each subject, the following data was also acquired: (1) T1-weighted scans were also acquired using a 3D fast-field echo scan (resolution = 1x1x1 mm^3, TR = 6.9 ms, TE = 3.1 ms, inversion time (TI) = 824.5 ms) and (2) dual-echo proton density/T2-weighted axial oblique scans (resolution = 1x1x1 mm^3, TR = 3500 ms, TE = 19/85 ms, field of view 240x180, number of slices 50). All data were acquired with slices aligned with the anterior commissure (AC) – posterior commissure (PC) line to minimise the effect of head positioning on data analysis.

5.2.3. Structural imaging processing

Bias field correction of structural imaging

To correct for magnetic field inhomogeneity, structural images were bias field corrected using the N4 algorithm (Tustison et al., 2010).

Lesion filling

For WM lesion detection, T2-hyper intense lesions were manually delineated from the proton density (PD)-weighted scans using JIM (v6.0, Xinapse Systems, Aldwincle, UK). The PD-weighted lesion masks were registered to T1-weighted scans using pseudo-T1 image as previously described (Hickman et al., 2002).

Registration between T1-weighted and diffusion-weighted image

A rigid-body transformation was performed to register the subject's T1-weighted image to the corresponding DWI image using BrainSuite (Bhushan et al., 2012), where the target volume was the first b0 image after DWI pre-processing, resulting in a structural image of resolution = 2x2x2 mm^3 (Smith et al., 2012). The purpose of registering the structural images to the diffusion images at this stage is two-fold: a) matching the voxel dimensions and positions of the T1-scan to that of DWI means that any subsequent image derived from the anatomical scan will be inherently aligned to the DWI and b) aligning the anatomical image to the DWI and not the other way around ensures that re-orientation of the gradient directions is not required.

Tissue segmentation and parcellation

We non-rigidly transformed the lesions to DWI space and then filled the T1-weighted images in this space using a modality-agnostic patch-based method (Prados et al., 2016b). The reason that we registered the T1-image in DWI space before lesion filling

is so that we matched all the anatomical features between the two modalities including lesions. Hence, we ensured that the non-rigid registration was not affected by the lesion filling technique. The filled T1-weighted images in low resolution were then segmented into cortical grey matter (CGM), WM, DGM, brainstem and CSF and parcellated into anatomically distinct regions according to Desikan–Killiany–Tourville atlas protocol using the GIF framework (Cardoso et al., 2015). This method has been previously used in different neurological diseases such as MS (Eshaghi et al., 2018), dementia (Premi et al., 2017) and epilepsy (Taylor et al., 2017). GIF is freely available as web-service at http://cmictig.cs.ucl.ac.uk/niftyweb (Prados et al., 2016a). The full list of brain regions generated with GIF are shown in **Table 5.1**. The generated WM and brainstem tissues were joined together to form the appropriate tissue used for ACT algorithm. ACT provides the anatomical prior to improve the accuracy of the reconstructed streamlines (Smith et al., 2012).

5.2.4. Diffusion-weighting imaging processing

Diffusion-weighted imaging pre-processing

The mean b0 image was rigid registered to the first b0 image. Then, the same rigid transformation was applied to the 61 DWI volumes. FSL v5.0.9 was used on the DWI data to correct for eddy current and head motion using affine registration to the first b0 (Andersson and Sotiropoulos, 2016). We also corrected the geometric distortions caused by EPI sequences using BrainSuite v15b (Bhushan et al., 2012). As discussed in **chapter 4**, EPI sequences are quite sensitive to inhomogeneities of the magnetic field resulting in localised distortions particularly at the interface between tissue, bone and air.

Model response function and perform constrained spherical deconvolution

For estimation of the response function, that is the signal expected from a voxel that contains a single coherent fibre bundle, we used the Tax algorithm (Tax et al., 2014). Then, CSD was performed to estimate the voxel-wise fibre orientation distribution functions (fODFs) (Tournier et al., 2007; Tournier et al., 2004).

Whole-brain streamline tractography

For each subject, 10^7 streamlines were generated using the "dynamic seeding mechanism" (Smith et al., 2015b). For probabilistic tractography, the 2nd-order Integration over Fibre Orientation Distributions (iFOD2) algorithm (Tournier et al., 2010) was employed, implementing the ACT framework (Smith et al., 2012). As a test, we also generated a tractogram containing 10^8 streamlines for two subjects. Moreover, in MS, tractography algorithms are known to be hampered by the presence of lesions (Sotiropoulos and Zalesky, 2017). Thus, in our approach, during tractogram reconstruction we provided anatomical prior of the WM as part of the ACT algorithm ensuring that no streamlines are incorrectly terminated in the WM due to the lesions. To validate this, we also ran the tractography in a subject for which lesion masks were not provided during the tractography step and tested the effects on the derived tractogram **(Fig. 5.8)**. We chose the 10^7 streamline tractogram as the default and SIFT2 was applied to modulate the contribution of each streamline to the relevant edge (Smith et al., 2015b).

5.4.5. Connectome reconstruction

Brain GM parcellations were selected from whole brain parcellation derived from GIF (Cardoso et al., 2015) and constituted the GM nodes of the network. A symmetric matrix consisting of 120 nodes was constructed. Each network edge was defined as the sum of weights of streamlines connecting a pair of nodes (Smith et al., 2015b).

5.4.6. Reproducibility

To test the reproducibility of our findings, we used a split-half method. Briefly, we divided the control group into 2 subgroups according to the distributions of age and gender; controls1: 6 participants, 3 females; controls2: 6 participants, 3 females. To determine whether there was a consistent topological organisation in the population we used Student's t-test to compare the edge density between the two subgroups.

As, discussed in chapter 4**, edge density**, is defined as

$$\rho = \frac{2E}{N(N-1)}$$

Eq. 5.1.

where *E* is the number of edges and *N* is the number of nodes. The definition is the same for weighted and binary matrices. Edge density was derived from TractoR (http://www.tractor-mri.org.uk; (Clayden et al., 2011)).

We also identified network **hubs**. Hubs are nodes with central role in the network and there are several ways with which they can be identified (van den Heuvel and Sporns, 2013). Here, hubs were defined as regions that exhibited high strength (K^w; ≥ mean + standard deviation (SD)) (Shu et al., 2011; Yeh et al., 2016) resulting

in 18 regions. In brain terms, hubs are generally considered as brain areas that are important for enabling efficient neuronal signalling and communication.

5.3. Results

The output files for each step were visually inspected. In this section, we shall demonstrate images of the main processing steps.

Quality assessment of the structural images

Firstly, the anatomical images were bias field corrected **(Fig. 5.1.B)**. This step is necessary as the segmentation and parcellation algorithms rely on intensity homogeneity to accurately delineate CSF, GM and WM. The anatomical images were subsequently lesion filled **(Fig. 5.1.D,F)**, as lesions in the brain can affect the estimation of the segmentation parameters (Chard et al., 2010) and then processed using GIF (Cardoso et al., 2015) to generate brain tissue parcellation and segmentation. **Fig. 5.3** and **Fig. 5.4** show an example of brain parcellation and segmentation respectively.

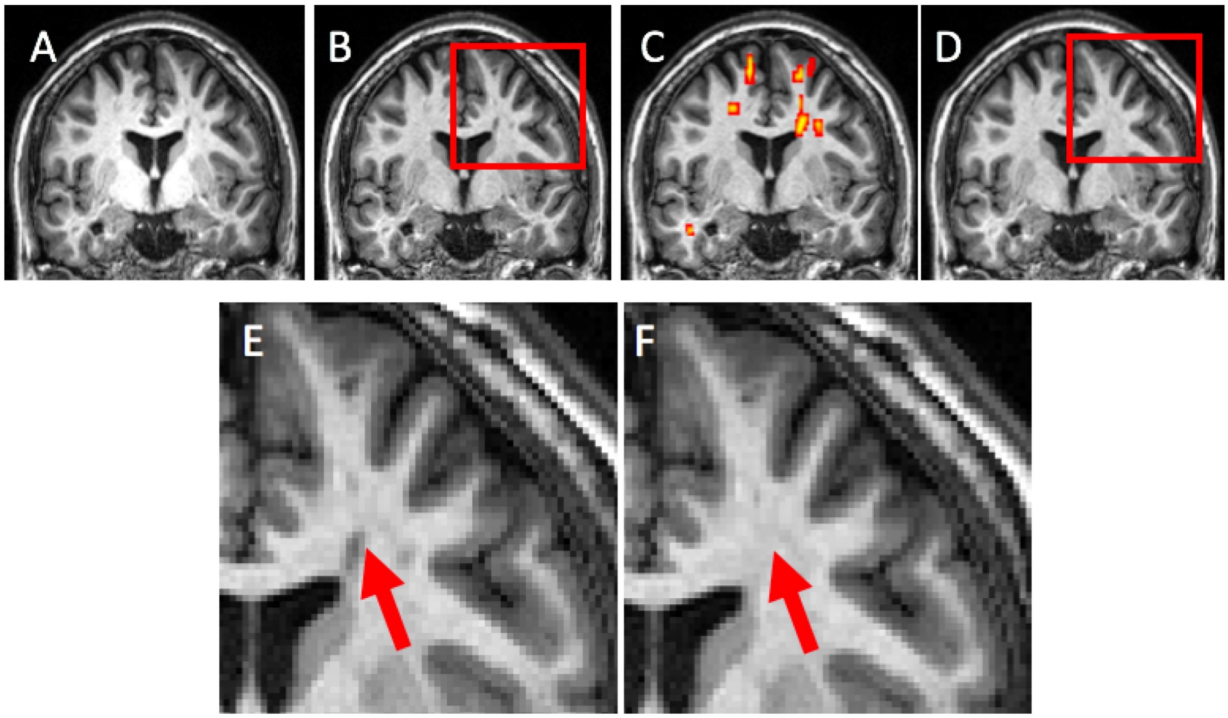

Figure 5.1. Anatomical images pre-processing

(A) Raw T1-weighted image, **(B)** T1-weighted was bias field corrected i.e. the intensity inhomogeneity (the increased brightness) that it is observed in the centre of the scan in **(A)** is removed in **(B)**. **(C)** The lesion probability masks (red-yellow masks) overlaid on T1-weighted image. **(D)** Lesion filled T1-weighted image. Red arrow in **(E)** point at a lesion (voxels with lower intensity than expected) which was subsequently filled in **(F)** using a modality-agnostic patch-based approach (Prados et al., 2016b). Red boxes in **(B)** and **(D)** show the area that is magnified in **(E)** and **(F)**, respectively.

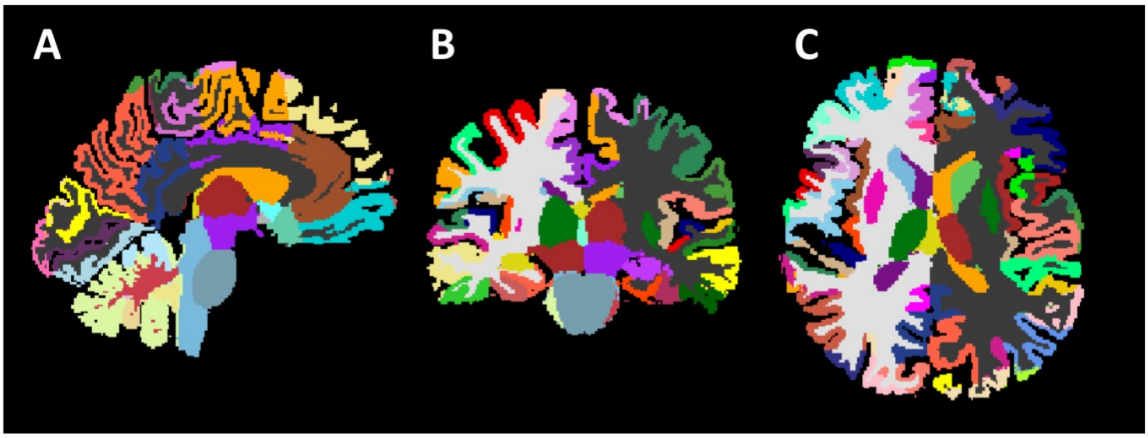

Figure 5.2. Brain parcellation

The brain tissue is divided into non-overlapping, distinct regions as depicted by the different colours. **(A)** sagittal, **(B)** coronal, **(C)** transverse plane.

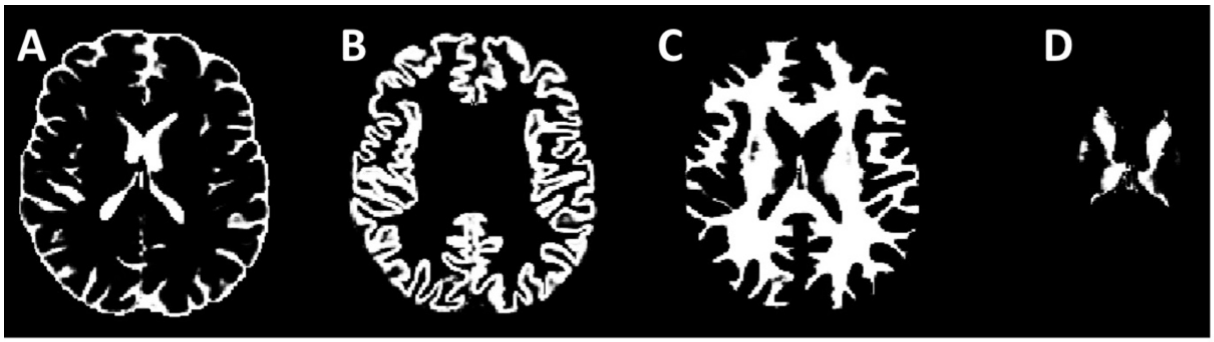

Figure 5.3. Brain tissue segmentation

The brain tissue is segmented into 5 tissue types, **(A)** CSF, **(B)** CGM, **(C)** WM, **(D)** DGM and brainstem. Note that the brainstem is not depicted in the above figures as the image was captured at a level where brainstem was not visible.

Brain regions			
1	Right Accumbens Area	61	Right middle occipital gyrus
2	Left Accumbens Area	62	Left middle occipital gyrus
3	Right Amygdala	63	Right medial orbital gyrus
4	Left Amygdala	64	Left medial orbital gyrus
5	Brain Stem And Pons	65	Right postcentral gyrus medial segment
6	Right Caudate	66	Left postcentral gyrus medial segment
7	Left Caudate	67	Right precentral gyrus medial segment
8	Right Cerebellum Exterior	68	Left precentral gyrus medial segment
9	Left Cerebellum Exterior	69	Right superior frontal gyrus medial segment
10	Right Hippocampus	70	Left superior frontal gyrus medial segment
11	Left Hippocampus	71	Right middle temporal gyrus
12	Right Pallidum	72	Left middle temporal gyrus
13	Left Pallidum	73	Right occipital pole
14	Right Putamen	74	Left occipital pole
15	Left Putamen	75	Right occipital fusiform gyrus
16	Right Thalamus Proper	76	Left occipital fusiform gyrus
17	Left Thalamus Proper	77	Right opercular part of the inferior frontal gyrus
18	Cerebellar Vermal Lobules I-V	78	Left opercular part of the inferior frontal gyrus
19	Cerebellar Vermal Lobules VI-VII	79	Right orbital part of the inferior frontal gyrus
20	Cerebellar Vermal Lobules VIII-X	80	Left orbital part of the inferior frontal gyrus
21	Left Basal Forebrain	81	Right posterior cingulate gyrus
22	Right Basal Forebrain	82	Left posterior cingulate gyrus
23	Right anterior cingulate gyrus	83	Right precuneus
24	Left anterior cingulate gyrus	84	Left precuneus
25	Right anterior insula	85	Right parahippocampal gyrus
26	Left anterior insula	86	Left parahippocampal gyrus
27	Right anterior orbital gyrus	87	Right posterior insula
28	Left anterior orbital gyrus	88	Left posterior insula
29	Right angular gyrus	89	Right parietal operculum
30	Left angular gyrus	90	Left parietal operculum
31	Right calcarine cortex	91	Right postcentral gyrus
32	Left calcarine cortex	92	Left postcentral gyrus
33	Right central operculum	93	Right posterior orbital gyrus
34	Left central operculum	94	Left posterior orbital gyrus
35	Right cuneus	95	Right planum polare
36	Left cuneus	96	Left planum polare
37	Right entorhinal area	97	Right precentral gyrus
38	Left entorhinal area	98	Left precentral gyrus
39	Right frontal operculum	99	Right planum temporale
40	Left frontal operculum	100	Left planum temporale
41	Right frontal pole	101	Right subcallosal area

42	Left frontal pole	102	Left subcallosal area
43	Right fusiform gyrus	103	Right superior frontal gyrus
44	Left fusiform gyrus	104	Left superior frontal gyrus
45	Right gyrus rectus	105	Right supplementary motor cortex
46	Left gyrus rectus	106	Left supplementary motor cortex
47	Right inferior occipital gyrus	107	Right supramarginal gyrus
48	Left inferior occipital gyrus	108	Left supramarginal gyrus
49	Right inferior temporal gyrus	109	Right superior occipital gyrus
50	Left inferior temporal gyrus	110	Left superior occipital gyrus
51	Right lingual gyrus	111	Right superior parietal lobule
52	Left lingual gyrus	112	Left superior parietal lobule
53	Right lateral orbital gyrus	113	Right superior temporal gyrus
54	Left lateral orbital gyrus	114	Left superior temporal gyrus
55	Right middle cingulate gyrus	115	Right temporal pole
56	Left middle cingulate gyrus	116	Left temporal pole
57	Right medial frontal cortex	117	Right triangular part of the inferior frontal gyrus
58	Left medial frontal cortex	118	Left triangular part of the inferior frontal gyrus
59	Right middle frontal gyrus	119	Right transverse temporal gyrus
60	Left middle frontal gyrus	120	Left transverse temporal gyrus

Table 5.1. List of generated grey matter regions

Quality assessment of the diffusion-weighted images

After we corrected for eddy-currents and geometric distortions (**Fig. 5.4**), we estimated the fODF and tested its performance in voxels that are known to have crossing fibres and no crossing fibres **(Fig. 5.5)**. Then, a whole brain probabilistic tractography was performed using the ACT framework. **Fig. 5.6** shows that the generated tractogram was confined to WM as expected. **Fig. 5.7** demonstrates an example of misregistration between b0 and DWI that can have detrimental effects on subsequent steps. **Fig. 5.8** shows that no streamlines are abnormally terminated in WM due to WM lesions.

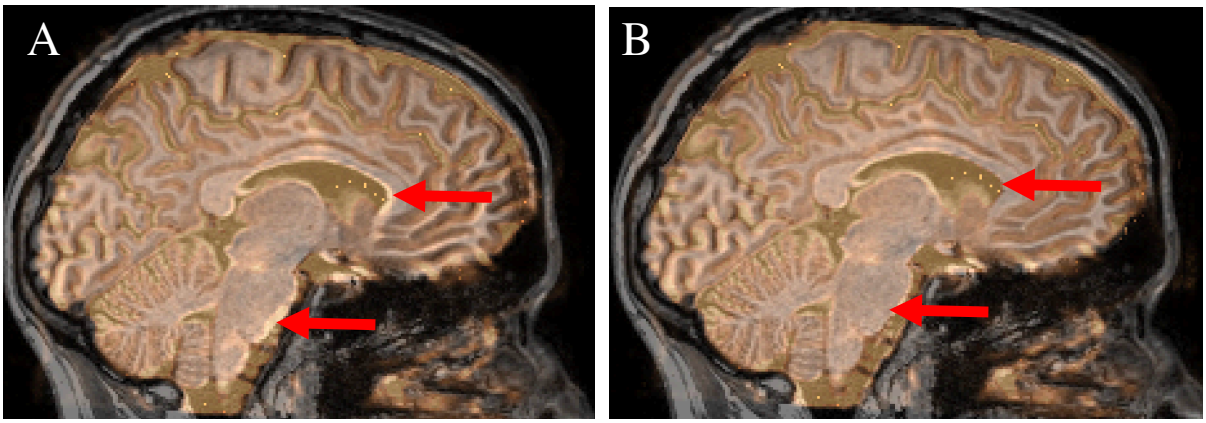

Figure 5.4. Geometric distortion correction

Uncorrected **(A)** and corrected **(B)** for geometric distortion b0 image without diffusion weighting overlaid on anatomical T1-weighted image. The arrows point are regions where the corrections are more prominent.

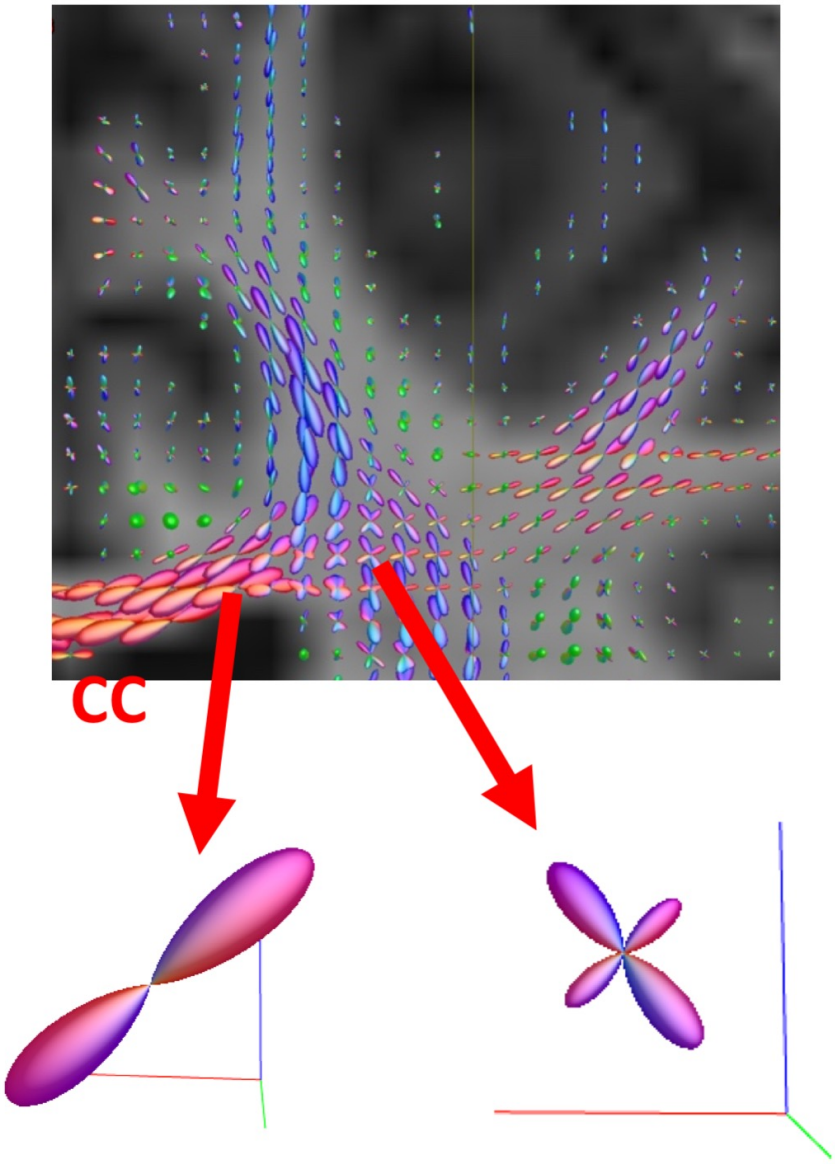

Figure 5.5. Voxel-wise fibre orientation distribution

Fibre orientation distributions (FOD) overlaid on T1-weighted image. The data were visually inspected at two places as the arrows point. **Right**: corpus callosum where we expect no crossing fibres, and this is validated by the magnified FOD which has only two lobes and **Left**: at an area where we expect crossing fibres i.e. at the intersection between callosal fibres and corticospinal tracts. The crossing fibres are modelled by FOD by having 4 lobes. **CC**; corpus callosum

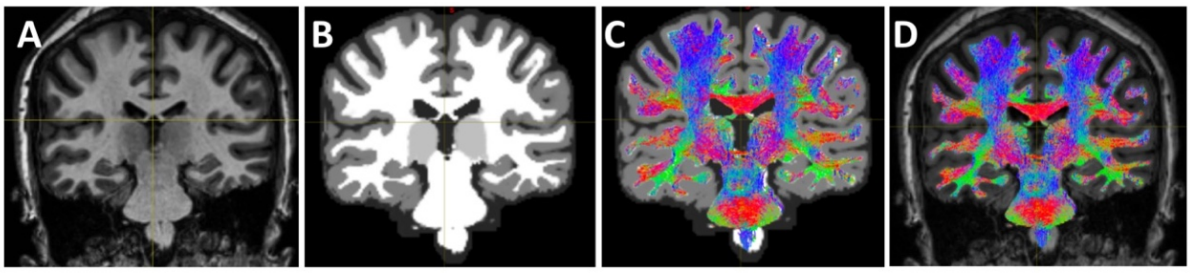

Figure 5.6. Whole brain probabilistic tractography

T1-weighted anatomical image **(A)** was segmented into CGM, WM and DGM **(B)**. In **(C)** and **(D)** the generated tractogram was overlaid on the segmented and anatomical image respectively for visual inspection. The generated streamlines were restricted only in WM as expected.

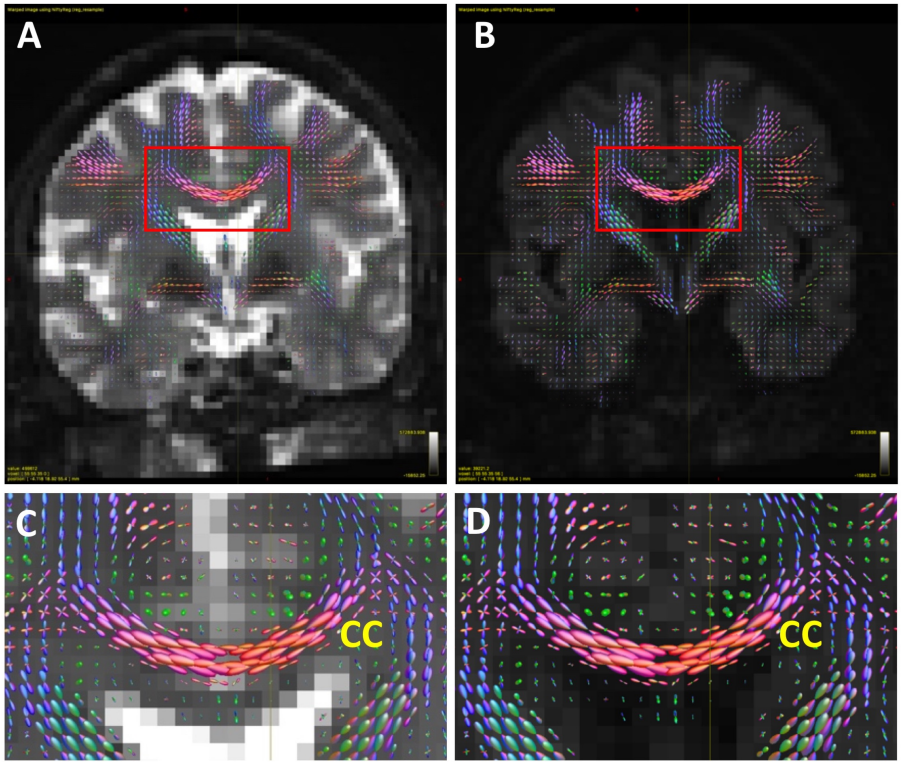

Figure 5.7. Example of the effect of misalignment between diffusion image with and without weighting

Fibre Orientation Distribution (FODs) is overlaid on **(A)** diffusion image without weighting (B0) and **(B)** diffusion weighted images (DWI). Due to the misalignment, the estimated FODs in **(A, C)** do not reflect the "true" underlying biological structure such as the corpus callosum as compared to **(B, D).** The red boxes in **(A)** and **(B)** represent the magnified images in **(C)** and **(D)** respectively. **CC**; corpus callosum.

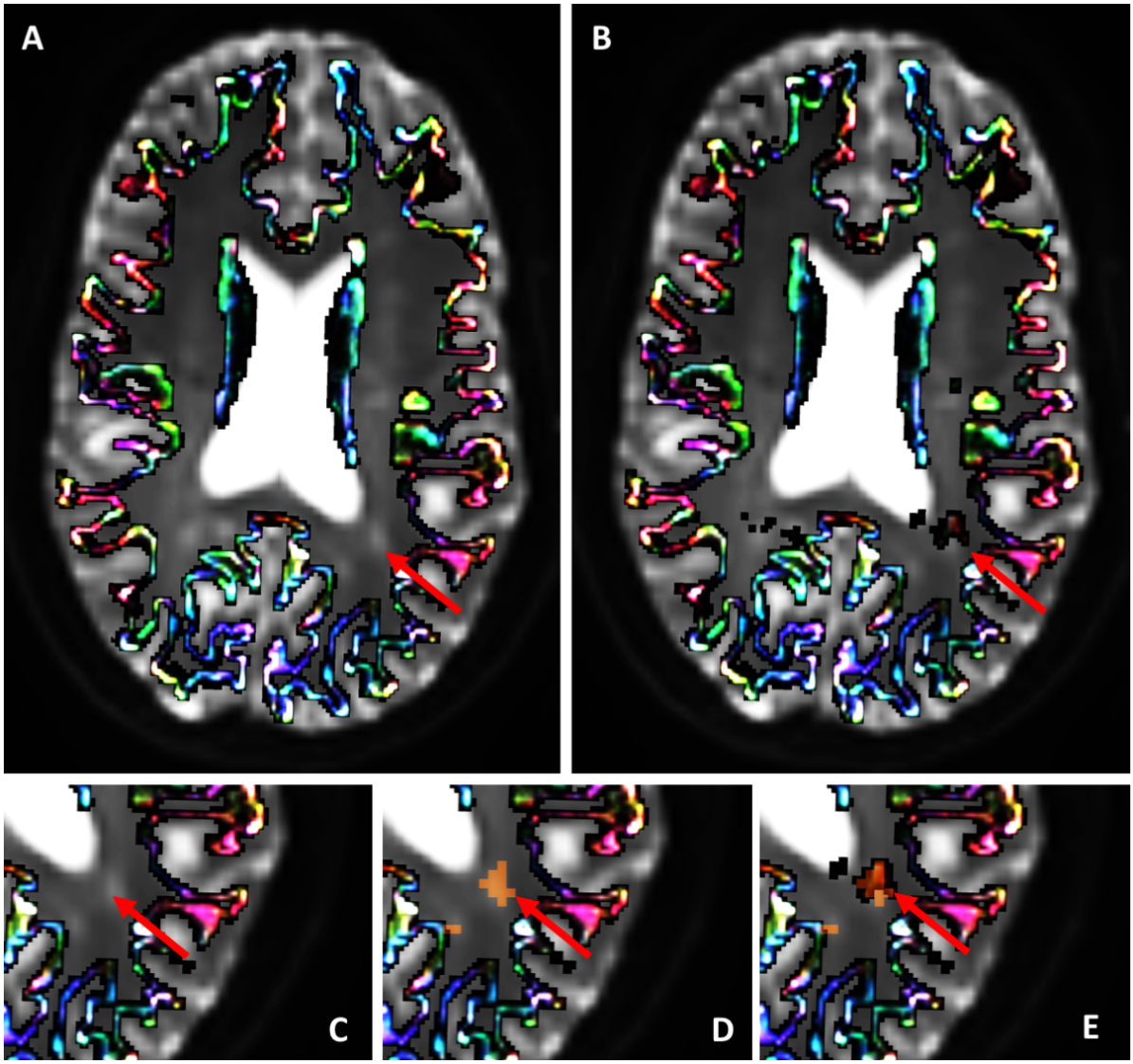

Figure 5.8. Effect of lesions on tractography

Color-coded line at the GM-WM interface overlaid on diffusion weighted image without directional weighting (B0) corresponds to the streamline termination points in **(A), (B), (C), (D)** and **(E)**. In **(B)** there are streamlines terminated in a lesion compared to **(A)** as shown by the red arrow. The red arrow points to a lesion **(C)**, to a lesion overlaid with lesion mask (orange; **D**) and to lesion overlaid with lesion mask and streamline termination points **(E).** In our study, we made sure that no streamlines are terminated in lesions. The effect of streamline termination and network measures is beyond the scope of this chapter.

Quality assessment of the connectome

The **Fig. 5.9**. shows the brain modelled as a graph and the connectivity matrix, also known as adjacency matrix, corresponding to only one individual. The two-dimensional connectivity matrix shows the pairwise connectivity between the 120 nodes of the network. Each column and its corresponding row corresponds to a unique node. In this study, we used the SIFT2 algorithm (Smith et al., 2015b) which reweights the contribution of streamline to the relevant edge. This means that the values in the matrix correspond to the pairwise sum of the cross-sectional area of the streamlines. Additionally, the matrix has zero values in the main diagonal (zero-diagonal) which means that we did not consider self-connections.

For the network validation we classified 12 control participants into 2 subgroups based on the age and gender and estimated the edge density. Controls1: 6 participants, 3 females, age (mean ± standard deviation (SD)) 36.5±11.7 years and controls2: 6 participants, 3 females (mean ± SD) 34.7 ± 14.5 years. There were no significant differences in the age and gender between the two groups ($p = 0.81$). When edge density as a network metric was compared between the two groups we found no significant difference ($p = 0.40$)

We also ranked brain regions based on the strength (K^W) metric and defined as hubs the nodes that had high K^w (≥ mean + one SD) **(Table 5.2)**. We identified the following hubs: the left and right precentral gyrus, left and right postcentral gyrus, left and right superior frontal gyrus, left and right middle frontal gyrus, and the subcortical brain structures, left and right thalamus proper and left and right putamen. These network hubs agree with previous work (Yeh et al., 2016)

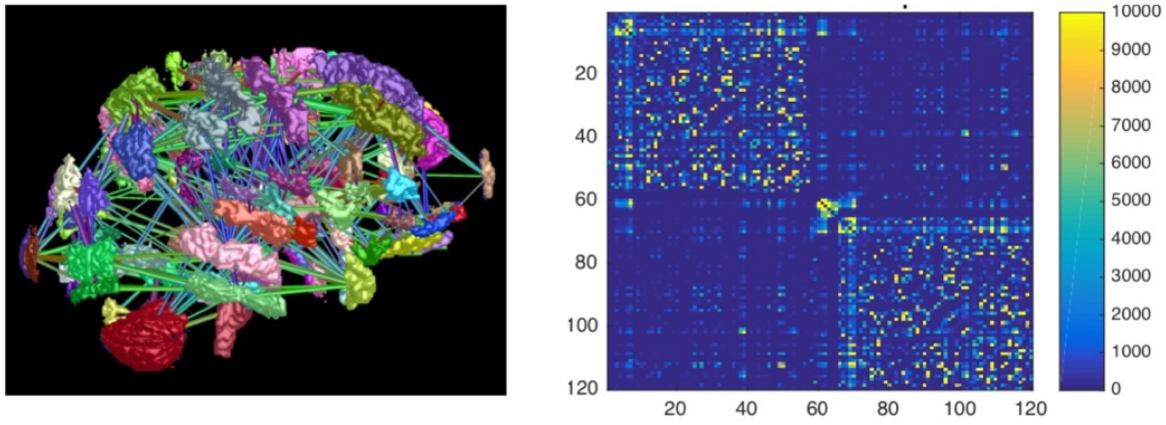

Figure 5.9. Example of a brain graph and connectivity matrix

On the **left**, the brain is modelled as a graph and on the **right** two-dimensional connectivity (adjacency) matrix is shown. In this zero-diagonal matrix, each row and column correspond to a different node (120 in total) and the element inside the matrix encodes information about the sum of the cross-sectional area of each streamline (Smith et al., 2015b). The matrix is organized in a way that the top left half quadrant corresponds to the left hemisphere and the bottom half right to the right hemisphere and they both contain intra-hemispheric connections.

BRAIN REGION	K^W ($X10^5$)
RIGHT PRECENTRAL GYRUS	3.48 (0.22)
LEFT PRECENTRAL GYRUS	3.62 (0.23)
RIGHT SUPERIOR FRONTAL GYRUS	3.44 (0.18)
LEFT SUPERIOR FRONTAL GYRUS	3.35 (0.17)
RIGHT MIDDLE FRONTAL GYRUS	2.90 (0.19)
LEFT MIDDLE FRONTAL GYRUS	3.07 (0.18)
RIGHT THALAMUS	2.69 (0.16)
LEFT THALAMUS	2.50 (0.15)
RIGHT POSTCENTRAL GYRUS	2.26 (0.11)
LEFT POSTCENTRAL GYRUS	2.31 (0.13)
RIGHT SUPERIOR PARIETAL LOBULE	2.29 (0.09)
LEFT SUPERIOR PARIETAL LOBULE	2.04 (0.11)
RIGHT PUTAMEN	2.34 (0.12)
LEFT PUTAMEN	2.20 (0.09)
RIGHT PRECUNEUS	2.21 (0.10)
LEFT PRECUNEUS	2.03 (0.10)
RIGHT MIDDLE TEMPORAL GYRUS	2.06 (0.10)
LEFT MIDDLE TEMPORAL GYRUS	1.89 (0.09)

Table 5.2. Structural network hubs

Network hubs defined based on the nodal strength (K^w; ≥ mean + one standard deviation (SD)). The defined regions are in accordance with the hubs published in the literature (Yeh et al., 2016).

5.4. Discussion

Recent advancements in neuroimaging, especially in diffusion MRI, provide powerful tools for the analysis of the brain as a complex network. However, creating a connectome is challenging in the sense that it is a multistep process and each step is a potential source of variance that can seriously bias the analysis, and advanced methods should be used that address some of the tracking biases. Therefore, careful quality assessment of each step is essential to ensure that the derived network reflects the underlying anatomical characteristics. The main steps and the usage of the advanced methods were shown in the results section above.

Beyond the quality assessment of the chosen algorithms, one must always consider the feasibility of connectome quantification. Weighting the connectomes with diffusion metrics such as FA or with number of streamlines suffers from intrinsic limitations as discussed in Jones et al. (2013) and in Sotiropoulos and Zalesky (2017). Therefore, several connectome studies represent the brain as a binary network meaning that existing connections irrespective of weight get the value “1” whereas no connections get the value “0”. To eliminate any spurious connections – usually represented with very low weight in the matrix – several arbitrary thresholding steps are performed. However, trace studies in macaques showed that the brain is a heterogeneous and complex network (Markov et al., 2011) and thus this binary formation fails to capture brain’s true complexity. Therefore, a weighted connectome could potentially be more relevant for connectivity analysis, if the reconstructed tractogram can reflect the underlying biological connectivity. In this study, the state-of-art CSD approach (Tournier et al., 2004; Tournier et al., 2007), the ACT framework (Smith et al., 2012) and SIFT2 technique (Smith et al., 2015b) were employed: CSD models intra-voxel crossing fibres, ACT improves the connection accuracy by

providing anatomical priors and SIFT2 improves the streamline density under the assumption that the FOD amplitude corresponds to the underlying fibre density (Raffelt et al., 2012). Recently, it has been demonstrated that streamline density derived after the application of SIFT method correlates better with WM connection estimates as derived from post-mortem tissues (Smith et al., 2015a). Hence, we believe that the use of these advanced methods should render the reconstructed network more biologically plausible, since they capture the continuous biological fibre connection density. Therefore, any detected changes are most likely to be relevant to pathology.

There is an additional point in favour of using of weighted connectivity matrix. The use of SIFT2 which reweights the streamlines so that false positives receive relatively weak weight (Smith et al., 2015b; Yeh et al., 2016). Hence keeping these low weights is unlikely to have a detrimental impact on the connectomic metrics and at the same time there is no need to arbitrarily threshold the matrix which might unfavourably alter the connectivity.

The proposed method is highly reproducible. For example, we showed that the estimated edge density is highly stable across age and gender matched subjects. Moreover, the network hubs, brain areas with high strength, identified in this study are in accordance with the previously reported study (Yeh et al., 2016) despite the fact that the parcellation scheme used is different (https://surfer.nmr.mgh.harvard.edu vs http://cmictig.cs.ucl.ac.uk/niftyweb/program.php?p=GIF) i.e. FreeSurfer vs GIF. This suggests that the hubs are relatively stable features of the network. Ideally, the brain network reconstructions and lesion effects should be validated histologically but because of the absence of appropriate ground-truth biological information further validation of our network cannot be performed.

The limitations associated with mapping the human brain and as a result with network reconstruction have been discussed in **chapter 4**. In this chapter, we used the latest techniques developed that are shown to reduce some of the known biases during the reconstruction process. Here, we do not claim that our structural network is a true representation of the actual human brain. We argue though that application of these state-of-art techniques improves significantly the reconstructed network such that it reflects better the underlying biology. To our knowledge this tis the first time that these techniques have been used in MS.

5.5. Conclusions

In conclusion, structural brain network reconstruction is a multistep process and each step is a potential source of bias. Here, we used state-of-the-art techniques, we quality assessed the output of each processing step and we validated the generated connectome with previously reported ones. The use of techniques such as ACT and SIFT2 are able to address a range of tractogram biases resulting in the reconstruction of a biologically plausible network. This pipeline will be used in **chapter 6** to investigate whether network metrics could explain disability in MS better than non-network metrics.

Bibliography

Andersson JL and Sotiropoulos SN. (2016) An integrated approach to correction for off-resonance effects and subject movement in diffusion MR imaging. *Neuroimage* 125: 1063-1078.

Bhushan C, Haldar JP, Joshi AA, et al. (2012) Correcting Susceptibility-Induced Distortion in Diffusion-Weighted MRI using Constrained Nonrigid Registration. *Signal Inf Process Assoc Annu Summit Conf APSIPA Asia Pac* 2012.

Cardoso MJ, Modat M, Wolz R, et al. (2015) Geodesic Information Flows: Spatially-Variant Graphs and Their Application to Segmentation and Fusion. *IEEE Trans Med Imaging* 34: 1976-1988.

Chard DT, Jackson JS, Miller DH, et al. (2010) Reducing the impact of white matter lesions on automated measures of brain gray and white matter volumes. *J Magn Reson Imaging* 32: 223-228.

Clayden J, Maniega SM, Stokey AJ, et al. (2011) TractoR: Magnetic Resonance Imaging and Tractography with R. *JSS*.

Eshaghi A, Prados F, Brownlee W, et al. (2018) Deep grey matter volume loss drives disability worsening in multiple sclerosis. *Ann Neurol*.

Griffa A, Baumann PS, Thiran JP, et al. (2013) Structural connectomics in brain diseases. *Neuroimage* 80: 515-526.

Hickman SI, Barker GJ, Molyneux PD, et al. (2002) Technical note: the comparison of hypointense lesions from 'pseudo-T1' and T1-weighted images in secondary progressive multiple sclerosis. *Mult Scler* 8: 433-435.

Jeurissen B, Leemans A, Tournier JD, et al. (2013) Investigating the prevalence of complex fiber configurations in white matter tissue with diffusion magnetic resonance imaging. *Hum Brain Mapp* 34: 2747-2766.

Jones DK, Knosche TR and Turner R. (2013) White matter integrity, fiber count, and other fallacies: the do's and don'ts of diffusion MRI. *Neuroimage* 73: 239-254.

Markov NT, Misery P, Falchier A, et al. (2011) Weight consistency specifies regularities of macaque cortical networks. *Cereb Cortex* 21: 1254-1272.

Prados F, Cardoso MJ, Burgos N, et al. (2016a) NiftyWeb: web based platform for image processing on the cloud. *24th Scientific Meeting and Exhibition of the International Society for Magnetic Resonance in Medicine (ISMRM).* ISMRM.

Prados F, Cardoso MJ, Kanber B, et al. (2016b) A multi-time-point modality-agnostic patch-based method for lesion filling in multiple sclerosis. *Neuroimage* 139: 376-384.

Premi E, Grassi M, van Swieten J, et al. (2017) Cognitive reserve and TMEM106B genotype modulate brain damage in presymptomatic frontotemporal dementia: a GENFI study. *Brain* 140: 1784-1791.

Raffelt D, Tournier JD, Rose S, et al. (2012) Apparent Fibre Density: a novel measure for the analysis of diffusion-weighted magnetic resonance images. *Neuroimage* 59: 3976-3994.

Shu N, Liu Y, Li K, et al. (2011) Diffusion tensor tractography reveals disrupted topological efficiency in white matter structural networks in multiple sclerosis. *Cereb Cortex* 21: 2565-2577.

Smith RE, Tournier JD, Calamante F, et al. (2012) Anatomically-constrained tractography: improved diffusion MRI streamlines tractography through effective use of anatomical information. *Neuroimage* 62: 1924-1938.

Smith RE, Tournier JD, Calamante F, et al. (2015a) The effects of SIFT on the reproducibility and biological accuracy of the structural connectome. *Neuroimage* 104: 253-265.
Smith RE, Tournier JD, Calamante F, et al. (2015b) SIFT2: Enabling dense quantitative assessment of brain white matter connectivity using streamlines tractography. *Neuroimage* 119: 338-351.
Sotiropoulos SN and Zalesky A. (2017) Building connectomes using diffusion MRI: why, how and but. *NMR Biomed*.
Sporns O, Tononi G and Kotter R. (2005) The human connectome: A structural description of the human brain. *PLoS Comput Biol* 1: e42.
Tax CM, Jeurissen B, Vos SB, et al. (2014) Recursive calibration of the fiber response function for spherical deconvolution of diffusion MRI data. *Neuroimage* 86: 67-80.
Taylor NP, Sinha N, Wang Y, et al. (2017) The impact of epilepsy surgery on the structural connectome and its relation to outcome. *Neurons and Cognition*.
Tournier JD, Calamante F and Connelly A. (2007) Robust determination of the fibre orientation distribution in diffusion MRI: non-negativity constrained super-resolved spherical deconvolution. *Neuroimage* 35: 1459-1472.
Tournier JD, Calamante F and Connelly A. (2010) Improved probabilistic streamlines tractography by 2nd order integration over fibre orientation distributions. *Joint Annual Meeting ISMRM-ESMRMB*.
Tournier JD, Calamante F, Gadian DG, et al. (2004) Direct estimation of the fiber orientation density function from diffusion-weighted MRI data using spherical deconvolution. *Neuroimage* 23: 1176-1185.
Tustison NJ, Avants BB, Cook PA, et al. (2010) N4ITK: improved N3 bias correction. *IEEE Trans Med Imaging* 29: 1310-1320.
van den Heuvel MP and Sporns O. (2013) Network hubs in the human brain. *Trends Cogn Sci* 17: 683-696.
Yeh CH, Smith RE, Liang X, et al. (2016) Correction for diffusion MRI fibre tracking biases: The consequences for structural connectomic metrics. *Neuroimage* 142: 150-162.

Chapter 6

6. Structural network disruption markers explain disability above non-network metrics in multiple sclerosis

Summary

In this chapter, we evaluated whether brain network metrics can improve the prediction of clinical and cognitive dysfunction in multiple sclerosis beyond brain atrophy measures and white matter lesions. We applied the pipeline developed in **chapter 5** in 51 healthy controls and 122 MS patients consisting of 58 relapsing-remitting, 28 primary progressive and 36 secondary progressive. Structural brain networks were reconstructed from diffusion-weighted magnetic resonance images. Standard metrics reflecting network density, efficiency and clustering coefficient were derived and compared between subjects' groups. Stepwise linear regression analyses were used to investigate the contribution of network measures that explain clinical disability (Expanded Disability Status Scale) and information processing speed (Symbol Digit Modalities Test) compared with conventional imaging metrics alone and to determine the best statistical model that explains better Expanded Disability Status Scale and Symbol Digit Modalities Test. This chapter shows compared to controls, network efficiency and clustering coefficient were reduced in multiple sclerosis whilst these measures are also reduced in secondary progressive relative to relapsing-remitting patients. Structural network metrics increase the variance explained by the statistical models for clinical and information processing dysfunction. The best model for Expanded Disability Status Scale score showed that reduced network density and global efficiency and increased age were associated with increased clinical disability.

The best model for Symbol Digit Modalities Test score showed that lower deep grey matter volume, reduced global efficiency and male gender were associated with worse cognitive performance. This chapter concludes that network metrics were able to explain disability better than conventional imaging measures suggesting that network metrics can provide additional clinically relevant information about multiple sclerosis pathology.

Scientific contribution

The results presented in this chapter are currently under review (revised version) in *Journal of Neurology, Neurosurgery and Psychiatry*: **"Structural network disruption markers explain disability in multiple sclerosis".**

6.1. Introduction

As discussed in **chapter 4,** diffusion-derived networks in MS have shown reduced network efficiency correlating with physical disability (Shu et al., 2011) or cognitive performance (Llufriu et al., 2017). A very common cognitive domain affected is information processing speed and is assessed by Symbol Digit Modalities Test (SDMT) (Rocca et al., 2015). Neurologic impairment with particular emphasis on ambulation status is evaluated by another widely used measure, Expanded Disability Status Scale (EDSS) (Kurtzke, 1983).

Whether network metrics improve the correlation with disability beyond routine imaging metrics is unknown. In addition, previous investigations included only RRMS or SPMS and did not examine all MS subtypes. In this study, using the pipeline that we developed in **chapter 5**, we aimed:

1. to study the structural network differences between subjects' groups in a cohort that includes the main MS subtypes (RRMS, PPMS, SPMS)
2. to investigate whether network measures can explain disability over and above conventional imaging metrics
3. to determine the best statistical model for predicting change in EDSS and SDMT.

6.2. Methods

This section will summarise the pipeline that we introduced in **chapter 5**

6.2.1. Participants

We recruited 122 MS patients (58 RRMS, 28 PPMS and 36 SPMS) who had not experienced relapses within the preceding 4 weeks and classified as per Lublin and Reingold criteria (Lublin and Reingold, 1996). Fifty-one HC were also examined. Participants underwent MRI and neurological assessment using EDSS (Kurtzke, 1983). A verbal SDMT test was performed in a subset of MS participants (n=60) (**eTable 6.1 supplemental**) to screen for information processing speed. Fatigue (visual analogue scale), depression and anxiety (Hospital Anxiety and Depression Scale [HADS]) were also assessed in some patients (**eTable 6.2 supplemental**). This work has been approved by the local institutional ethics committee and written consent was obtained from all the patients.

6.2.2. MRI data acquisition

MRI data acquisition parameters were introduced in **section 5.2.2.** Briefly, MRI data were acquired on a Philips Achieva 3T MR scanner (Philips Healthcare, Best, Netherlands) with a 32-channel head coil using: (1) 3D sagittal T1-weighted scans with a fast-field echo scan, (2) whole brain High Angular Resolution Diffusion Imaging (HARDI) scan with echo planar imaging consisted of a cardiac-gated spin-echo (SE) sequence and (3) dual-echo proton density/T2-weighted axial oblique-scans.

6.2.3. Structural network reconstruction pipeline

For network reconstruction, we used the optimised pipeline discussed in **chapter 5** and illustrated in **Fig. 6.1**. The main steps are summarised below:

Structural images processing

Briefly, an affine transformation was performed to register the subject's non-filled T1-weighted bias-field corrected image to the corresponding DWI using BrainSuite v.15b (Bhushan et al., 2012). The target volume was the first b0 image after DWI pre-processing, resulting in a structural image of resolution 2x2x2 mm^3. T2-hyperintense lesions were affine transformed to DWI space and then filled the T1-weighted images using a modality-agnostic patch-based method (Prados et al., 2016b). The filled T1-weighted images were then segmented into different tissue types and parcellated according to Desikan–Killiany–Tourville atlas protocol using GIF (Cardoso et al., 2015). We then estimated the volumes of the various tissue types (NABV (normal appearing brain volume (BV)), GM, CGM, DGM and reduction of these volumes reflect atrophy measures. We also estimated LL (lesion load) as a measure of WM focal damage.

Diffusion-weighted imaging processing and tractography

The mean b0 image was rigid registered to the first b0 image. Then, the same rigid transformation was applied to the 61 DWI volumes. FSL v5.0.9 was used on the DWI data to correct for eddy current and head motion (Andersson and Sotiropoulos, 2016) and BrainSuite v.15b to correct for EPI distortions (Bhushan et al., 2012). For the whole brain probabilistic tractography, we used MRtrix3 v0.3.14 to generate 10^7 streamlines implementing the ACT framework (Smith et al., 2012) followed by SIFT2 algorithm (Smith et al., 2015b).

Network reconstruction and metrics

GM parcellations constituted the network nodes, 120 in total and each network edge was defined as the sum of weights of streamlines connecting a pair of nodes (Smith

et al., 2015b). We extracted a range of standard network measures using TractoR (Clayden et al., 2011). We focused on the following network topological measures: Edge density, also known as connectivity, is the ratio of the connections exist relative to the number of potential connections. Global efficiency is a network integration metric that describes the information flow over the entire network while local efficiency is considered a local homolog of global efficiency quantifying information transfer within local networks. Finally, clustering coefficient reflects the number of connections between neighbouring nodes and is related to network segregation (Rubinov and Sporns, 2010). We used the weighted forms of the graph-derived metrics, except edge density, which is derived from a binary network.

6.2.4. Statistical analysis

Statistical analysis was performed using R software (https://www.r-project.org/ v3.3.0). For all the models, we explored whether there was a violation of normality assumption of the residuals. Data are reported as mean ± standard deviation (SD), unless otherwise stated. P-values<0.05 were considered statistically significant.

Preliminary analysis

To assess network differences between subjects' groups ANOVA analysis was used adjusting for age, gender, LL and total intracranial volume (TIV) to correct for head size. To explore possible associations of all the variables in MS patients, we used bivariate Pearson's correlations. The variables include network metrics (edge density, global efficiency, mean local efficiency and mean clustering coefficient), atrophy measures (volumes of NABV, GM, CGM, DGM), WM damage metrics (LL), clinical scores (EDSS and SDMT) and patient age and gender (**Fig. 6.2**). In this study, atrophy measures and WM lesions are also referred to as MRI metrics. Volumetric differences

between HC and MS patients were also assessed (**eTable 6.3 supplemental results**).

Network measures and volumetric parameters in explaining EDSS and SDMT

We performed stepwise linear regression analyses using each of the volume metrics (in turn) as independent variables and age, gender and LL as covariates to explain clinical scores (dependent variable). We also controlled for the presence of disease modifying treatments (DMTs). We selected the best model as assessed with the adjusted R^2 and then added each network metric, in turn, as an independent variable. For SDMT, we performed a post-hoc analysis controlling for education level as a categorical and afterwards as continuous variable to investigate possible linear relationship between education level and SDMT. To assess whether the effect for each network metric in explaining disability is group-dependent, we stratified the MS population based on their clinical profile by creating an interaction term e.g. the product between the network metric and a categorical variable for MS subgroup (RRMS, PPMS, SPMS), 'network metrics x MS subgroup', that was then included in the model as an explanatory variable. For SDMT we explored possible associations between network metrics and MRI variables in HC.

Final models to explain EDSS and SDMT

To find the best model that explains disability, a stepwise forward selection linear regression strategy was employed. All variables of interest were sequentially added to the model and kept only if significant, culminating in two final models, one per each clinical score.

6.3. Results

Demographic, clinical, MRI and network data from MS patients and HC are summarised in **Table 6.1**.

Differences in network metrics in MS population and subtypes

There was a significant decrease in global efficiency (regression coefficient (RC) = -71.23, p = 0.016), mean local efficiency (RC = -72.53, p = 0.31) and mean clustering coefficient (RC = -14.84, p < 0.0001) in the whole MS group when compared with HC. For the subtypes, there was reduced global efficiency in PPMS (RC = -85.82, p = 0.027) and in SPMS (RC = -145.34, p = 0.0002) relative to HC and also decrease in this metric in SPMS relative to RRMS (RC = -111.90, p = 0.0008). Mean local efficiency was reduced in SPMS compared to HC (RC = -158.42, p = 0.0002) and to RRMS (RC = -128.21, p = 0.0007). Relative to HC, mean clustering coefficient was reduced in RRMS (RC = -14.84, p < 0.0001), PPMS (RC = -13.42, p < 0.0001) and SPMS (RC = -20.30, p < 0.0001) while relative to RRMS it was reduced in SPMS (RC = -8.30, p = 0.0033). There was also a significant decrease in SPMS compared to PPMS (RC = -6.88, p = 0.037). All models were adjusted for age, gender, LL and TIV **(Table 6.2; Fig. 6.2)**.

Descriptive associations among study variables in patients

Pairwise associations among clinical, volume and network metrics, LL and age study variables are shown in **Fig. 6.3**. Higher LL was associated with lower connectivity (r = -0.3), lower values of global (r = -0.3) or local (r = -0.2) efficiency and reduced clustering (r = -0.6). Also, lower connectivity and lower clustering coefficient were associated with reduced volumes of NABV, GM, CGM, DGM and NAWM (r = between 0.2 and 0.5). Moreover, we found associations between clinical scores and network

measures, e.g. higher EDSS and lower SDMT scores were associated with lower connectivity values, global and local efficiency and clustering coefficient (r = between 0.2 and 0.5). Additionally, correlation analyses between clinical scores and volume metrics demonstrated that higher EDSS scores and lower SDMT were associated with reduced volumes of NABV, GM, CGM, DGM and NAWM (r = between 0.2 and 0.5). Higher LL was also associated with decreased SDMT (r = -0.5) but showed very little correlation with EDSS score (r = -0.1). We also found that higher EDSS score is associated with lower SDMT score (r = 0.5). Gender showed weak associations with network metrics (r= between -0.1 and 0.2). For age, we found that older participants show lower values of network metrics (r = between -01 and 0.2) except edge density that shows weak linear relationship (r < 0.05).

Statistical modelling of EDSS score

We found that NABV was the only significant predictor of EDSS after adjusting for age, gender and LL. For each mL decrease in NABV there was an increase in the EDSS score of $4.06x10^{-3}$ (95% confidence interval (95%CI): $-7.68x10^{-3}$ to $-4.3x10^{-3}$) p = 0.029, adjusted R^2 = 0.185; **Table 6.3)**. We did not find any significant adjusted associations between the other volume metrics and EDSS.

When network metrics were added to the model reported above as predictors, in turn, we found that they were each associated with EDSS independently of NABV. Specifically, we found that for each percentage point decrease in edge density there was an increase in the EDSS score of 0.13 (95% CI: -0.27 to $-1.49x10^{-3}$, p = 0.047, adjusted R^2 = 0.205) and for each unit decease in global efficiency there was an increase in the EDSS score of $2.67x10^{-3}$ (95% CI: $-4.75x10^{-3}$ to $-5.81x10^{-4}$, p = 0.013, adjusted R^2 = 0.221). In addition, we found that for each unit decease in mean local efficiency there was an increase in the EDSS score of $1.90x10^{-3}$ (95% CI: $-3.76x10^{-3}$

to -4.40x10^{-5}, p = 0.045, adjusted R^2 = 0.206) and finally for each unit decease in mean clustering coefficient there was an increase in the EDSS score of 3.98x10^{-2} (95% CI: -6.34x10^{-2} to -1.61x10^{-2}, p = 0.011, adjusted R^2=0.235) (**Table 6.3**). We did not find any significant difference in the effect of any of the network measures in any of the MS subgroups examined. All the above models were adjusted for age, gender, LL and DMTs.

The best model to explain EDSS using the stepwise forward selection linear regression analysis showed that lower edge density, lower global efficiency and increased age of the participants were significantly associated with EDSS (**Table 6.3**). This model explained 26% of the variance in EDSS compared with 18.5% for the NABV alone or with 20% for global efficiency (-0.02, 95% CI: -0.0049 to -0.00063, p = 0.012) or with 20% for edge density (-0.16, 95% CI: -0.28 to -0.035, p = 0.012), after adjusting for age, gender and LL.

Statistical modelling of SDMT score

We repeated the multiple linear regression analyses to predict SDMT score. When only volume metrics were included, the best model fit was achieved by DGM as predictor, showing that for each 1 cm^3 decrease in the volume of DGM there was a decrease in the SDMT score of 1.61 (95% CI: 0.79 to 2.43, p < 0.001, adjusted R^2 = 0.361; **Table 6.4**), i.e. smaller DGM volumes were associated with worse information processing speed in the whole MS group.

When we added network metrics, in turn, in our multiple regression analysis that included DGM as one of the predictors, we found that global efficiency, mean local efficiency and mean clustering coefficient were able to significantly explain additional variance in SDMT. For each unit increase in global efficiency there was an increase

in the SDMT score of 0.02 (95% CI: 0.01 to 0.04, p = 0.008, adjusted R^2=0.396). For each unit increase in mean local efficiency there was an increase in the SDMT score of 0.02 (95% CI: 0.002 to 0.03, p = 0.018, adjusted R^2 = 0.380) and finally for each unit increase in mean clustering coefficient there was an increase in the SDMT score of 0.21 (95% CI: 0.05 to 0.38, p = 0.013, adjusted R^2 = 0.387). There was no evidence of change of SDMT score per percentage increase in edge density (0.44, 95% CI: -0.56 to 1.44, p = 0.38, adjusted R^2 = 0.374; **Table 6.4**). Additionally, there was no significant difference in the effect of any of the network metrics in any of the subgroups examined.

The best model to explain SDMT using the stepwise forward selection linear regression analysis showed that greater DGM volume, greater global efficiency and female gender were all associated with better information processing speed (**Table 6.4)**. This model explained 39.6% of the variance in SDMT scores compared with 36% for the DGM alone (1.61, 95 % CI: 0.79 to 2.43, p < 0.001).

6.5. Discussion

This study detected differential topological organisation of WM networks in MS patients and subtypes. We also demonstrated that markers of network disruption explain EDSS and SDMT performance over and above metrics of tissue atrophy and WM lesions.

Structural network differences between subjects' groups

We detected network topological changes in MS. Relative to HC, SPMS had reduced global and local efficiency, PPMS reduced global efficiency while there was no efficiency change in RRMS. These changes reflect network alterations due to diffuse WM pathology including impaired long and short distance connections characteristics that are more prominent in the progressive types. Previous studies focused mainly on RRMS reporting decreases in this metric in structural (Kocevar et al., 2016; Shu et al., 2016; Shu et al., 2011) and functional (Rocca et al., 2016; Shu et al., 2016; Liu et al., 2017) networks whilst others, in accordance with this work, found no differences (Llufriu et al., 2017). Intriguingly, increased efficiency in RRMS in the first year from onset in the absence of clinical impairment is suggestive of structural adaptations to maintain normal function (Fleischer et al., 2017). Our RRMS cohort has a relatively long disease duration with high EDSS with accrual of baseline disability as a result of incomplete recovery from relapses explaining partly the absence of this effect. To date, only one study considered SPMS and PPMS groups reporting reduced global efficiency, in accordance with our findings (Kocevar et al., 2016). Moreover, we demonstrate reduced global and local efficiency in SPMS relative to RRMS, a result likely to reflect the neurodegenerative component in this progressive subtype.

Clustering coefficient is a “small-world” metric and reduction suggests a more random architecture (Bullmore and Sporns, 2012) related to increased disability as shown in our study and elsewhere (Douw et al., 2011). Previous structural studies reported increased clustering coefficient in RRMS compared to HC (Muthuraman et al., 2016; Fleischer et al., 2017; Tewarie et al., 2014) and is thought to reflect transient compensatory changes. No change was reported in functional networks (Rocca et al., 2016; Schoonheim et al., 2012). Here, we report a decrease in clustering coefficient in RRMS compared to HC, in agreement with a study that investigated both structural and functional networks (Shu et al., 2016). We also extend these findings, demonstrating reduction of this metric in the progressive phases. Clustering coefficient was further reduced in SPMS relative to RRMS and PPMS indicating that impaired local information flow is linked to the disease severity. Nonetheless, further investigations with bigger sample sizes and longitudinal study design should confirm the study findings.

Network measures explain additional variance of disability

Whole brain atrophy is a relatively strong predictor of EDSS. Our study shows that the addition of network metrics into the model, singly and together, explains more EDSS variance, leading to our final model (**Table 6.3**), according to which edge density and global efficiency explain 26% of the variance, that is 7% more compared to NABV alone (18.5%). Loss of connectivity could reflect neurodegeneration due to continuous inflammation (Friese et al., 2014) while reduced global efficiency could indicate impaired structural long-range connections probably due to inflammatory activity and neuroaxonal loss (Mangeat et al., 2018). The fact that these measures integrate information beyond local tissue damage atrophy measures may account for the increased explained variance.

SDMT was most strongly associated with DGM atrophy and WM damage (Tewarie et al., 2015). Previous structural and functional studies demonstrated the relationship between network disruption and cognitive impairment (Tewarie et al., 2015; Schoonheim et al., 2015; Dineen et al., 2009). Our study findings showed that global efficiency is not only associated with SDMT as previously shown but it also explained additional variance **(Table 6.4)** highlighting that intact network integration is important for efficient information processing beyond participant's education level and treatment. These findings are also consistent across WM diseases (Tuladhar et al., 2016) signifying the relevance of network efficiency as potential marker of cognitive disability.

MS is a heterogeneous disease. This study included MS patients with the main disease phenotypes in order to provide a representative snapshot of structural networks throughout the entire disease course. Our regression analyses show that the behaviour of the network metrics was similar in all MS subtypes suggesting that these measures could be useful across the whole MS disease spectrum. The same statistical models did not explain SDMT in HC. This negative result is not surprising given the narrow distribution of the SDMT variable in HC compared to patients (see **Table 6.1** for mean and SD). Furthermore, due the small number of HC for which we have SDMT (n=12) these results should be interpreted with caution. Future studies could assess whether the findings presented here are replicated in other cohorts.

Descriptive associations among study variables in patients

Our univariate associations in patients revealed some interesting patterns. Low values of network metrics were associated with clinical impairment and worse information processing speed in accordance with previous studies (Shu et al., 2011; Llufriu et al., 2017; Shu et al., 2016). Interestingly, reduced clustering showed the strongest

association out of network metrics with worse SDMT indicating that network randomization impairs information processing speed as shown previously (Douw et al., 2011). Our multivariate analysis though, demonstrated that reduced network integration and tissue atrophy can more strongly affect SDMT performance. In line with previous work (Shu et al., 2011), WM lesions impair the communication between brain regions at the global and local level as demonstrated by the reduced network efficiencies. As shown in the exact same cohort, we did not find any association between WM lesions and EDSS (Pardini et al., 2015) and only weak association between WM lesions and SDMT and this highlights the need to explore non-conventional MRI metrics to explain disability. Also, there was no association between edge density and any of the network efficiencies. Although this could be the result of wiring cost and efficiency (Bullmore and Sporns, 2012), we argue that direct comparison between binary and weighted network is not valid.

In our approach we used CSD to model intra-voxel crossing fibres (Tournier et al., 2007), ACT and SIFT2 to improve connection accuracy and streamline density (Smith et al., 2015b; Smith et al., 2012) respectively with the assumption that the FOD amplitude corresponds to the underlying fibre density (Raffelt et al., 2012). These advanced methods improve tractogram reconstruction without the need of various scaling techniques (Yeh et al., 2016). We also provided anatomical prior of the WM ensuring that no streamlines are incorrectly terminated in the WM due to lesions as showed in **chapter 5** (**Fig. 5.8**). In fact, we identified an association between LL and connectivity, but this is a moderate correlation (r = -0.3) highlighting that our current approach is not overly influenced by lesions.

Limitations and future directions

This study has several limitations. In our approach, we applied techniques to address some of the reconstruction biases and to ensure that no streamlines were abnormally terminated in WM (Smith et al., 2012; Smith et al., 2015b; Yeh et al., 2016). However, histological validation studies are required to make direct links between imaging measures and underlying pathology. Additionally, the cross-sectional design of the study does not allow to determine the clinical relevance of network measures over time. Moreover, we used SDMT scores for approximately half of MS cohort (n=60 vs n=122) but this subcohort had similar proportions of MS subgroups to the whole cohort (**eTable 6.1 supplemental**). Also, the effects of fatigue, depression and anxiety can be investigated in future studies with larger cohorts. A post-hoc analysis revealed depression and anxiety scores showed mild correlations with SDMT whereas fatigue did not. It is difficult to investigate their influences in our cohort as the HADS and fatigue scores were not collected in all subjects with SDMT. Additionally, medication that are commonly used in MS including antidepressants, benzodiazepines and antimuscarinics for bladder dysfunction (Panicker et al., 2015) can all affect cognitive functions and processing speed influencing thus the study findings. Due to the retrospective nature of the study, medication use could not be quantified here but this should be tested in future studies. Finally, although the effect of cortical lesions in clinical scores is limited (van de Pavert et al., 2016), it is possible that they may influence our study outcomes.

The study findings could provide the basis for future work. There are different scales that we could study MS from, including micro, meso and macro scales (Cercignani and Gandini Wheeler-Kingshott, 2018). Network analysis offers a framework at the macroscale to study whole brain connectivity patterns beyond focal

pathology while TBSS, for example, is currently considered a leading technique for the voxel-wise DTI analysis (Dineen et al., 2009). Future investigations could focus in the comparison between scales and their link with clinical outcome. Additionally, further studies could follow a subnetwork or nodal rather than global network analysis and perhaps derive integrative measures of structural and functional networks and investigate if these parameters explain additional variance

6.6. Conclusion

In conclusion, we found distinct structural network organisation in the various groups. In addition, network metrics and in particular global efficiency explains disability over and above non-network metrics supporting the relevance of intact long-distance connections mainly, to maintain normal function. These results highlight the fact that network metrics can provide additional clinical information regarding MS pathology.

To gain further insights into network dynamics, longitudinal studies are required which can elucidate how network changes over time. Longitudinal structural network studies have not yet performed in MS, while from an image analysis perspective they require specific processing techniques which will be discussed in **chapter 7**.

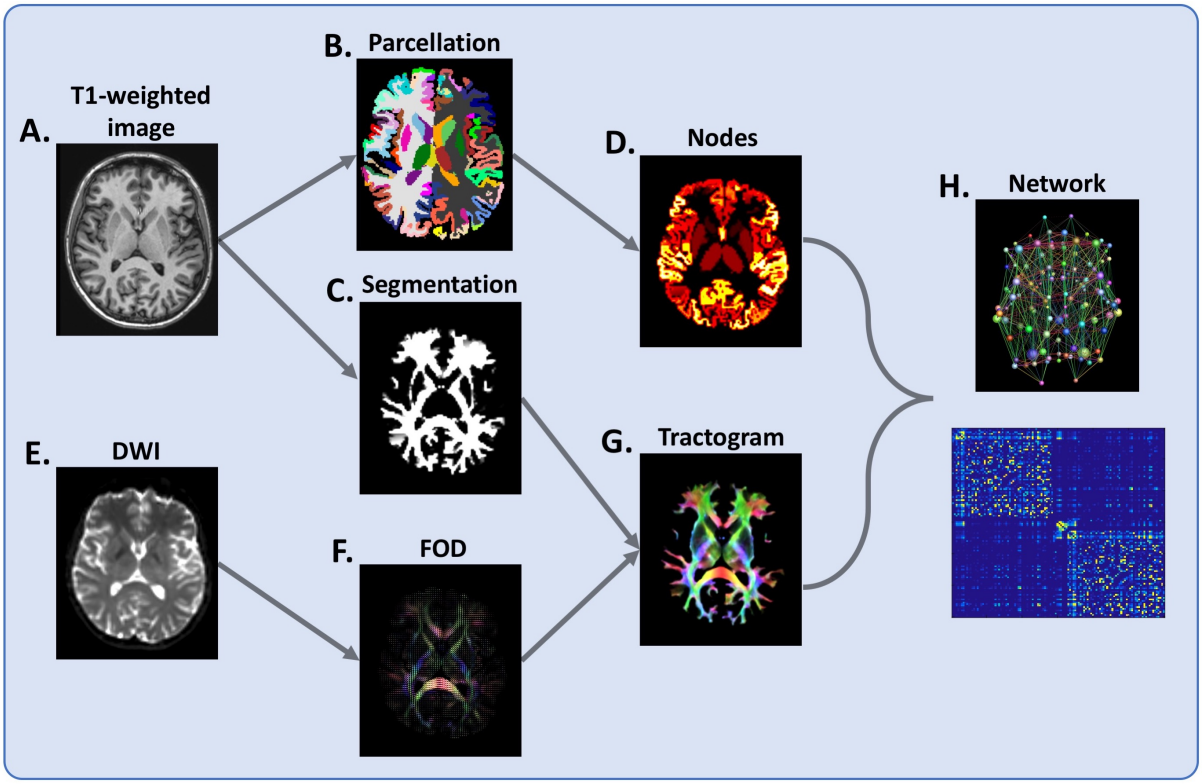

Figure 6.1. Flowchart of structural brain network reconstruction

For each subject, **(A)** T1-weighted image is segmented into grey matter **(B)** and white matter **(C)**. The grey matter segmentation is parcellated into cortical and deep grey matter regions **(B)** which serve as network nodes **(D)** in the subsequent network-based analysis. From a diffusion-weighted image (DWI) **(E)**, voxel-wise fibre orientation distribution (FOD) **(F)** is estimated and whole brain tractography undertaken **(G)**, with the white matter segmentation **(C)** used to prevent this from spilling into grey matter (see main text for details). Finally, nodes and tractogram are modelled into a network **(H)**. Connections are weighted by the sum of the pairwise streamline weights.

Table 6.1. Demographics, clinical, MRI and network metrics

	HC (n = 51)	MS patients (n = 122)	RRMS (n = 58)	PPMS (n = 28)	SPMS (n = 36)
			Demographics		
Age, years	41 ± 13	48 ± 11	42 ± 10	52 ± 9	53 ± 7
Gender (M/F)	25/26	36/86	18/40	10/18	8/28
Disease duration, years	-	15 ± 10	11 ± 8	14 ± 7	22 ± 10
% (no) patients of DMTs	-	58 (67)	84 (48)	13 (3)	47 (16)
% (no) patients who relapsed in the previous two years	-	51 (38)	68 (32)	0 (0)	24 (6)
			Clinical scores		
EDSS, median	-	5.5 (0-8.5)	2 (0-7)	6 (3-8)	6.5 (4-8.5)
SDMT	65.08 ± 8.31	45.50 ± 13.27	51.04 ± 14.28	42.86 ± 9.46	39.00 ± 10.88
			MRI metrics		
NABV (cm^3)	1158 ± 102	1042 ± 120	1070 ± 123	1060 ± 122	984 ± 93
GM (cm^3)	679 ± 57	625 ± 65	641 ± 64	632 ± 67	593 ± 52
CGM (cm^3)	640 ± 54	591 ± 61	606 ± 61	597 ± 65	561 ± 50
DGM (cm^3)	39.00 ± 3.39	34.18 ± 4.02	34.86 ± 4.09	35.41 ± 3.50	32.12 ± 3.54
NAWM (cm^3)	480 ± 49	418 ± 59	429 ± 62	429 ± 60	391 ± 45
LL (mL)	-	14.37 ± 15.92	12.78 ± 15.72	16.56 ± 19.83	15.23 ± 12.73
			Network metrics		
Edge Density (%)	92.6 ± 2.7	90.6 ± 3.2	90.8 ± 3.3	90.5 ± 3.0	90.3 ± 3.0
Global efficiency	3881 ± 121	3783 ± 175	3827 ± 137	3763 ± 196	3729 ± 199
Mean local efficiency	3975 ± 139	3889 ± 200	3934 ± 160	3868 ± 220	3831 ± 229
Mean clustering coefficient	247 ± 9.2	223 ± 18.3	227 ± 17.2	224 ± 20.5	217 ± 16.8

Values listed are mean ± standard deviation (SD)

Abbreviations: HC = healthy controls; MS = multiple sclerosis; RRMS = relapsing-remitting MS; PPMS = primary progressive MS; SPMS = secondary progressive MS; EDSS = Expanded Disability Status Scale; SDMT = Symbol Digit Modalities Test; NABV = normal appearing brain volume; GM = grey matter; CGM = cortical grey matter; DGM = deep grey matter; NAWM = normal appearing white matter; LL = Lesion load

Table 6.2. Network differences between different groups

	HC			RRMS			PPMS		
	RC	**95% CI**	**p-value**	**RC**	**95% CI**	**p-value**	**RC**	**95% CI**	**p-value**
EDGE DENSITY									
MS	-0.65	-1.69 0.38	0.210						
RRMS	-0.71	-1.84 0.42	0.219						
PPMS	-0.72	-2.11 0.67	0.310	-0.011	-1.27 1.25	0.987			
SPMS	-0.45	-1.78 0.88	0.507	0.258	-0.93 1.43	0.670	0.27	-1.12 1.66	0.707
GLOBAL EFFICIENCY									
MS	-71.23	-129.47 -13.00	**0.016**						
RRMS	-33.44	-95.11 28.25	0.287						
PPMS	-85.82	-161.65 -9.96	**0.027**	-52.38	-121.08 16.34	0.135			
SPMS	-145.34	-218.38 -72.28	**0.0001**	-111.90	-176.47 -47.31	**0.0008**	-59.52	-135.72 16.67	0.126
MEAN LOCAL EFFICIENCY									
MS	-72.53	-138.60 -6.46	**0.031**						
RRMS	-30.21	-100.16 39.74	0.396						
PPMS	-85.68	-171.68 0.34	0.051	-55.46	-133.39 22.47	0.162			
SPMS	-158.42	- 241.26 -75.58	**0.0002**	-128.21	-201.44 -54.96	**0.0007**	-72.74	-159.16 13.68	0.099
MEAN CLUSTERING COEFFICIENT									
MS	-14.84	-19.89 -9.79	**<0.0001**						
RRMS	-12.00	-17.51 -6.48	**<0.0001**						
PPMS	-13.42	-20.19 -6.64	**0.0001**	-1.42	-7.55 4.73	0.650			
SPMS	-20.30	-26.84 -13.76	**<0.0001**	-8.30	-14.07 -2.52	**0.0033**	-6.88	-13.69 -0.06	**0.037**

Abbreviations: HC = healthy controls; MS = multiple sclerosis; RRMS = relapsing-remitting MS; PPMS = primary progressive MS; SPMS = secondary progressive MS; RC = regression coefficient; CI = confidence intervals

P-values in bold denote statistical significance at $P < 0.05$ when the groups on the left were compared to the groups on the top row and adjusted for age, gender, lesion load and total intracranial volume.

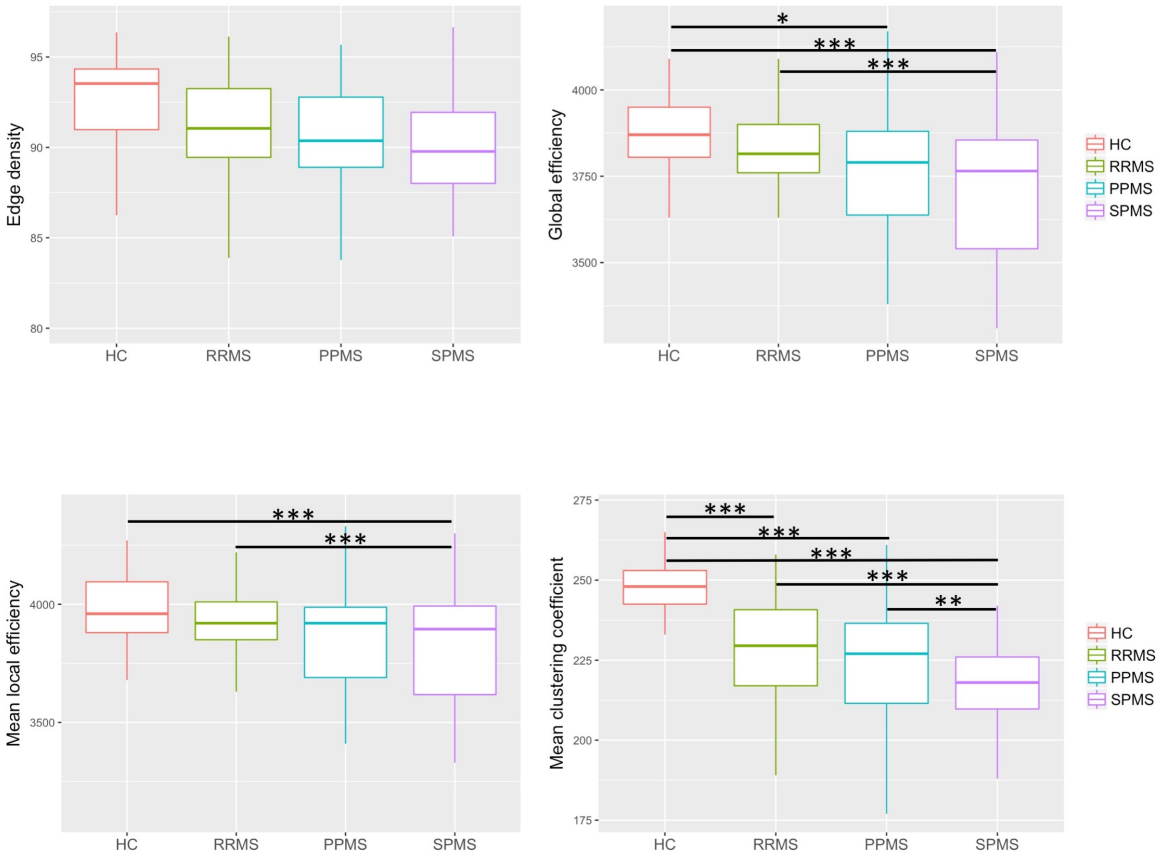

Figure 6.2. Boxplots of network metrics between the various groups

Boxplots show the unadjusted results. The bottom and the top of each box is the first and the third quantile, and the band inside is the median. The ends of the whiskers represent the lowest and the highest datum within 1.5 interquartile range. The statistical significance is denoted as * and this is after adjusting for age, gender, lesion load and total intracranial volume.

*p<0.05, **p<0.01, ***p<0.001

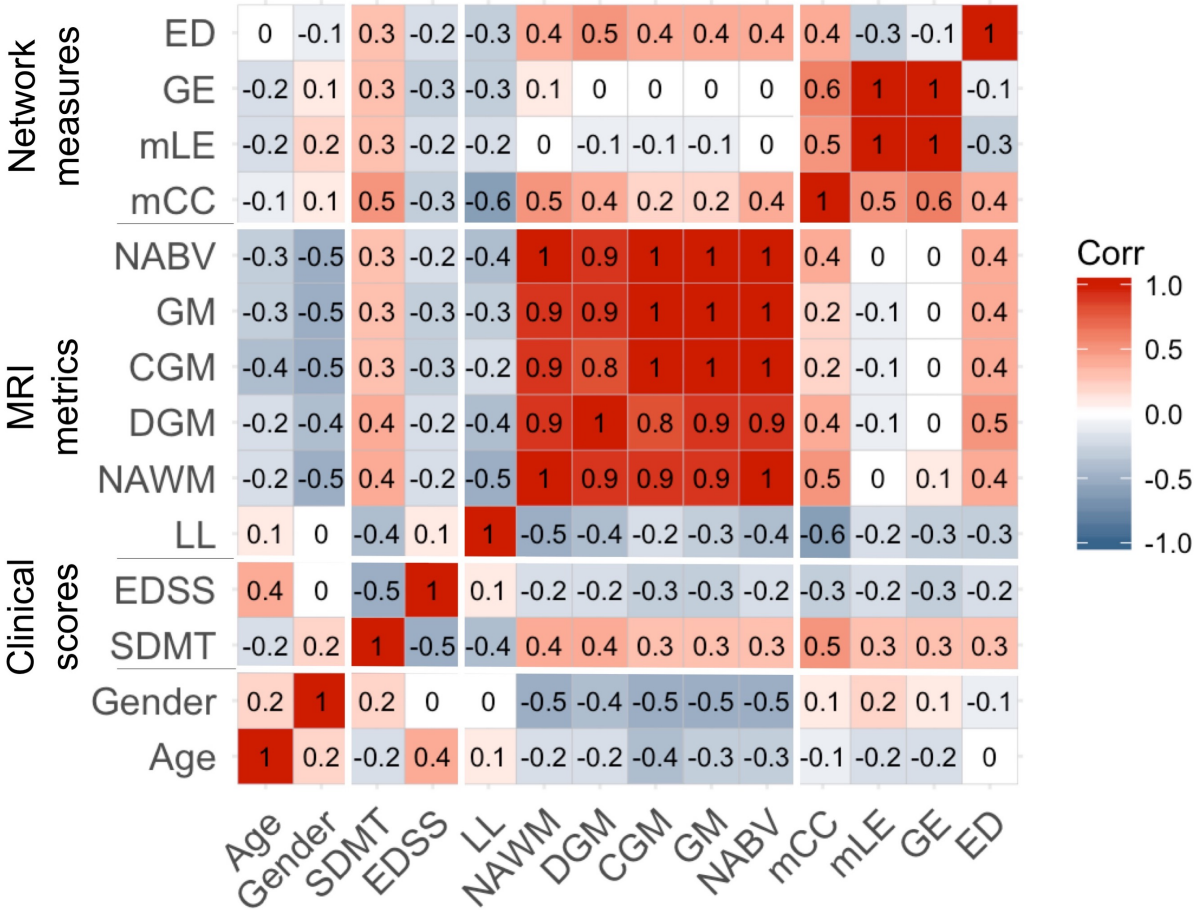

Figure 6.3. Descriptive pairwise univariable associations in patients

The reported value in each entry of the matrix corresponds to the pairwise Pearson correlation coefficient (r).

Abbreviations:

ED = Edge density; GE = global efficiency; mLE = mean local efficiency; mCC = mean clustering coefficient; NABV = normal appearing brain volume; GM = grey matter; CGM = cortical grey matter; DGM = deep grey matter; NAWM = normal appearing white matter; LL = lesion load; EDSS = Expanded Disability Status Scale; SDMT = Symbol Digit Modalities Test

Table 6.3. Stepwise linear regression for prediction of EDSS in multiple sclerosis

	Model summary + predictors	Regression Coefficient	95% CI	p-value
	MRI metrics			
EDSS score	Adj. R^2 = 0.185			
	NABV, cm^3	-0.0041	(-0.0077 to -0.00043)	**0.029**
	Age, years	0.081	(0.044 to 0.12)	**<0.001**
	Female	-0.73	(-1.66 to 0.20)	0.125
	MRI metrics + network measures			
EDSS score	Adj. R^2 = 0.205			
	NABV, cm^3	-0.0021	(-0.0061 to 0.0019)	0.297
	Edge density, %	-0.13	(-0.26 to -0.0014)	**0.047**
	Age, years	0.087	(0.051 to 0.12)	**<0.001**
	Female	-0.60	(-1.53 to 0.33)	0.202
	Adj. R^2 = 0.221			
	NABV, cm^3	-0.0037	(-0.0073 to -0.00016)	**0.041**
	Global efficiency	-0.0026	(-0.0048 to -0.00058)	**0.013**
	Age, years	0.072	(0.036 to 0.11)	**<0.001**
	Female	-0.52	(-1.44 to 0.40)	0.266
	Adj. R^2 = 0.206			
	NABV, cm^3	-0.0041	(-0.076 to -0.00049)	**0.026**
	mLE	-0.0019	(-0.0038 to -0.000044)	**0.045**
	Age, years	0.073	(0.036 to 0.11)	**<0.001**
	Female	-0.57	(-1.50 to 0.37)	0.231
	Adj. R^2 = 0.229			
	NABV, cm^3	-0.0016	(-0.005 to 0.007)	0.551
	mCC	-0.029	(-0.051 to -0.0075)	**0.008**
	Age, years	0.078	(-0.0042 to 0.0022)	**<0.001**
	Female	-0.30	(-1.26 to 0.66)	0.534
	Final model			
EDSS score	Adj. R^2 = 0.259			
	Edge density, %	-0.17	(-0.28 to -0.060)	**0.003**
	Global efficiency	-0.0031	(-0.0051 to -0.0011)	**0.003**
	Age, years	0.081	(0.047 to 0.12)	**<0.001**

Abbreviations: EDSS = Expanded Disability Status Scale; NABV = normal appearing brain volume; mLE = mean local efficiency; mCC = mean clustering coefficient; CI = confidence intervals

p – values in bold denote statistical significance at $p < 0.05$

Table 6.4. Stepwise linear regression for prediction of SDMT in multiple sclerosis

	Model summary + predictors	Regression Coefficient	95% CI	p-value
	MRI metrics			
SDMT score	Adj. R^2 = 0.361			
	DGM, cm^3	1.61	(0.79 to 2.43)	**<0.001**
	Lesion load, mL	-0.17	(-0.34 to -0.0014)	**0.048**
	Female	12.16	(5.51 to 18.82)	**<0.001**
	MRI metrics + network measures			
SDMT score	Adj. R^2 = 0.352			
	DGM, cm^3	1.52	(0.61 to 2.43)	**0.001**
	Lesion load, mL	-0.17	(-0.34 to 0.0069)	0.059
	Edge density, (%)	0.24	(-0.75 to 1.23)	0.624
	Female	11.94	(5.18 to 18.70)	**<0.001**
	Adj. R^2 = 0.396			
	DGM, cm^3	1.93	(1.21 to 2.65)	**<0.001**
	Global efficiency	0.021	(0.0055 to 0.035)	**0.008**
	Female	10.97	(4.37 to 17.56)	**0.002**
	Adj. R^2 = 0.380			
	DGM, cm^3	2.01	(1.28 to 2.75)	**<0.001**
	mLE	0.015	(0.0028 to 0.028)	**0.018**
	Female	11.43	(4.79 to 18.06)	**0.001**
	Adj. R^2 = 0.387			
	DGM, cm^3	1.45	(0.63 to 2.28)	**<0.001**
	mCC	0.21	(0.047 to 0.38)	**0.013**
	Female	9.92	(2.98 to 16.85)	**0.006**
	Final model			
SDMT score	Adj. R^2 = 0.396			
	DGM, cm^3	1.93	(1.21 to 2.65)	**<0.001**
	Global efficiency	0.021	(0.0055 to 0.035)	**0.008**
	Female	10.97	(4.36 to 17.56)	**0.002**

Abbreviations: SDMT = Symbol Digit Modalities Test; DGM = deep grey matter; mLE = mean local efficiency; mCC = mean clustering coefficient; CI = confidence intervals

p – values in bold denote statistical significance at $p < 0.05$

Appendix A Supplemental results

eTable 6.1: Characteristics of the participants with and without SDMT score

	Whole MS population (n = 122)	MS Population with SDMT (n = 60)	MS Population without SDMT (n = 62)	p-value
Subtypes	RRMS = 58 PPMS = 28 SPMS = 36	RRMS = 28 PPMS = 14 SPMS = 18	RRMS = 29 PPMS = 15 SPMS = 18	0.98[a]
Age, years	48 ± 11	47 ± 11	49 ± 10	0.48[b]
Gender (M/F)	36/86	18/42	18/44	0.99[a]
Disease duration, years	15 ± 10	16 ± 11	14 ± 8	0.29[b]
EDSS, median	5.5 (0-8.5)	4.5 (1.0-8.5)	6 (0 - 8.5)	0.07[b]

Values listed are mean ± standard deviation (SD)

Comparison was performed between the MS population with and without SDMT

[a] chi Square test

[b] Student t-test for independent samples

Abbreviations: MS = multiple sclerosis; RRMS = relapsing-remitting MS; PPMS = primary progressive MS; SPMS = secondary progressive MS; EDSS = Expanded Disability Scale Status; SDMT = Symbol Digit Modality Test;

eTable 6.2: Depression and fatigue levels of the participants with SDMT scores

	HC	MS patients	RRMS	PPMS	SPMS
Anxiety					
Mean ± SD	4.72 ± 3.90	6.31 ± 3.68	6.28 ± 3.72	5.54 ± 4.03	7.08 ± 3.42
% (no) subjects	92 (11)	78 (47)	93 (26)	73 (11)	67 (12)
Depression					
Mean ± SD	2.74 ± 2.46	5.92 ± 3.46	5.43 ± 3.56	6.25 ± 3.88	6.83 ± 2.79
% (no) subjects	92 (11)	78 (47)	93 (26)	73 (11)	67 (12)
Fatigue					
Mean ± SD	3.05 ± 2.75	4.36 ± 2.51	4.03 ± 2.18	4.40 ± 2.67	4.97 ± 3.06
% (no) subjects	92 (11)	78 (47)	93 (26)	73 (11)	67 (12)

Values listed are mean ± standard deviation (SD).

Fatigue was measured using a 10cm Visual Analogue Scale. Depression and Anxiety scores were recorded using the Hospital Anxiety and Depression Scale.

Abbreviations: HC = healthy controls; MS = multiple sclerosis; RRMS = relapsing-remitting MS; PPMS = primary progressive MS; SPMS = secondary progressive MS;

A. Volumetric differences between HC and MS patients and subtypes

There was a significant decrease in the volumes of BV, GM, CGM, DGM and WM (all $p < 0.05$) in patients compared with HC after adjusting age, gender and LL. Examining the MS subtypes, RRMS and SPMS had lower volumes (BV, GM, WM, CGM, DGM) adjusted for age, gender and LL (all $p < 0.05$) when compared with HCs. PPMS group also had lower BV, DGM and WM (all $p < 0.05$) whereas the decrease in CGM volume vs HCs showed borderline significance ($p = 0.063$ adjusted for age, gender and LL). See **eTable 6.3 (supplemental**).

eTable 6.3: Between group differences in MRI metrics

	Volume metrics											
	MS patients (n = 122)			**RRMS (n = 58)**			**PPMS (n = 28)**			**SPMS (n = 36)**		
	RC	**95% CI**	**p-value**	**RC**	**95% CI**	**p-value**	**RC**	**95% CI**	**p-value**	**RC**	**95% CI**	**p-value**
BV (cm^3)	-79.51	(-112.40 to -46.62)	**<0.001**	-64.86	(-100.57 to -29.15)	**<0.001**	-69.33	(-115.35 to 23.31)	**0.034**	-126.86	(-170.95 to 82.77)	**<0.001**
GM (cm^3)	-30.67	(-47.68 to -13.65)	**<0.001**	-24.80	(-43.40 to -6.19)	**0.0093**	-24.21	(-48.19 to -0.23)	**0.048**	-51.77	(-74.74 to -28.80)	**<0.001**
CGM (cm^3)	-26.97	(-43.08 to 10.85)	**0.0012**	-21.36	(-39.01 to 3.72)	**0.018**	-21.59	(-44.32 to 1.15)	0.063	-46.42	(-68.20 to -24.64)	**<0.001**
DGM (cm^3)	-3.70	(-4.84 to -2.55)	**<0.001**	-3.43	(-4.67 to 2.20	**<0.001**	-2.62	(-4.21 to -1.03)	**0.0014**	-5.35	(-6.87 to -3.83)	**<0.001**
WM (cm^3)	-26.97	(-43.08 to -10.85)	**0.0012**	-27.26	(-43.72 to -10.81)	**0.0013**	-28.60	(-49.80 to -7.39)	**0.0085**	-59.88	(-80.20 to -39.56)	**<0.001**
LL[a] (mL)		-			-		3.78	(-3.50 to 11.06)	0.306	2.46	(-4.26 to 9.17)	0.470

Abbreviations: MS = multiple sclerosis; RRMS = relapsing-remitting MS; PPMS = primary progressive MS; SPMS = secondary progressive MS; LL = Lesion load; BV = brain volume; GM = grey matter; CGM = cortical grey matter; DGM = deep grey matter; WM = white matter; RC = regression coefficient; CI = confidence intervals

p -values in bold denote statistical significance at $p < 0.05$ when compared to controls and adjusted for age, gender and lesion load

[a] Lesion load was compared against relapsing-remitting group

Bibliography

Andersson JL and Sotiropoulos SN. (2016) An integrated approach to correction for off-resonance effects and subject movement in diffusion MR imaging. *Neuroimage* 125: 1063-1078.

Bhushan C, Haldar JP, Joshi AA, et al. (2012) Correcting Susceptibility-Induced Distortion in Diffusion-Weighted MRI using Constrained Nonrigid Registration. *Signal Inf Process Assoc Annu Summit Conf APSIPA Asia Pac* 2012.

Bullmore E and Sporns O. (2012) The economy of brain network organization. *Nat Rev Neurosci* 13: 336-349.

Cardoso MJ, Modat M, Wolz R, et al. (2015) Geodesic Information Flows: Spatially-Variant Graphs and Their Application to Segmentation and Fusion. *IEEE Trans Med Imaging* 34: 1976-1988.

Cercignani M and Gandini Wheeler-Kingshott C. (2018) From micro- to macro-structures in multiple sclerosis: what is the added value of diffusion imaging. *NMR Biomed*.

Clayden J, Maniega SM, Stokey AJ, et al. (2011) TractoR: Magnetic Resonance Imaging and Tractography with R. *JSS*.

Dineen RA, Vilisaar J, Hlinka J, et al. (2009) Disconnection as a mechanism for cognitive dysfunction in multiple sclerosis. *Brain* 132: 239-249.

Douw L, Schoonheim MM, Landi D, et al. (2011) Cognition is related to resting-state small-world network topology: an magnetoencephalographic study. *Neuroscience* 175: 169-177.

Fleischer F, Gröger A, Koirala N, et al. (2017) Increased structural white and grey matter network connectivity compensates for functional decline in early multiple sclerosis. *Multiple Sclerosis Journal* 23: 432–441.

Friese MA, Schattling B and Fugger L. (2014) Mechanisms of neurodegeneration and axonal dysfunction in multiple sclerosis. *Nat Rev Neurol* 10: 225-238.

Kocevar G, Stamile C, Hannoun S, et al. (2016) Graph Theory-Based Brain Connectivity for Automatic Classification of Multiple Sclerosis Clinical Courses. *Front Neurosci* 10: 478.

Kurtzke JF. (1983) Rating neurologic impairment in multiple sclerosis: an expanded disability status scale (EDSS). *Neurology* 33: 1444-1452.

Liu Y, Wang H, Duan Y, et al. (2017) Functional Brain Network Alterations in Clinically Isolated Syndrome and Multiple Sclerosis: A Graph-based Connectome Study. *Radiology* 282: 534-541.

Llufriu S, Martinez-Heras E, Solana E, et al. (2017) Structural networks involved in attention and executive functions in multiple sclerosis. *Neuroimage Clin* 13: 288-296.

Lublin FD and Reingold SC. (1996) Defining the clinical course of multiple sclerosis: results of an international survey. National Multiple Sclerosis Society (USA) Advisory Committee on Clinical Trials of New Agents in Multiple Sclerosis. *Neurology* 46: 907-911.

Mangeat G, Badji A, Ouellette R, et al. (2018) Changes in structural network are associated with cortical demyelination in early multiple sclerosis. *Hum Brain Mapp* 39: 2133-2146.

Muthuraman M, Fleischer V, Kolber P, et al. (2016) Structural Brain Network Characteristics Can Differentiate CIS from Early RRMS. *Front Neurosci* 10: 14.

Panicker JN, Fowler CJ and Kessler TM. (2015) Lower urinary tract dysfunction in the neurological patient: clinical assessment and management. *Lancet Neurol* 14: 720-732.
Pardini M, Yaldizli O, Sethi V, et al. (2015) Motor network efficiency and disability in multiple sclerosis. *Neurology* 85: 1115-1122.
Prados F, Cardoso MJ, Kanber B, et al. (2016b) A multi-time-point modality-agnostic patch-based method for lesion filling in multiple sclerosis. *Neuroimage* 139: 376-384.
Raffelt D, Tournier JD, Rose S, et al. (2012) Apparent Fibre Density: a novel measure for the analysis of diffusion-weighted magnetic resonance images. *Neuroimage* 59: 3976-3994.
Rocca MA, Amato MP, De Stefano N, et al. (2015) Clinical and imaging assessment of cognitive dysfunction in multiple sclerosis. *Lancet Neurol* 14: 302-317.
Rocca MA, Valsasina P, Meani A, et al. (2016) Impaired functional integration in multiple sclerosis: a graph theory study. *Brain Struct Funct* 221: 115-131.
Rubinov M and Sporns O. (2010) Complex network measures of brain connectivity: uses and interpretations. *Neuroimage* 52: 1059-1069.
Schoonheim MM, Hulst HE, Landi D, et al. (2012) Gender-related differences in functional connectivity in multiple sclerosis. *Mult Scler* 18: 164-173.
Schoonheim MM, Meijer KA and Geurts JJ. (2015) Network collapse and cognitive impairment in multiple sclerosis. *Front Neurol* 6: 82.
Shu N, Duan Y, Xia M, et al. (2016) Disrupted topological organization of structural and functional brain connectomes in clinically isolated syndrome and multiple sclerosis. *Sci Rep* 6: 29383.
Shu N, Liu Y, Li K, et al. (2011) Diffusion tensor tractography reveals disrupted topological efficiency in white matter structural networks in multiple sclerosis. *Cereb Cortex* 21: 2565-2577.
Smith RE, Tournier JD, Calamante F, et al. (2012) Anatomically-constrained tractography: improved diffusion MRI streamlines tractography through effective use of anatomical information. *Neuroimage* 62: 1924-1938.
Smith RE, Tournier JD, Calamante F, et al. (2015b) SIFT2: Enabling dense quantitative assessment of brain white matter connectivity using streamlines tractography. *Neuroimage* 119: 338-351.
Tewarie P, Schoonheim MM, Schouten DI, et al. (2015) Functional brain networks: linking thalamic atrophy to clinical disability in multiple sclerosis, a multimodal fMRI and MEG study. *Hum Brain Mapp* 36: 603-618.
Tewarie P, Steenwijk MD, Tijms BM, et al. (2014) Disruption of structural and functional networks in long-standing multiple sclerosis. *Hum Brain Mapp* 35: 5946-5961.
Tournier JD, Calamante F and Connelly A. (2007) Robust determination of the fibre orientation distribution in diffusion MRI: non-negativity constrained super-resolved spherical deconvolution. *Neuroimage* 35: 1459-1472.
Tuladhar AM, van Uden IWM, Loes C.A. Rutten-Jacobs LCA, et al. (2016) Structural network efficiency predicts conversion to dementia. *Neurology* 86: 1112-1119.
van de Pavert SH, Muhlert N, Sethi V, et al. (2016) DIR-visible grey matter lesions and atrophy in multiple sclerosis: partners in crime? *J Neurol Neurosurg Psychiatry* 87: 461-467.
Yeh CH, Smith RE, Liang X, et al. (2016) Correction for diffusion MRI fibre tracking biases: The consequences for structural connectomic metrics. *Neuroimage* 142: 150-162.

Chapter 7

7. Longitudinal analysis framework for structural brain networks with application to multiple sclerosis

Summary

In this chapter, we considered the problem of reconstructing brain networks, where diffusion-weighted and T1-weighted magnetic resonance images have been acquired at multiple time-points for the same subject. We introduced a method for registering diffusion-weighted and structural scans in a subject-specific half-way space and we demonstrated that half-way space-derived network metrics are strongly correlated with native space-derived network metrics. We also reported sufficient agreement between the two techniques in a cohort comprising of 12 healthy controls and 12 multiple sclerosis patients. The results remained unaffected when the analyses were evaluated in controls and patients separately. The findings of this chapter might be of particular interest in longitudinal structural network studies assessing network changes over time in normal and disease conditions.

Scientific contribution

The results presented in this chapter have been published in peer-review book chapter as: **Longitudinal analysis framework of DWI data for reconstructing structural brain networks with application to multiple sclerosis**. *Computational Diffusion MRI*.

7.1. Introduction

As discussed in previous sections diffusion MRI allows the non-invasive investigation of tissue microstructure and it is an increasingly popular technique for reconstructing structural brain networks. Network-based analyses have provided valuable insights into the mechanisms underlying brain function and how pathology may affect them. However, to date this has been limited to cross-sectional (single time-point) analyses. Longitudinal studies have the potential to provide valuable insights into the dynamics of network function, their decline and collapse due to pathology, and would establish whether or not network-based outcome measures are sufficiently sensitive to change to be viable measures of treatment efficacy.

From an imaging analysis perspective, specialised techniques are required in order to take advantage of the longitudinal study designs without introducing any potential biases. For instance, a possible bias could arise by not treating all time-points the same way i.e. when follow-up images are resampled (the process of transforming/rotating a sampled image from one coordinate system to another) to the baseline scans. This can cause a noticeable reduction in image quality (smoothing) in the follow-up scan leaving the baseline scan intact which means that longitudinal changes would be overestimated (Reuter and Fischl, 2011). To avoid this, structural scans from all available time-points have been proposed to be transformed into an unbiased within-subject template ensuring equal treatment of all images (hereinafter referred to as half-way space) (Reuter et al., 2012). Recently, the half-way space approach has been extended to longitudinal diffusion-weighted data and it was combined with tensor-based registration to achieve images alignment within and across subjects (Keihaninejad et al., 2013). Moreover, the application of the longitudinal tractography framework improved the reliability and sensitivity of the

reconstructed tractogram when compared to data reconstructed at each time point independently (Yendiki et al., 2016). Collectively, these studies provide evidence that the use of half-way template may be an effective approach in assessing structural or diffusion metrics' changes due to disease progression.

To date, there are limited number of diffusion-derived networks (Tuladhar et al., 2016; Nir et al., 2015) with more than one time-point and none of these studies used a longitudinal framework in their analyses. Considering the given advantages of the longitudinal approach (half-way registration) in imaging processing, it is likely that such an approach could be used when assessing network analysis over time. However, the effects of such registration on networks has not been examined yet. This is particularly important as resampling of diffusion-weighted scans requires both registration of the spatial information and the correct reorientation of the corresponding diffusion-weighting gradient directions, a step that could be a potential source of bias. With these in mind, we aimed to:

1. to propose a longitudinal network pipeline combining the best practices for unbiased processing of structural data with diffusion data
2. to demonstrate that tractogram reconstruction in half-way space is feasible
3. to evaluate the effects of the pipeline on the network metrics by comparing them against the network metrics derived from native space.
4. to stress test our method testing whether these effects were different between HC and MS patients.

7.2. Methods

7.2.1. Participants

Twelve HC (6 males; mean age 36 ± 13 years) and 61 MS (21 males; mean age 47 ± 11 years), were scanned at two time-points, approximately two years apart (1.84 ± 0.55 years). For this study, we selected, MS patients who were ranked above the 20th centile for whole brain LL (n=12). This is because we wanted to investigate whether the degree of the visible inflammation will affect differently our network metrics when compared with the control group. This work has been approved by the local institutional ethics committee and written consent was obtained from all the patients.

7.2.2. MRI data acquisition

This is the same as in previous experimental chapters. Briefly, MRI data were acquired on a Philips Achieva 3T MR scanner (Philips Healthcare, Best, Netherlands) with a 32-channel head coil using: (1) 3D sagittal T1-weighted scans with a fast-field echo scan, (2) whole brain HARDI scan with EPI consisted of a cardiac-gated SE sequence and (3) dual-echo proton density/T2-weighted axial oblique-scans.

7.2.3. Overview of the longitudinal pipeline

Structural images pre-processing

As discussed in previous chapters, affine transformation was performed to register the subject's non-filled T1-weighted bias-field corrected image to the corresponding DWI using BrainSuite v.15b (Bhushan et al., 2012) of the appropriate time point. The target volume was the first b0 image after DWI pre-processing, resulting in a structural image of resolution 2x2x2 mm^3. T2-hyperintense lesions were affine transformed to DWI

space and then filled on the T1-weighted images using a modality-agnostic patch-based method (Prados et al., 2016b).

Diffusion-weighted imaging pre-processing

The mean b0 image was rigid registered to the first b0 image. Then, the same rigid transformation was applied to the 61 DWI volumes. FSL v5.0.9 was used on the DWI data to correct for eddy current and head motion (Andersson and Sotiropoulos, 2016) and BrainSuite v.15b to correct for EPI distortions (Bhushan et al., 2012).

Within-subject registration for diffusion-weighted and structural images

We performed pairwise symmetric rigid registrations of the mean b0 image to obtain transformation matrices between each pair of images using NiftyReg (http://niftyreg.sf.net) (Leung et al., 2012). For each image, we computed the geometric log mean of pairwise affine transformations (Alexa, 2002)

Following this step, both diffusion-weighted and anatomical images from all time-points were transformed into a common unbiased half-way space. In addition, we rotated the diffusion gradient vectors applying their corresponding transformation between native and half-way space. Subsequent processing of the diffusion-weighted and structural images was performed in this subject-specific space.

Tissue segmentation and parcellation

Brain tissue was segmented and parcellated as discussed in **section 5.2.3 (chapter 5)**. Briefly, the T1-weighted images were segmented into CGM, WM, DGM, brainstem and CSF and parcellated into anatomically distinct subregions using the GIF framework v2.0 (Cardoso et al., 2015). GIF is free available as webservice at http://cmictig.cs.ucl.ac.uk/niftyweb (Prados et al., 2016a). The generated WM and

brain- stem tissues were joined together to form the appropriate tissue as required for ACT algorithm (Smith et al., 2012).

Tractogram reconstruction

As discussed in **section 5.2.3** (**chapter 5)** for diffusion-weighted post-processing, we used algorithms from the MRtrix3 v0.3.14 package (http://www.mrtrix.org). We estimated the response function (Tax et al., 2014) and followed by CSD to model fibre orientation distributions (Tournier et al., 2007; Tournier et al., 2004). Then, we used iFOD2 algorithm (Tournier et al., 2010) to generate one tractogram per subject with 10^7 streamlines in combination with ACT (Smith et al., 2012) followed by SIFT2 (Smith et al., 2015b).

To visualise the reconstructed tractogram we performed whole-brain directionally-encoded colour track-density mapping (TDI) (Calamante et al., 2010).

Structural brain network reconstruction

The SIFT2 re-weighted streamlines from the previous step were then assigned to the closest node as defined by the GIF parcellation framework (Cardoso et al., 2015). A range of network metrics including edge density, global efficiency, mean local efficiency and mean clustering coefficient were computed using the TractoR package (Clayden et al., 2011). Summary of the longitudinal pipeline is illustrated in **Fig. 7.1**.

7.2.4. Overview of the baseline pipeline

This is the same pipeline that was discussed in **chapter 5.** Briefly, we used the first time-point and followed the exact same pipeline as described above. By default, there were no subject-specific half-way registrations. The same network metrics were extracted that allowed us to perform the correlations. Here after the metrics derived

with this pipeline will be referred to as native metrics as opposed to the half-way metrics. **Fig. 7.2** summarises the baseline pipeline.

7.2.5. Statistical analysis

Statistical analysis was performed using R software (https://www.r-project.org) v3.3.0. We used Pearson correlation analysis to investigate the level of correlation between baseline native and baseline half-way space network metrics. To further investigate the agreement between the two methods we used Bland-Altman plots (Bland and Altman, 1986). The plots display the difference between the metrics against their mean. We computed each point on the Bland-Altman plot for each subject using the following equation

$$M_{i(x,y)} = (0.5(M_1 + M_2\,, M_1 - M_2))$$

Eq. 7.1

where M_1 and M_2 are the metric values (native and half-way network metrics) for the subject i.

For all the models, we explored whether there was a violation of normality assumption of the residuals. Data are reported as mean (± SD), unless otherwise stated. P-values < 0.05 were considered statistically significant.

7.3. Results

Visual inspection of track-density map

Fig. 7.3 demonstrates the track-density maps generated in native and half-way space. Visual inspection of these demonstrated that: a) the tractograms appeared to be normal without any obvious abnormalities, b) tractography in half-way space was feasible and c) the half-way space tractograms were similar as the ones in native space.

Correlation of the network metrics at native and half-way space

We derived a range of commonly used network metrics from native and half-way space. We firstly assessed the Pearson correlations of the whole brain network-derived measures combining the MS and HC groups as shown in **Table 7.1**. As can be seen there was a significant positive correlation ($r \geq 0.94$, $p < 0.001$) of all the network measures examined. To examine whether the effect of registration in half-way space was different in the control group compared to MS group, we estimated the correlation coefficient of the network metrics for each group separately. We observed strong positive correlation between the network metrics derived in native and half-way space for both HC and MS subjects ($r \geq 0.80$, $p < 0.001$) **(Table 7.1; Fig. 7.4).**

Bland-Altman analysis of the network metrics at native and half-way space

Finally, we used Bland-Altman analysis to evaluate the degree of agreement between the two pipelines. **Fig. 7.5** showed Bland-Altman plots for edge density, global efficiency, mean local efficiency and mean clustering coefficient computed from native and half-way space. The mean bias (% ± SD) for edge density computation is +1.08 ±

1.55%, for global efficiency is -2.05 ± 2.07%, for mean local efficiency is -2.33 ± 1.95% and for mean clustering coefficient is -1.39 ± 2.14% in the half-way against the native space. The mean bias estimation was consistent when different groups were examined **(Table 7.2; Fig. 7.5**)

7.4. Discussion

In this chapter, we introduced a novel method that extends the longitudinal registration framework beyond the anatomical and diffusion-weighted data. Using registration best practices, we have successfully derived network metrics from networks that have been previously registered in the half-way space.

Firstly, we demonstrated a strong correlation between native and half-way space-derived network metrics. Importantly, these results were further confirmed when data from HC and MS patients were analysed separately. Especially for the latter group, we chose to apply our method on participants who had very high LL (top 20%) in order to stress test our methods mainly because it is known that diffusion metrics are affected in lesional brains (Werring et al., 1999). The results demonstrated that the correlation was maintained when both controls and patients were examined separately. Of note, edge density showed slightly lower correlation between native and half-way metrics in MS compared to the other metrics. Edge density was derived from a binary network, by definition, meaning that for this metric only the presence or absence of a connection is considered. The lower correlation in the multiple sclerosis group only, might suggest that slightly misregistered lesions may interrupt the underlying FODs and ultimately causing disruption of connections. The rest of the network measures were derived from a weighted network and hence did not suffer from this issue. This is because a zero weight and a small weight have a similar effect on the total variance. Nonetheless, by demonstrating a strong correlation between structural network metrics derived in native and half-way space in a group with very high structural brain abnormalities suggests that the pipeline is likely to perform at least as well across the whole spectrum of the disease.

To further evaluate our approach, we used Bland-Altman plots to examine the similarity between the two methods. These results supported the correlation observations demonstrating a sufficient agreement with the mean bias limited to less than 2.5 % between the two pipelines. Importantly, this agreement was independent of pathology providing further evidence that supports the applicability of this technique in disease state and more specifically in disorders with substantial WM damage.

Moreover, we have demonstrated that registration of diffusion-weighted data in half-way space was successful as evaluated by the reconstructed directionally-encoded colour TDI maps **(Fig. 7.3)**. In traditional scalar image registration, there is a lot of focus on spatial alignment. This is not the case in diffusion-weighted data as they require both spatial image registration and re-orientation of the gradient directions constituting diffusion-weighted image registration much more complex and challenging (Alexander et al., 2001; Zhang et al., 2006). Here, indeed, we demonstrated correct data registration and reorientation of the voxel-wise signal profile into a half-way space suggesting the feasibility of such an approach.

Some limitations apply to this work. In the proposed method, the same steps were followed to both time-points during network reconstruction avoiding thus any interpolation asymmetry induced bias (Keihaninejad et al., 2013). However, our analyses did not examine whether the technique presented here reduced the network metrics variability when compared to the native metrics. Such results could be suggestive of the advantages that our method might hold. One way to examine this, was to assess the specificity and sensitivity of each pipeline using a test-retest design. However, due to the absence of such a dataset we could not perform this analysis. Nonetheless, the use of the multiple time-point technique allows the investigator to extract structural, diffusion or network metrics while all the scans are

registered in a common space, extending the technique beyond the already established frameworks (Reuter et al., 2012; Keihaninejad et al., 2013).

7.5. Conclusion

In conclusion, we have shown for the first time a pipeline for structural brain network reconstruction from longitudinally acquired diffusion-weighted data. Our approach takes advantage of the already established within-subject registration techniques that have been successfully used in anatomical and diffusion data. In general, there was good agreement between network measures derived from scans processed in native and half-way space, indicating that our pipeline does not substantially degrade measures while bringing longitudinally acquired data into alignment. This pipeline enables longitudinal studies on structural network characteristics and appears sufficiently robust to allow this even in the presence of substantial brain abnormalities. **Chapter 8** will use the proposed pipeline to investigate the predictive value, if any, of the baseline network metrics in follow-up volumetric changes.

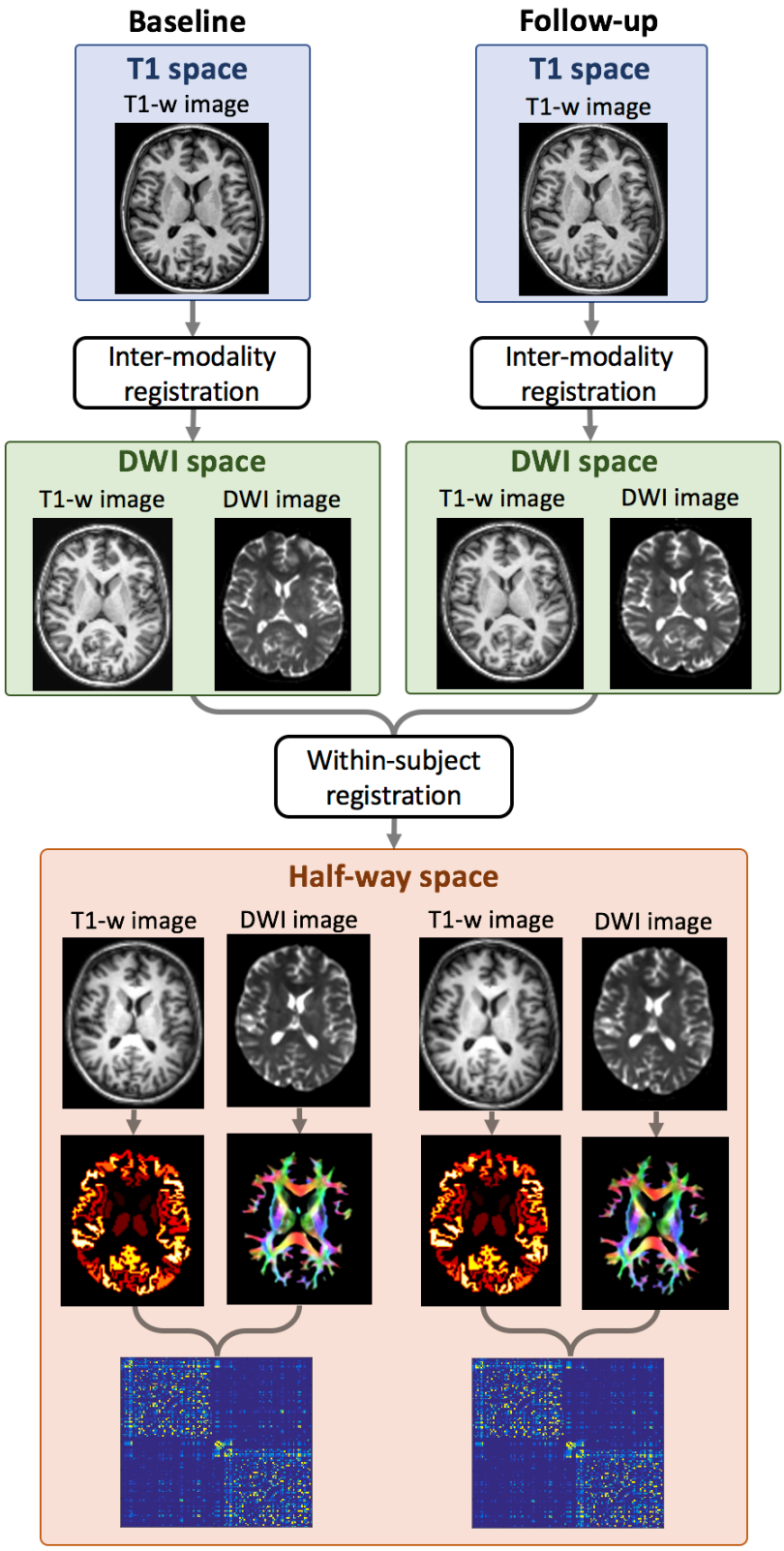

Figure 7.1. Overview of the longitudinal brain network reconstruction pipeline

Abbreviations: T1-w = T1 weighted image; DWI = diffusion-weighted image

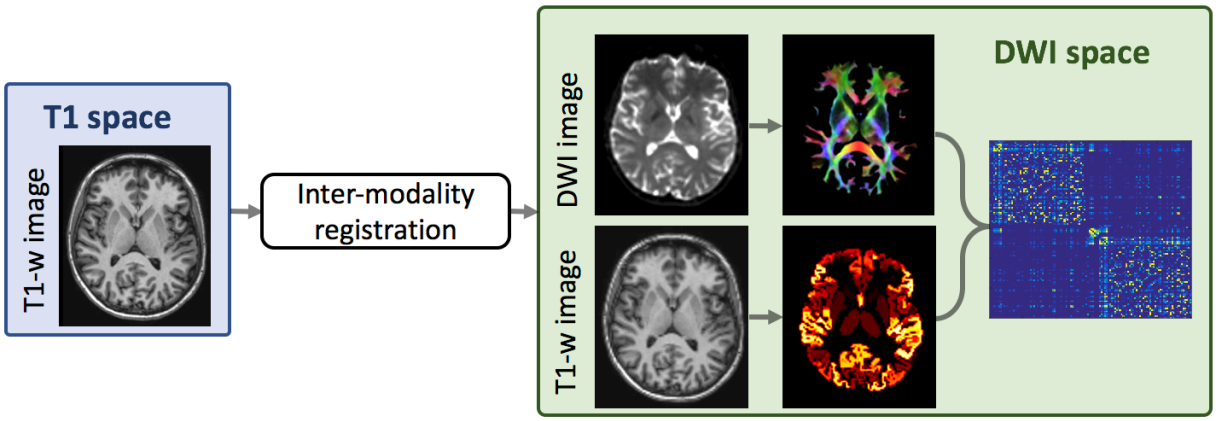

Figure 7.2. Overview of the baseline brain network reconstruction pipeline

Abbreviations: T1-w = T1 weighted image; DWI = diffusion-weighted image

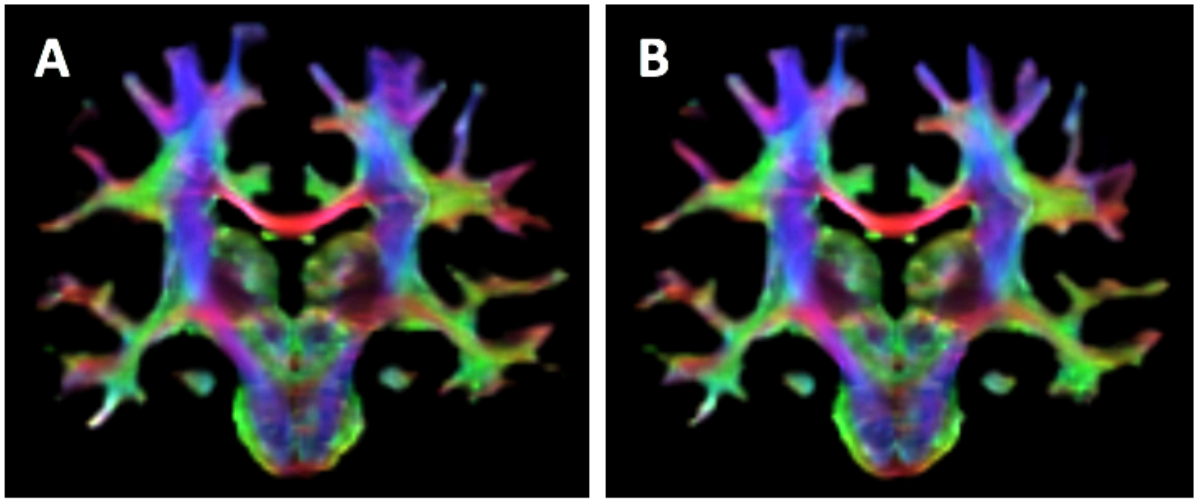

Figure 7.3. Quality check of track-density imaging

Super-resolution directionally-encoded color track-density imaging (TDI) map reconstructed in native **(A)** and half-way space **(B)**.

Network metrics	Whole group	Healthy controls	MS patients
Edge density	r = 0.94***	r = 0.93***	r = 0.80***
Global efficiency	r = 0.95***	r = 0.94***	r = 0.94***
Mean local efficiency	r = 0.98***	r = 0.98***	r = 0.96***
Mean clustering coefficient	r = 0.98***	r = 0.94***	r = 0.92***

Table 7.1. Pearson correlation coefficients between native and half-way space network metrics

*P < 0.05, **P < 0,001, ***P < 0.001

Abbreviations: MS = multiple sclerosis; r = Pearson correlation coefficient

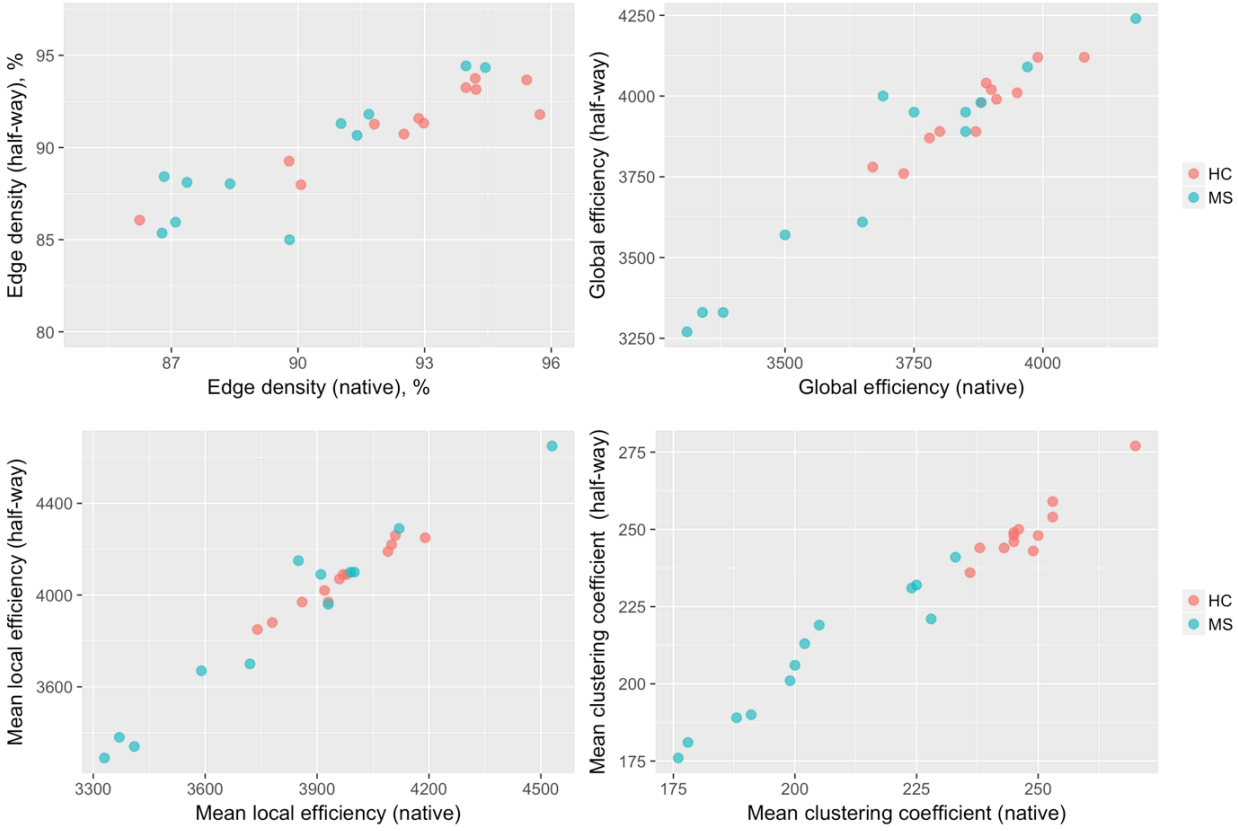

Figure 7.4. Scatterplots of networks metrics

Scatterplots of edge density, global efficiency, mean local efficiency and mean clustering coefficient derived from native and half-way space.

Abbreviations: HC = healthy controls; MS = multiple sclerosis

Network metrics	Whole group	Healthy controls	MS patients
Edge density	1.08 ± 1.55%	1.45 ± 1.12%	0.70 ± 1.87%
Global efficiency	-2.05 ± 2.07%	-2.17 ± 1.04%	-1.92 ± 2.85%
Mean local efficiency	-2.33 ± 1.95%	-2.55 ± 0.70%	-2.10 ± 2.75%
Mean clustering coefficient	-1.39 ± 2.14%	-0.84 ± 1.50%	-2.06 ±2.78%

Table 7.2. Bland-Altman analysis for network metrics derived from network and half-way space

In this table, the difference between native and half-way metrics divided by the mean of each metric is expressed as a percentage

Abbreviations: MS = multiple sclerosis

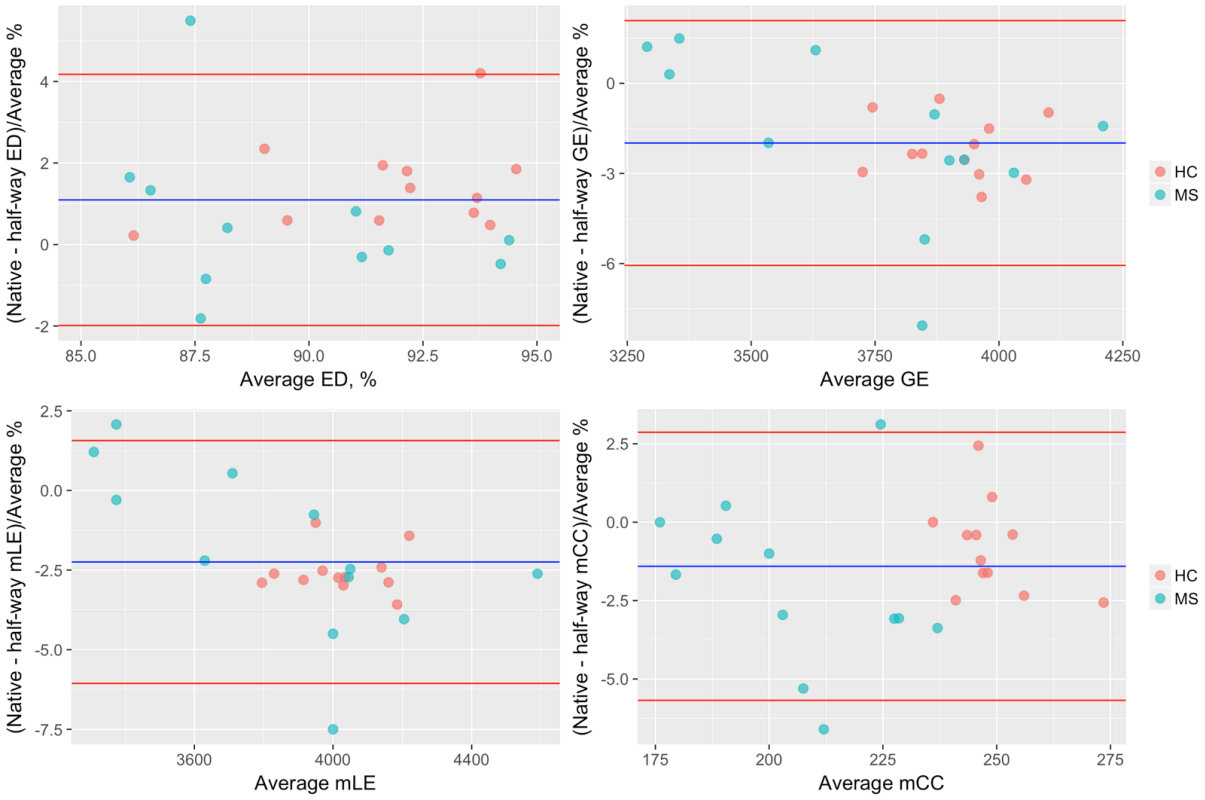

Figure 7.5. Bland-Altman plots of network metrics

Bland-Altman plots of edge density, global efficiency and mean local efficiency, mean clustering coefficient derived from native and half-way space. Blue line corresponds to the mean of the whole group and red lines indicate 1.96xSD.

Abbreviations: ED = edge density; GE = global efficiency; mLE = mean local efficiency; mCC = mean clustering coefficient

Bibliography

Alexa M. (2002) Linear combination of transformations. *Proceedings of the 29th Annual Conference on Computer Graphics and Interactive Techniques.* New York, NY, USA: SIGGRAPH '02, 380–387.

Alexander DC, Pierpaoli C, Basser PJ, et al. (2001) Spatial transformations of diffusion tensor magnetic resonance images. *IEEE Trans Med Imaging* 20: 1131-1139.

Andersson JL and Sotiropoulos SN. (2016) An integrated approach to correction for off-resonance effects and subject movement in diffusion MR imaging. *Neuroimage* 125: 1063-1078.

Bhushan C, Haldar JP, Joshi AA, et al. (2012) Correcting Susceptibility-Induced Distortion in Diffusion-Weighted MRI using Constrained Nonrigid Registration. *Signal Inf Process Assoc Annu Summit Conf APSIPA Asia Pac* 2012.

Bland JM and Altman DG. (1986) Statistical methods for assessing agreement between two methods of clinical measurement. *Lancet*: 307-310.

Calamante F, Tournier JD, Jackson GD, et al. (2010) Track-density imaging (TDI): super-resolution white matter imaging using whole-brain track-density mapping. *Neuroimage* 53: 1233-1243.

Cardoso MJ, Modat M, Wolz R, et al. (2015) Geodesic Information Flows: Spatially-Variant Graphs and Their Application to Segmentation and Fusion. *IEEE Trans Med Imaging* 34: 1976-1988.

Clayden J, Maniega SM, Stokey AJ, et al. (2011) TractoR: Magnetic Resonance Imaging and Tractography with R. *JSS*.

Keihaninejad S, Zhang H, Ryan NS, et al. (2013) An unbiased longitudinal analysis framework for tracking white matter changes using diffusion tensor imaging with application to Alzheimer's disease. *Neuroimage* 72: 153-163.

Leung KK, Ridgway GR, Ourselin S, et al. (2012) Consistent multi-time-point brain atrophy estimation from the boundary shift integral. *Neuroimage* 59: 3995-4005.

Nir TM, Jahanshad N, Toga AW, et al. (2015) Connectivity network measures predict volumetric atrophy in mild cognitive impairment. *Neurobiol Aging* 36 Suppl 1: S113-120.

Prados F, Cardoso MJ, Burgos N, et al. (2016a) NiftyWeb: web based platform for image processing on the cloud. *24th Scientific Meeting and Exhibition of the International Society for Magnetic Resonance in Medicine (ISMRM).* ISMRM.

Prados F, Cardoso MJ, Kanber B, et al. (2016b) A multi-time-point modality-agnostic patch-based method for lesion filling in multiple sclerosis. *Neuroimage* 139: 376-384.

Reuter M and Fischl B. (2011) Avoiding asymmetry-induced bias in longitudinal image processing. *Neuroimage* 57: 19-21.

Reuter M, Schmansky NJ, Rosas HD, et al. (2012) Within-subject template estimation for unbiased longitudinal image analysis. *Neuroimage* 61: 1402-1418.

Smith RE, Tournier JD, Calamante F, et al. (2012) Anatomically-constrained tractography: improved diffusion MRI streamlines tractography through effective use of anatomical information. *Neuroimage* 62: 1924-1938.

Smith RE, Tournier JD, Calamante F, et al. (2015b) SIFT2: Enabling dense quantitative assessment of brain white matter connectivity using streamlines tractography. *Neuroimage* 119: 338-351.
Tax CM, Jeurissen B, Vos SB, et al. (2014) Recursive calibration of the fiber response function for spherical deconvolution of diffusion MRI data. *Neuroimage* 86: 67-80.
Tournier JD, Calamante F and Connelly A. (2007) Robust determination of the fibre orientation distribution in diffusion MRI: non-negativity constrained super-resolved spherical deconvolution. *Neuroimage* 35: 1459-1472.
Tournier JD, Calamante F and Connelly A. (2010) Improved probabilistic streamlines tractography by 2nd order integration over fibre orientation distributions. *Joint Annual Meeting ISMRM-ESMRMB*.
Tournier JD, Calamante F, Gadian DG, et al. (2004) Direct estimation of the fiber orientation density function from diffusion-weighted MRI data using spherical deconvolution. *Neuroimage* 23: 1176-1185.
Tuladhar AM, van Uden IWM, Loes C.A. Rutten-Jacobs LCA, et al. (2016) Structural network efficiency predicts conversion to dementia. *Neurology* 86: 1112-1119.
Werring DJ, Clark CA, Barker GJ, et al. (1999) Diffusion tensor imaging of lesions and normal-appearing white matter in multiple sclerosis. *Neurology* 52: 1626-1632.
Yendiki A, Reuter M, Wilkens P, et al. (2016) Joint reconstruction of white-matter pathways from longitudinal diffusion MRI data with anatomical priors. *Neuroimage* 127: 277-286.
Zhang H, Yushkevich PA, Alexander DC, et al. (2006) Deformable registration of diffusion tensor MR images with explicit orientation optimization. *Med Image Anal* 10: 764-785.

Chapter 8

8. Baseline whole brain network measures predict future volumetric changes in multiple sclerosis

Summary

In this chapter, we evaluated the relationship between baseline diffusion-based network metrics and follow-up (interval from baseline 1.84 ± 0.55 years) brain damage, expressed either as brain atrophy or as visible inflammation hypothesising that baseline network parameters are harbingers of future brain changes. We applied the pipeline developed in **chapter 7** in 61 patients (41 females; age 47 ± 11 years; disease duration 17 ± 11 years) consisting of 27 relapsing-remitting (22 females; age 41 ± 11 years; disease duration 12 ± 9 years), 14 primary progressive (6 females; age 50 ± 10 years; disease duration 13 ± 8 years) and 20 secondary progressive (12 females; age 54 ± 7 years; disease duration 26 ± 10 years) and in 12 healthy controls (6 females; age 36 ± 13 years). Baseline and follow-up structural brain networks were reconstructed from diffusion-weighted magnetic resonance images and baseline network metrics including edge density, network efficiency and clustering coefficient were computed. Using multiple linear regression analysis, we demonstrated that higher baseline edge density predicted higher follow-up LL in relapsing-remitting ($p = 0.033$) whereas higher global ($p = 0.0019$) or local ($p = 0.0017$) efficiency predicted lower follow-up LL in primary progressive independently. The findings suggest that diffusion-based network metrics can be novel predictors of progression in multiple sclerosis.

Scientific contribution

The manuscript derived from this chapter has been reviewed internally and is going to be submitted in *Human Brain Mapping* peer-review journal.: **The predictive value of network metrics in multiple sclerosis: a longitudinal study.**

8.1. Introduction

Network measures are not only correlated with disability (Shu et al., 2011; Llufriu et al., 2017) but they can also explain disability better than conventional imaging metrics as discussed in **chapter 6** highlighting the clinical relevance of network-based approaches in MS. However, little is known about network metrics' predictive value for tissue damage. In fact, there is great interest in identifying predictors of brain damage in MS as not all patients have either the same rate of progression or they do not convert into more progressive phases at the same time. The limited longitudinal studies have provided evidence that higher baseline lesion volume predicts SPMS conversion from RRMS (Fisniku et al., 2008a) while more recently it was reported that cortical damage is a consequence of NAWM pathology as measured by MTR (Bodini et al., 2016). In this longitudinal study, using a novel longitudinal network pipeline presented in **chapter 7** we aimed for the first time:

1. to evaluate whether baseline network measures could predict future brain tissue abnormalities, either at the macroscopic level, i.e. greater lesion volume, or at the microscopic level, i.e. GM damage, ultimately causing tissue loss, i.e. atrophy.

8.2. Methods

8.2.1. Participants

Twelve HC (6 females; mean age 36 ± 13 years), 27 RRMS (22 females; mean age 41 ± 11 years), 14 PPMS (6 females, mean age 50 ± 10 years) and 20 SPMS (12 females; mean age 54 ± 7 years), were scanned at two time-points, approximately two years apart (1.84 ± 0.55 years). This work has been approved by the local institutional ethics committee and written consent was obtained from all the patients.

8.2.2. MRI data acquisition

MRI acquisition parameters were reported in **chapter 5**. Briefly, MRI data were acquired on a Philips Achieva 3T MR scanner (Philips Healthcare, Best, Netherlands) with a 32-channel head coil using: (1) 3D sagittal T1-weighted scans with a fast-field echo scan, (2) whole brain HARDI scan with EPI consisted of a cardiac-gated SE sequence and (3) dual-echo proton density/T2-weighted axial oblique-scans.

8.2.3. Longitudinal network pipeline

We presented in **chapter 7** a longitudinal pipeline to reconstruct structural brain networks (Charalambous et al., 2017) and illustrated in **Fig. 7.1**. The main steps are summarised below.

Structural image pre-processing

Bias field corrected structural images were rigid-body transformed to the corresponding DWI image of the appropriate time point using BrainSuite v15b. This resulted in a structural scan of resolution 2x2x2 mm^3. T2-hyperintense lesions non-rigidly transformed to DWI space and then filled the T1-weighted images using a modality-agnostic patch-based method (Prados et al., 2016b).

Diffusion-weighted imaging pre-processing

The mean b0 image was rigid registered to the first b0 image. Then, the same rigid transformation was applied to the 61 DWI volumes. FSL v5.0.9 was used on the DWI data to correct for eddy current and head motion (Andersson and Sotiropoulos, 2016) and BrainSuite v.15b to correct for EPI distortions (Bhushan et al., 2012).

Within-subject registration for diffusion-weighted and structural images

We performed pair-wise symmetric rigid registrations to the mean b0 image to obtain the transformation matrices between each pair of images using NiftyReg (http://niftyreg.sf.net). After this, both diffusion-weighted and anatomical images from both time-points were transformed into a common half-way space. Moreover, we rotated the diffusion gradients applying the corresponding transformation matrix. Subsequent analyses were performed in this subject-specific space

Tractogram and structural brain network reconstruction

As discussed in **section 5.2.3.** (**chapter 5)** for diffusion-weighted post-processing, we used algorithms from the MRtrix3 v0.3.14 package (http://www.mrtrix.org). We used CSD to model fibre orientation distributions (Tournier et al., 2007; Tournier et al., 2004) followed by the iFOD2 algorithm (Tournier et al., 2010) to generate one tractogram per subject with 10^7 streamlines in combination with ACT framework (Smith et al., 2012) followed by SIFT2 (Smith et al., 2015b). The SIFT2 re-weighted streamlines were then assigned to the closest node as defined by GIF (Cardoso et al., 2015).GM parcellations were the network nodes whereas the networks edges were the sum of the weight of the streamlines.

Study metrics

Structural brain network metrics included edge density, global efficiency, mean local efficiency and mean clustering coefficient. These were computed from the TractoR package (Clayden et al., 2011). NABV and GM volume were computed from their corresponding time-point (baseline and follow-up) after registered in the half-way space. To perform a more regional analysis, GM volume was further divided into CGM and DGM volume. Reduction of these measures is considered as tissue atrophy. We also estimated LL as a measure of WM focal damage at baseline and follow-up.

8.2.3. Statistical analysis

This cohort is a subset of the one used in **chapter 6** for which we had longitudinal data and we followed the longitudinal pipeline as described in **chapter 7**. For these reasons, we recalculated the metrics and we reassessed the associations between network and MRI metrics at baseline. To explore possible longitudinal associations between network and MRI metrics, multiple linear regression analyses were computed in which baseline network measures were used as independent variables (one in each regression), and follow-up volumes, i.e. NABV, GM, CGM, DGM and LL were included in the model as the dependent variable (one in each regression). These models were adjusted for the baseline value of the follow-up volume being predicted. To study the ability of each baseline network metric to predict follow-up volumes in each of the MS subtypes, a categorical variable indicating MS phenotype (i.e. ‘subgroup’) and an interaction term ‘subgroup x network metric’ were added as covariates to the analyses. For all the regression models in this study, baseline age, gender, baseline disease duration and baseline LL were entered as covariates. Finally, we evaluated differences in network parameter changes over time between controls and patients.

Statistical analysis was performed using R software (https://www.r-project.org/ v3.3.0.). Data are reported as mean ± SD (two significant figures), unless otherwise stated. P-values < 0.05 were considered statistically significant.

8.3. Results

Demographic, clinical, MRI and network data from MS patients and healthy controls are summarised in **Table 8.1**.

Baseline associations between network metrics with lesion load and MRI volumes

At baseline, there was strong evidence of an association between lower edge density, global efficiency and clustering coefficient and greater LL. For each 1% decrease in edge density there was a higher LL of 2.13 ml (95% CI: 3.30 to 0.97, $p < 0.001$). In addition, for each unit decrease in global efficiency there was a higher LL of 0.025 ml (95% CI: 0.047 to 0.0040, $p = 0.037$) and finally for each unit decrease in mean clustering coefficient there was a higher LL of 0.51 ml (95% CI: 0.70 to 0.33, $p < 0.001$). We did not find any association between mean local efficiency and LL at baseline (**eTable 8.1 supplemental**).

There was also an association between edge density, mean local efficiency and mean clustering coefficient and MRI volumes. For each 1% reduction in edge density there were lower volumes of NABV by 10.84 cm^3 (95% CI: 3.49 to 18.18, $p = 0.005$), GM by 5.64 cm^3 (95% CI: 1.65 to 9.63, $p = 0.006$), CGM by 5.19 cm^3 (95% CI: 1.39 to 8.98, $p = 0.008$) and DGM by 0.45 cm^3 (95% CI: 0.21 to 0.70, $p < 0.001$). In addition, for each unit increase in mean local efficiency there was an adjusted decrease in the DGM volume of 0.0038cm^3 (95% CI: -0.0073 to -0.00024, $p = 0.036$) **(eTable 8.6 supplemental**). Moreover, for each unit decrease in mean clustering coefficient there was lower NABV of 2.35 cm^3 (95% CI: 1.09 to 3.62, $p < 0.001$), GM volume of 0.81 cm^3 (95% CI: 0.12 to 1.50, $p = 0.023$), CGM volume of 0.73 cm^3 (95% CI: 0.082 to 1.39, $p = 0.028$) and DGM volume of 0.072 cm^3 (95% CI: 0.027 to 0.12, $p = 0.002$)

(**eTable 1-5 supplemental**). The associations between mean clustering coefficient and MRI metrics were no longer significant after adjusting for LL.

Prediction of follow-up lesion load and MRI volumes from baseline network metrics

For the whole group, we found that higher baseline edge density predicted higher follow-up LL (0.18 ml, (95% CI: 0.021 to 0.35), p = 0.033) (**Table 8.2**). In addition, we detected that higher baseline global efficiency predicts lower follow-up DGM volume ($0.52x10^{-3}$ cm^3 (95% CI: $-0.99x10^{-3}$ to $-0.57x10^{-5}$), p = 0.048) after adjusting for its baseline value (**Table 8.3**). Both models were adjusted for the baseline value of the variable being predicted

We also detected different effects of baseline network metric for each of MS subtypes. We found that higher edge density at baseline predicted higher follow-up LL in RRMS subtype (0.40, 95% CI: 0.035 to 0.76, p = 0.03) only (**Table 8.2; Fig. 8.2A**). Moreover, lower baseline global efficiency (-0.0076, 95%: -0.012 to -0.0029, p = 0.0019) or mean local efficiency (-0.0068, 95% CI: -0.011 to -0.0027, p = 0.0017) predicted higher follow-up LL only in PPMS after adjusting for the baseline LL value (**Table 8.2; Fig. 8.2B, C**). Finally, in PPMS, higher baseline edge density predicts greater DGM volume at follow-up (0.075, 95% CI: 0.0019 to 0.15, p = 0.044) (**Table 8.3; Fig 8.3.**).

Network changes and differences over time in patients and controls

Network metrics did not change in patients or controls **(eTable 8.9 supplemental).** There was evidence of greater decrease in edge density over time in SPMS compared to HC (-0.78%, 95% CI: -1.63 to 0.08, p = 0.075). We also report evidence of less

decrease in mean clustering coefficient over time in PPMS compared to controls (3.01, 95% CI -0.21 to 6.23, p = 0.066). We did not find any changes over time in global or local efficiency, nor in any metrics in RRMS.

8.4. Discussion

We have evaluated the relationship between baseline network metrics and follow-up structural volumes and demonstrated that network metrics can predict reduced DGM volume and increased WM lesions.

Baseline network measures predict macroscopic visible inflammation

Firstly, we demonstrated that higher baseline edge density predicts higher follow-up LL above and beyond the presence of baseline WM lesions. Edge density is denoted as the proportion of existing edges divided by the total possible number of edges reflecting thus the overall network connectivity (Kaiser, 2011). Our results indicated that the more connected the network is, the greater the lesion volume after two years becomes. This could mean that a more preserved connectivity at baseline indicates a higher biological cost which makes the network more vulnerable to additional pathology such as pathogenic processes including astrogliosis, oligodendrocyte loss and infiltration by macrophages/microglia (Bogdan et al., 2013), contributing to increased WM damage over a short period of time. The fact that this behaviour is not detected in progressive diseases suggests that edge density could serve as an early marker of future tissue damage.

Moreover, our findings demonstrated that in the primary progressive group alone lower baseline efficiency predicts higher lesion volume after adjusting for its baseline value. WM lesions are likely to affect the information transfer capacity within a network and this could explain the decreased overall brain efficiency as the lesion volume increases, as reported in our baseline analysis of this study and in previous work (Shu et al., 2011). Interestingly, our analysis indicates that the greater the baseline lesion volume is, the greater the reduction of network efficiency, which in turn

predicts higher lesion volume after two years above and beyond of baseline focal damage (i.e. lesions). Although the exact mechanism underlying this observation remains to be elucidated, we can hypothesise that network efficiency metrics are sensitive to microstructural changes in the normal appearing WM such as reduced cross-sectional area (Smith et al., 2015a) that will contribute to further tissue damage. A previous longitudinal MTR study demonstrated that anomalies detected in the normal appearing WM were predictive of tissue loss in visual and motor cortex, supporting partially the results presented here. To further elaborate on our findings, we could hypothesise that primary demyelination causes reductions in neuronal tract density, although the reverse could be possible, in turn reflecting reduced network efficiency. Future investigations considering myelin density and with longer longitudinal studies could validate or confute this hypothesis.

Baseline network measures predict tissue loss

Our findings show interesting results with respect to the DGM volume loss. Higher mean local efficiency is associated with smaller DGM volume at baseline. Given that DGM atrophy is more strongly associated with cognitive impairment as previously reported (Debernard et al., 2015) and in **chapter 6** of this thesis, it is possible that the increase in local information flow reflects some potential mechanisms to compensate for the tissue loss. However, we speculate that these potentially 'adaptive' mechanisms over time may cause increased atrophy as we demonstrated that higher baseline global efficiency predicts greater atrophy in the DGM volume after two years when the baseline DGM volume value is considered. Although this is not the first time network reorganization has been reported in structural (Fleischer et al., 2017) or in functional (Rocca et al., 2016) connectivity studies, this is the first study that investigates the predictive nature of diffusion-derived network metrics in MS.

Furthermore, we demonstrate that primary progressive patients with lower network connectivity at baseline will have greater DGM atrophy after two years. Given that we also presented here that higher baseline connectivity predicts higher visible damage at follow-up, we believe that the temporal-related occurrence of inflammation and neurodegeneration are captured by our analyses. For example, a patient with MS and shorter disease duration may have high connectivity that predicts more lesion volume at follow-up, while longer disease duration suggests less connectivity due to the progressive loss of connections predicting neurodegeneration. In fact, lower connectivity predicts greater tissue loss in mild cognitive impairment patients (Nir et al., 2015) justifying in part our results; however, due to the small sample size in our study this explanation remains speculative. Hence, these findings need to be confirmed in other cohorts with longer follow-up data and if true they could demonstrate that edge density in particularly might serve as predictor for disease progression.

Our baseline analysis also shows that lower mean clustering coefficient is associated with reduced brain tissue. Mean clustering coefficient is a topological metric and reduced values reflect reduced brain segregation (Rubinov and Sporns, 2010). Interestingly, when we adjusted for LL in our analysis, we found that the association between clustering coefficient and brain tissue volume was no longer significant; neither the mean clustering coefficient nor the LL variables were associated with brain volume. This can be explained by the fact that the two predictors are highly correlated ($r = 0.6$), which means that they both “compete” with each other in explaining the variance in the data, therefore losing their significance. Reduced clustering coefficient is thought to reflect more random structural networks. Therefore, the fact that reduced mean clustering coefficient is associated with greater lesion

volume supports the disconnection mechanism hypothesis proposed elsewhere (Dineen et al., 2009).

Further considerations of the present study

We detected evidence of differential rates of change in edge density and mean clustering coefficient between MS subtypes. This could provide some useful insights in whole brain connectivity properties and longitudinal development of brain damage, that future investigations can be built upon: A) The two year-window might be a short period to capture significant network alterations. Therefore, longer interval scans might be desirable. B) Our cohort has a relatively long disease duration (mean ± SD; 17 ± 11 years) which means that it is likely that any network changes might have occurred at earlier stages of the disease. In fact, Tur et al. (2016) demonstrated that optic radiations diffusion-derived metrics decreased over time in patients after optic neuritis after one-year follow-up. C) The findings from Tur et al. (2016) suggest that a more targeted subnetwork derived metrics might be more sensitive in capturing longitudinal changes. Taking into consideration a recent study demonstrating that a SDMT score is sensitive to cognitive changes after one year in MS (Lopez-Gongora et al., 2015), we could speculate that subnetwork-metrics that include for example areas from the DGM nuclei could be good candidate to validate this hypothesis.

This study has several limitations. The limitations associated with the pipeline itself have been addressed in **chapters 5-7**. In addition, we appreciate our small sample size, primarily in the primary progressive group (n=14). However, we inspected all regression models for outliers and influencers, with negative results. Additionally, we evaluated whether network metrics could predict tissue damage longitudinally. While this is important for disease stratification, it is also important to help evaluate whether those metrics can predict the conversion of prodromal or mild diseased types

into more progressive stages. A similar approach was adopted in a study of small vessel disease patients which demonstrated that subjects who converted to dementia had lower baseline global efficiency (Tuladhar et al., 2016). Early MS subjects should be studied to complement our current data to investigate whether the network metrics presented in the current study are predictive of MS type conversion. Finally, we used global network metrics to predict coarse anatomical volumetric changes. Steenwijk et al. (2016) recently demonstrated that cortical atrophy does not equally affect all brain regions which might indicate that neurodegeneration might have a predilection for particular areas. This in turn suggests that prediction of more regional changes would be of future interest for assessing its sensitivity to disease progression.

8.5. Conclusion

In conclusion, our study provides evidence of longitudinal damage that can be predicted by baseline network metrics and it is independent of the baseline visible damage and the extent of the baseline tissue loss. Here we show for the first time that that diffusion-based network measures can be novel predictors for MS progression.

The network metrics used in **chapter 6** and **8** were derived from the brain as a whole. However, considering the findings published by Tur et al. (2016) and by Steenwijk et al. (2016) it becomes apparent that targeted subnetwork analysis might be more sensitive in capturing longitudinal network changes. Therefore, decomposing the network into subnetworks may well be a valuable strategy to obtain further insights into subnetwork organisation and how this is affected in pathology. The following chapter will cover a novel, data-driven decomposition approach and its application in MS.

BASELINE					
	HC (n=12)	**Whole MS (n=61)**	**RRMS (n=27)**	**PPMS (n=14)**	**SPMS (n=20)**
Age, years	36 ± 13	47 ± 11	41 ± 11	50 ± 10	54 ± 07
Gender (M/F)	06/06	21/41	05/22	08/06	08/12
Interval from baseline, years	1.83 ± 0.55	1.84 ± 0.55	1.80 ± 0.52	2.24 ± 0.66	1.62 ± 0.33
Disease duration, years	-	17 ± 11	12 ± 9	13 ± 8	26 ± 10
EDSS, median	-	5.00 (1-6.5)	2.00 (1-6)	6.00 (3-6.5)	6.50 (4-8.5)
NABV, cm^3	1186 ± 107	1040 ± 127	1060 ± 144	1081 ± 99	984 ± 103
GM, cm^3	699 ± 60	626 ± 68	637 ± 76	645 ± 57	599 ± 58
CGM, cm^3	659 ± 56	592 ± 65	602 ± 73	609 ± 55	566 ± 55
DGM, cm^3	40 ± 3	34 ± 4	35 ± 5	36 ± 3	33 ± 4
NAWM, cm^3	487 ± 52	414 ± 62	423 ± 72	436 ± 46	386 ± 48
LL, ml	-	17.42 ± 17.98	17.49 ± 20.41	15.86 ± 17.65	18.42 ± 15.31
Edge density, %	91.15 ± 2.37	90.66 ± 3.62	90.76 ± 4.15	91.15 ± 3.29	90.18 ± 3.16
Global efficiency	3955 ± 118	3894 ± 226	3952 ± 156	3880 ± 252	3827 ± 274
Mean local efficiency	4071 ± 139	4000 ± 261	4061 ± 193	3979 ± 285	3934 ± 314
Mean clustering coefficient	249 ± 10	230 ± 21	235 ± 19	231 ± 20	222 ± 21

Table 8.1. Baseline characteristics of the participants

Abbreviations: HC = healthy controls; MS = multiple sclerosis; RRMS = relapsing-remitting MS; PPMS = primary progressive MS; SPMS = secondary progressive MS; NABV = normal appearing brain volume; GM = grey matter; CGM = cortical grey matter; DGM = deep grey matter; NAWM = normal appearing white matter; LL = Lesion load

WHOLE MS GROUP			
Follow-up lesion load (ml)			
Main baseline predictors	**Regression Coefficient**	**95% CI**	**P-value**
Edge density	0.18	0.02 – 0.35	**0.033**
Global efficiency	-0.00042	-0.0031 – 0.0022	0.749
Local Efficiency	-0.00061	-0.0029 – 0.0016	0.586
Clustering coefficient	0.017	-0.018 – 0.053	0.289
MS SUBTYPES			
Edge density			
RRMS	0.40	0.035 – 0.76	**0.032**
PPMS	0.28	-0.085 – 0.64	0.130
SPMS	-0.12	-0.44 – 0.20	0.454
Global efficiency			
RRMS	0.0013	-0.0040 – 0.0065	0.624
PPMS	-0.0076	-0.012 – -0.0029	**0.0019**
SPMS	0.0022	-0.0015 – 0.0060	0.246
Local Efficiency			
RRMS	-0.00019	-0.0044 – 0.0040	0.93
PPMS	-0.0068	-0.011 – -0.0027	**0.0017**
SPMS	0.0022	-0.0011 – 0.0055	0.18
Clustering coefficient			
RRMS	0.036	-0.014 – 0.087	0.158
PPMS	-0.034	-0.099 – 0.032	0.308
SPMS	0.017	-0.039 – 0.072	0.55

Table 8.2. Linear regression of baseline associations between baseline metrics and follow-up lesion load in multiple sclerosis group and subtypes

Models are adjusted for baseline age, baseline lesion load and gender

Data reported as two significant figures

Abbreviations: MS = multiple sclerosis; RRMS = relapsing-remitting MS; PPMS = primary progressive multiple sclerosis MS; SPMS = secondary progressive MS; CI = confidence interval

WHOLE MS GROUP			
Follow-up deep grey matter volume (cm^3)			
Main baseline predictors	**Regression Coefficient**	**95% CI**	**P-value**
Edge density	-0.012	-0.050 – 0.024	0.487
Global efficiency	-0.00052	-0.00099 – -0.0000057	**0.048**
Local Efficiency	-0.00041	-0.00085 – -0.000025	0.064
Clustering coefficient	0.0045	-0.010 – 0.0011	0.109
MS SUBTYPES			
Edge density			
RRMS	-0.024	-0.072 – 0.022	0.297
PPMS	0.075	0.0019 – 0.15	**0.044**
SPMS	-0.040	-0.11 – 0.026	0.229
Global efficiency			
RRMS	-0.000033	-0.0012 – 0.0011	0.953
PPMS	-0.00064	-0.0016 – 0.00037	0.212
SPMS	-0.00018	-0.00099 – 0.00064	0.666
Local Efficiency			
RRMS	0.000071	-0.00083 – 0.00098	0.875
PPMS	-0.00061	-0.0015 – 0.00028	0.172
SPMS	-0.00010	-0.00081 – 0.00061	0.774
Clustering coefficient			
RRMS	-0.0015	-0.012 – 0.0085	0.753
PPMS	0.0036	-0.0092 – 0.017	0.576
SPMS	-0.0084	-0.019 – 0.0023	0.123

Table 8.3. Linear regression of baseline associations between baseline metrics and follow-up deep grey matter volume in multiple sclerosis group and subtypes

Models are adjusted for baseline age, baseline lesion load, baseline deep grey matter volume and gender

Data reported as two significant figures

Abbreviations: MS = multiple sclerosis; RRMS = relapsing-remitting MS; PPMS = primary progressive multiple sclerosis MS; SPMS = secondary progressive MS; CI = confidence interval

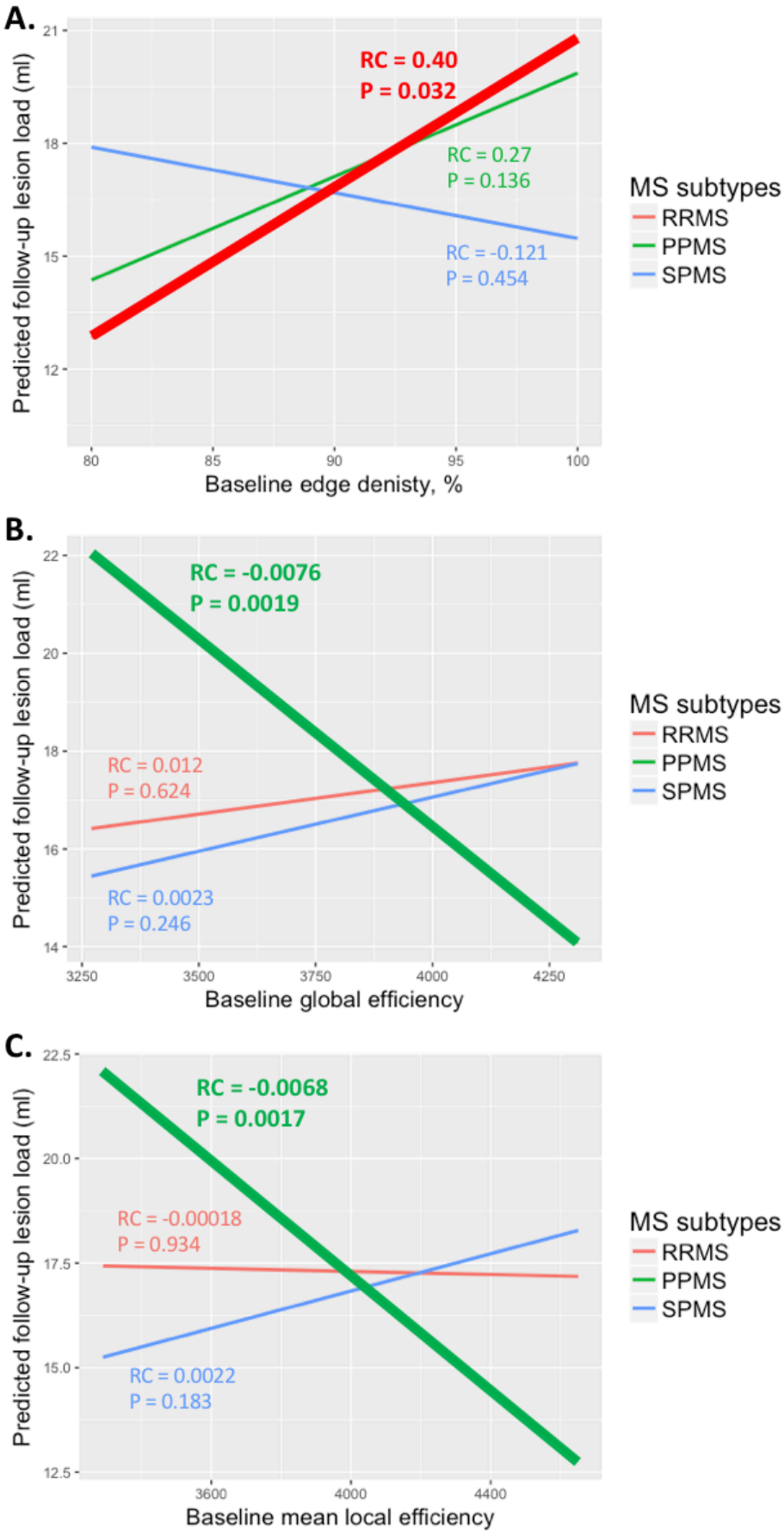
A.
Predicted follow-up lesion load (ml)
21
18
15
12
80
85
90
95
100
Baseline edge denisty, %
RC = 0.40
P = 0.032
RC = 0.27
P = 0.136
RC = -0.121
P = 0.454
MS subtypes
RRMS
PPMS
SPMS
B.
Predicted follow-up lesion load (ml)
22
20
18
16
14
3250
3500
3750
4000
4250
Baseline global efficiency
RC = -0.0076
P = 0.0019
RC = 0.012
P = 0.624
RC = 0.0023
P = 0.246
MS subtypes
RRMS
PPMS
SPMS
C.
Predicted follow-up lesion load (ml)
22.5
20.0
17.5
15.0
12.5
3600
4000
4400
Baseline mean local efficiency
RC = -0.0068
P = 0.0017
RC = -0.00018
P = 0.934
RC = 0.0022
P = 0.183
MS subtypes
RRMS
PPMS
SPMS

Figure 8.1. Prediction of follow-up lesion load form baseline network metrics

The graph demonstrates the prediction of follow-up lesion load from baseline edge density **(A)**, global efficiency **(B)** and mean local efficiency **(C)**. The thick lines represent significant association.

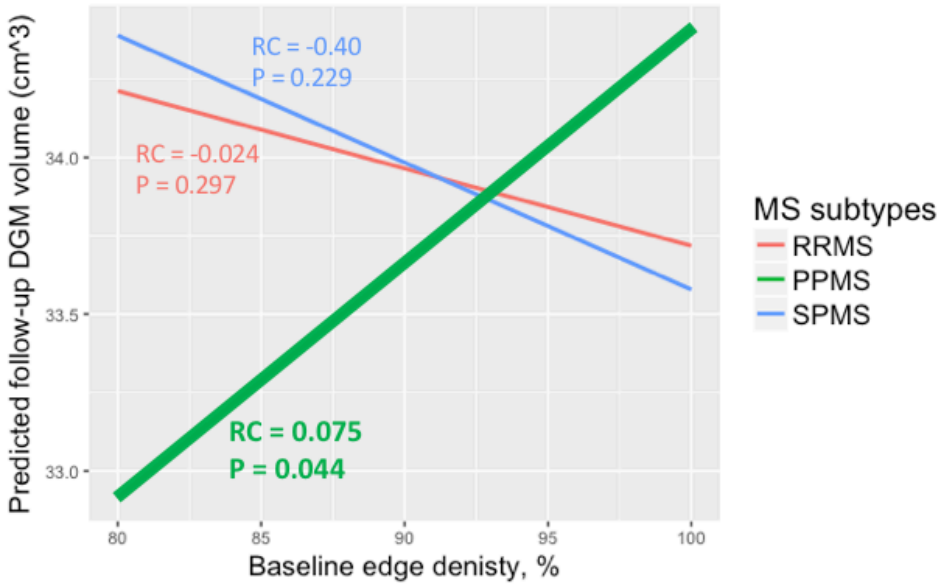

Figure 8.2. Prediction of follow-up deep grey matter volume from baseline edge density

The thick line represents significant association.

Appendix B Supplemental results

WHOLE MS GROUP			
Baseline lesion load (ml)			
Main predictors	**Regression Coefficient**	**95% CI**	**P-value**
Edge density	-2.130	-3.30 – -0.97	**<0.001**
Global efficiency	-0.025	-0.047 – -0.0040	**0.037**
Local Efficiency	-0.014	-0.03 – 0.0045	0.132
Clustering coefficient	-0.510	-0.70 – -0.33	**<0.001**
MS SUBTYPES			
Edge density			
RRMS	-2.857	-4.45 – -1.31	**<0.001**
PPMS	0.1032	-2.77 – 2.98	0.94
SPMS	-2.431	-4.91 – 0.048	0.054
Global efficiency			
RRMS	-0.029	-0.075 – 0.016	0.20
PPMS	-0.042	-0.082 – -0.0026	**0.037**
SPMS	-0.012	-0.045 – 0.021	0.47
Mean local Efficiency			
RRMS	-0.0040	-0.042 – 0.034	0.83
PPMS	-0.035	-0.071 – 0.00051	0.053
SPMS	-0.0065	-0.036 – 0.023	0.66
Mean clustering coefficient			
RRMS	-0.604	-0.91 – -0.30	**<0.001**
PPMS	-0.561	-0.98 – -0.14	**0.0096**
SPMS	-0.547	-0.89 – -0.21	**0.0023**

eTable 8.1: Linear regression of baseline associations between baseline metrics and baseline and baseline lesion load in multiple sclerosis group and subtypes.

Models are adjusted for baseline age, baseline lesion load and gender

Data reported as two significant figures

Abbreviations: MS = multiple sclerosis; RRMS = relapsing-remitting MS; PPMS = primary progressive multiple sclerosis MS; SPMS = secondary progressive MS; CI = confidence interval

WHOLE MS GROUP			
Baseline normal appearing brain volume (cm^3)			
Main predictors	**Regression Coefficient**	**95% CI**	**P-value**
Edge density	10.84	3.49 – 18.18	**0.005**
Global efficiency	-0.039	-0.16 - 0.086	0.536
Local Efficiency	-0.052	-0.16 – 0.053	0.324
Clustering coefficient [a]	2.35	1.09 – 3.62	**<0.001**
MS SUBTYPES			
Edge density			
RRMS	11.38	1.77 – 20.99	**0.021**
PPMS	2.86	-12.81 – 18.58	0.714
SPMS	11.00	-0.30 – 25.03	0.122
Global efficiency			
RRMS	-0.0092	-0.25 – 0.23	0.943
PPMS	-0.070	0.29 – 0.14	0.522
SPMS	-0.074	-0.25 – 0.10	0.403
Mean local Efficiency			
RRMS	-0.056	-0.25 – 0.14	0.565
PPMS	-0.053	-0.24 – 0.14	0.583
SPMS	-0.070	-0.22 – 0.084	0.367
Mean clustering coefficient			
RRMS	1.72	-0.48 – 3.93	0.122
PPMS	0.093	-2.74 – 2.92	0.947
SPMS	0.64	1.73 – 3.02	0.588

eTable 8.2: Linear regression of baseline associations between baseline network metrics and baseline normal appearing brain volume in multiple sclerosis group and subtypes.

Models are adjusted for baseline age, baseline lesion load and gender

Data reported as two significant figures

[a] after adjusting for baseline lesion load the association is no longer significant

Abbreviations: MS = multiple sclerosis; RRMS = relapsing-remitting MS; PPMS = primary progressive multiple sclerosis MS; SPMS = secondary progressive MS; CI = confidence interval

WHOLE MS GROUP			
Baseline grey matter volume (cm^3)			
Main predictors	**Regression Coefficient**	**95% CI**	**P-value**
Edge density	6.79	3.19 – 10.40	**<0.001**
Global efficiency	-0.035	-0.10 – 0.032	0.295
Local Efficiency	-0.039	-0.096 – 0.017	0.169
Clustering coefficient [a]	0.81	0.12 – 1.50	**0.022**
MS SUBTYPES			
Edge density			
RRMS	6.08	0.76 – 11.40	**0.026**
PPMS	1.27	-7.43 – 9.93	0.774
SPMS	6.57	-1.19 – 14.33	0.095
Global efficiency			
RRMS	-0.019	-0.15 – 0.12	0.775
PPMS	-0.039	-0.016 – 0.082	0.523
SPMS	-0.058	-0.16 – 0.039	0.234
Mean local Efficiency			
RRMS	-0.038	-0.15 – 0.07	0.453
PPMS	-0.029	-0.13 – 0.077	0.589
SPMS	-0.054	-0.13 – 0.031	0.205
Mean clustering coefficient			
RRMS	0.59	-0.064 – 1.83	0.339
PPMS	-0.19	-1.78 – 1.39	0.806
SPMS	-0.0055	-1.33 – 1.33	0.993

eTable 8.3: Linear regression of baseline associations between baseline network metrics and baseline grey matter volume in multiple sclerosis group and subtypes.

Models are adjusted for baseline age, baseline lesion load and gender

Data reported as two significant figures

[a] after adjusting for baseline lesion load the association is no longer significant

Abbreviations: MS = multiple sclerosis; RRMS = relapsing-remitting MS; PPMS = primary progressive multiple sclerosis MS; SPMS = secondary progressive MS; CI = confidence interval

WHOLE MS GROUP			
Baseline cortical grey matter volume (cm^3)			
Main predictors	**Regression Coefficient**	**95% CI**	**P-value**
Edge density	6.21	2.78 – 9.63	**<0.001**
Global efficiency	-0.032	-0.0096 – 0.032	0.320
Local Efficiency	-0.035	-0.089 – 0.018	0.190
Clustering coefficient [a]	0.73	0.082 – 1.39	**0.028**
MS SUBTYPES			
Edge density			
RRMS	5.65	0.58 – 10.72	**0.029**
PPMS	0.95	-7.33 – 9.23	0.819
SPMS	6.09	-1.31 – 13.49	0.105
Global efficiency			
RRMS	-0.015	-0.14 – 0.11	0.806
PPMS	-0.034	-0.15 – 0.080	0.551
SPMS	-0.054	-0.15 – 0.039	0.247
Mean local Efficiency			
RRMS	-0.035	-0.14 – 0.066	0.484
PPMS	-0.025	-0.12 – 0.076	0.623
SPMS	-0.050	-0.13 – 0.030	0.217
Mean clustering coefficient			
RRMS	0.55	-0.62 – 1.72	0.345
PPMS	-0.16	1.67 – 1.34	0.827
SPMS	-0.0097	-1.27 – 1.25	0.988

eTable 8.4: Linear regression of baseline associations between baseline network metrics and baseline cortical grey matter volume in multiple sclerosis group and subtypes.

Models are adjusted for baseline age, baseline lesion load and gender

Data reported as two significant figures

[a] after adjusting for baseline lesion load the association is no longer significant

Abbreviations: MS = multiple sclerosis; RRMS = relapsing-remitting MS; PPMS = primary progressive multiple sclerosis MS; SPMS = secondary progressive MS; CI = confidence interval

WHOLE MS GROUP			
Baseline deep grey matter volume (cm^3)			
Main predictors	**Regression Coefficient**	**95% CI**	**P-value**
Edge density	0.45	0.21 – 0.69	**<0.001**
Global efficiency	-0.0035	-0.0077 – 0.00071	0.101
Local Efficiency	-0.0038	-0.0073 – -0.00024	**0.036**
Clustering coefficient [a]	0.072	0.027 – 0.12	**0.002**
MS SUBTYPES			
Edge density			
RRMS	0.43	0.11 – 0.75	**0.009**
PPMS	0.30	-0.22 – 0.82	0.254
SPMS	0.48	0.013 – 0.94	**0.044**
Global efficiency			
RRMS	-0.0035	-0.012 – 0.0047	0.394
PPMS	-0.0044	-0.012 – 0.0030	0.233
SPMS	-0.0043	-0.010 – 0.0015	0.145
Mean local Efficiency			
RRMS	-0.0045	-0.011 – 0.0019	0.162
PPMS	-0.0038	-0.010 – 0.0026	0.233
SPMS	-0.0039	-0.0091 – 0.0011	0.134
Mean clustering coefficient			
RRMS	0.042	-0.033 – 0.112	0.277
PPMS	-0.029	-0.13 – 0.068	0.546
SPMS	0.0041	-0.078 – 0.086	0.913

eTable 8.5: Linear regression of baseline associations between baseline metrics and baseline deep grey matter volume in multiple sclerosis group and subtypes.

Models are adjusted for baseline age, baseline lesion load and gender

Data reported as two significant figures

[a] after adjusting for baseline lesion load the association is no longer significant

Abbreviations: MS = multiple sclerosis; RRMS = relapsing-remitting MS; PPMS = primary progressive multiple sclerosis MS; SPMS = secondary progressive MS; CI = confidence interval

WHOLE MS GROUP			
Follow-up normal appearing brain volume (cm^3)			
Main baseline predictors	**Regression Coefficient**	**95% CI**	**P-value**
Edge density	0.21	-0.43 – 0.84	0.524
Global efficiency	0.00057	-0.0089 – 0.010	0.904
Local Efficiency	0.00019	-0.0081 – 0.0085	0.962
Clustering coefficient	0.026	-0.083 – 0.13	0.633
MS SUBTYPES			
Edge density			
RRMS	0.018	-0.92 – 0.96	0.969
PPMS	1.21	-0.25 – 2.68	0.103
SPMS	-0.37	-1.71 – 0.97	0.578
Global efficiency			
RRMS	0.00090	-0.021 – 0.023	0.935
PPMS	-0.0087	-0.028 – 0.011	0.382
SPMS	0.0065	-0.0095 – 0.022	0.421
Local Efficiency			
RRMS	0.00052	-0.017 – 0.018	0.953
PPMS	-0.0087	-0.026 – 0.0087	0.321
SPMS	0.0059	-0.0080 – 0.020	0.397
Clustering coefficient			
RRMS	0.0026	-0.20 – 0.21	0.979
PPMS	0.29	-0.12 – 0.39	0.293
SPMS	0.0049	-0.21 – 0.22	0.964

eTable 8.7: Linear regression of baseline associations between baseline network metrics and follow-up normal appearing brain volume in multiple sclerosis group and subtypes.

Models are adjusted for baseline normal appearing brain volume, baseline age, baseline lesion load and gender

Data reported as two significant figures

Abbreviations: MS = multiple sclerosis; RRMS = relapsing-remitting MS; PPMS = primary progressive multiple sclerosis MS; SPMS = secondary progressive MS; CI = confidence interval

WHOLE MS GROUP			
Follow-up grey matter volume (cm^3)			
Main baseline predictors	**Regression Coefficient**	**95% CI**	**P-value**
Edge density	0.28	-0.22 – 0.80	0.262
Global efficiency	0.00043	-0.0074 – 0.0083	0.912
Local Efficiency	-0.00015	-0.0070 – 0.0067	0.965
Clustering coefficient	0.052	-0.034 – 0.13	0.232
MS SUBTYPES			
Edge density			
RRMS	0.17	-0.56 – 0.91	0.633
PPMS	0.87	-0.27 – 2.02	0.132
SPMS	-0.66	-1.71 – 0.39	0.214
Global efficiency			
RRMS	0.00075	-0.016 – 0.018	0.931
PPMS	-0.0063	-0.022 – 0.0092	0.415
SPMS	0.0077	-0.0049 – 0.020	0.227
Local Efficiency			
RRMS	-0.00058	-0.014 – 0.013	0.934
PPMS	-0.0057	-0.019 – 0.0079	0.402
SPMS	0.0072	-0.0038 – 0.018	0.194
Clustering coefficient			
RRMS	0.064	-0.091 – 0.22	0.410
PPMS	0.18	-0.012 – 0.38	0.064
SPMS	0.015	-0.15 – 0.182	0.855

eTable 8.6: Linear regression of baseline associations between baseline network metrics and follow-up grey matter volume in multiple sclerosis group and subtypes.

Models are adjusted for baseline grey matter volume, baseline age, baseline lesion load and gender

Data reported as two significant figures

Abbreviations: MS = multiple sclerosis; RRMS = relapsing-remitting MS; PPMS = primary progressive multiple sclerosis MS; SPMS = secondary progressive MS; CI = confidence interval

WHOLE MS GROUP			
Follow-up cortical grey matter volume (cm^3)			
Main baseline predictors	**Regression Coefficient**	**95% CI**	**P-value**
Edge density	0.30	-0.19 – 0.78	0.229
Global efficiency	0.00090	-0.0067 – 0.0085	0.813
Local Efficiency	0.00021	-0.0064 – 0.00684	0.950
Clustering coefficient	0.057	-0.026 – 0.14	0.173
MS SUBTYPES			
Edge density			
RRMS	0.21	-0.51 – 0.92	0.563
PPMS	0.80	-0.31 – 1.91	0.154
SPMS	-0.61	-1.63 – 0.40	0.233
Global efficiency			
RRMS	0.00072	-0.016 – 0.017	0.932
PPMS	-0.0058	-0.021 – 0.0092	0.441
SPMS	0.0078	-0.0044 – 0.020	0.206
Local Efficiency			
RRMS	-0.00073	-0.014 – 0.013	0.914
PPMS	-0.0052	-0.019 – 0.0080	0.432
SPMS	0.0073	-0.0034 – 0.018	0.177
Clustering coefficient			
RRMS	0.067	-0.084 0.21	0.379
PPMS	0.18	-0.0091 – 0.38	0.061
SPMS	0.024	-0.14 – 0.19	0.769

eTable 8.8: Linear regression of baseline associations between baseline network metrics and follow-up cortical grey matter volume in multiple sclerosis group and subtypes.

Models are adjusted for baseline cortical grey matter volume, baseline age, baseline lesion load and gender

Data reported as two significant figures

Abbreviations: MS = multiple sclerosis; RRMS = relapsing-remitting MS; PPMS = primary progressive multiple sclerosis MS; SPMS = secondary progressive MS; CI = confidence interval

ANNUALISED CHANGES					
	HC (n=12)	**Whole MS (n=61)**	**RRMS (n=27)**	**PPMS (n=14)**	**SPMS (n=20)**
Edge density, %	-0.07 ± 1.18	-0.50 ± 1.22	-0.43 ± 1.05	-0.14 ± 0.92	-0.86 ± 1.50
Global efficiency	31.68 ± 54.78	7.55 ± 53.23	7.25 ± 55.15	20.27 ± 29.75	-0.95 ± 63.12
Mean local efficiency	36.17 ± 60.69	16.30 ± 59.55	13.12 ± 61.31	24.02 ± 38.91	15.17 ± 70.43
Mean clustering coefficient	-3.22 ± 6.21	-1.32 ± 4.22	-1.52 ± 4.90	-0.23 ± 1.92	-1.80 ± 4.75

eTable 8.9: Annualised changes of network metrics.

Abbreviations: MS = multiple sclerosis RRMS = relapsing-remitting MS; PPMS = primary progressive multiple sclerosis MS; SPMS = secondary progressive MS;

Data (mean ± SD) reported as two significant figures

Bibliography

Andersson JL and Sotiropoulos SN. (2016) An integrated approach to correction for off-resonance effects and subject movement in diffusion MR imaging. *Neuroimage* 125: 1063-1078.

Bhushan C, Haldar JP, Joshi AA, et al. (2012) Correcting Susceptibility-Induced Distortion in Diffusion-Weighted MRI using Constrained Nonrigid Registration. *Signal Inf Process Assoc Annu Summit Conf APSIPA Asia Pac* 2012.

Bodini B, Chard D, Altmann DR, et al. (2016) White and gray matter damage in primary progressive MS: The chicken or the egg? *Neurology* 86: 170-176.

Bogdan F, Popescu G, Pirko I, et al. (2013) Pathology of Multiple Sclerosis: Where Do We Stand? *Continuum*.

Cardoso MJ, Modat M, Wolz R, et al. (2015) Geodesic Information Flows: Spatially-Variant Graphs and Their Application to Segmentation and Fusion. *IEEE Trans Med Imaging* 34: 1976-1988.

Charalambous T, Prados F, Tur C, et al. (2017) Longitudinal analysis framework of DWI data for reconstructing structural brain networks with application to Multiple Sclerosis. *Computational Diffusion MRI*.

Clayden J, Maniega SM, Stokey AJ, et al. (2011) TractoR: Magnetic Resonance Imaging and Tractography with R. *JSS*.

Debernard L, Melzer TR, Alla S, et al. (2015) Deep grey matter MRI abnormalities and cognitive function in relapsing-remitting multiple sclerosis. *Psychiatry Res* 234: 352-361.

Dineen RA, Vilisaar J, Hlinka J, et al. (2009) Disconnection as a mechanism for cognitive dysfunction in multiple sclerosis. *Brain* 132: 239-249.

Fisniku LK, Brex PA, Altmann DR, et al. (2008a) Disability and T2 MRI lesions: a 20-year follow-up of patients with relapse onset of multiple sclerosis. *Brain* 131: 808-817.

Fleischer F, Gröger A, Koirala N, et al. (2017) Increased structural white and grey matter network connectivity compensates for functional decline in early multiple sclerosis. *Multiple Sclerosis Journal* 23: 432–441.

Kaiser M. (2011) A tutorial in connectome analysis: topological and spatial features of brain networks. *Neuroimage* 57: 892-907.

Llufriu S, Martinez-Heras E, Solana E, et al. (2017) Structural networks involved in attention and executive functions in multiple sclerosis. *Neuroimage Clin* 13: 288-296.

Lopez-Gongora M, Querol L and Escartin A. (2015) A one-year follow-up study of the Symbol Digit Modalities Test (SDMT) and the Paced Auditory Serial Addition Test (PASAT) in relapsing-remitting multiple sclerosis: an appraisal of comparative longitudinal sensitivity. *BMC Neurol* 15: 40.

Nir TM, Jahanshad N, Toga AW, et al. (2015) Connectivity network measures predict volumetric atrophy in mild cognitive impairment. *Neurobiol Aging* 36 Suppl 1: S113-120.

Prados F, Cardoso MJ, Kanber B, et al. (2016b) A multi-time-point modality-agnostic patch-based method for lesion filling in multiple sclerosis. *Neuroimage* 139: 376-384.

Rocca MA, Valsasina P, Meani A, et al. (2016) Impaired functional integration in multiple sclerosis: a graph theory study. *Brain Struct Funct* 221: 115-131.

Rubinov M and Sporns O. (2010) Complex network measures of brain connectivity: uses and interpretations. *Neuroimage* 52: 1059-1069.
Shu N, Liu Y, Li K, et al. (2011) Diffusion tensor tractography reveals disrupted topological efficiency in white matter structural networks in multiple sclerosis. *Cereb Cortex* 21: 2565-2577.
Smith RE, Tournier JD, Calamante F, et al. (2012) Anatomically-constrained tractography: improved diffusion MRI streamlines tractography through effective use of anatomical information. *Neuroimage* 62: 1924-1938.
Smith RE, Tournier JD, Calamante F, et al. (2015a) The effects of SIFT on the reproducibility and biological accuracy of the structural connectome. *Neuroimage* 104: 253-265.
Smith RE, Tournier JD, Calamante F, et al. (2015b) SIFT2: Enabling dense quantitative assessment of brain white matter connectivity using streamlines tractography. *Neuroimage* 119: 338-351.
Steenwijk MD, Geurts JJ, Daams M, et al. (2016) Cortical atrophy patterns in multiple sclerosis are non-random and clinically relevant. *Brain* 139: 115-126.
Tournier JD, Calamante F and Connelly A. (2007) Robust determination of the fibre orientation distribution in diffusion MRI: non-negativity constrained super-resolved spherical deconvolution. *Neuroimage* 35: 1459-1472.
Tournier JD, Calamante F and Connelly A. (2010) Improved probabilistic streamlines tractography by 2nd order integration over fibre orientation distributions. *Joint Annual Meeting ISMRM-ESMRMB*.
Tournier JD, Calamante F, Gadian DG, et al. (2004) Direct estimation of the fiber orientation density function from diffusion-weighted MRI data using spherical deconvolution. *Neuroimage* 23: 1176-1185.
Tuladhar AM, van Uden IWM, Loes C.A. Rutten-Jacobs LCA, et al. (2016) Structural network efficiency predicts conversion to dementia. *Neurology* 86: 1112-1119.
Tur C, Goodkin O, Altmann DR, et al. (2016) Longitudinal evidence for anterograde trans-synaptic degeneration after optic neuritis. *Brain* 139: 816-828.

Chapter 9

9. Distinct patterns of principal network organisation in multiple sclerosis subtypes

Summary

In this chapter we sought to investigate principal network organization in healthy controls and multiple sclerosis patients. Structural brain networks were reconstructed from diffusion-weighted magnetic resonance images in 51 healthy controls and 122 patients consisting of 58 relapsing-remitting, 28 primary progressive and 36 secondary progressive. We then calculated and compared the first and second principal networks from the derived mean connectivity matrix from healthy controls and for each of the MS phenotypes. We also estimated and compared the subject-wise brain regions that exhibited high connectivity (hubs) in each group. The results presented here show preserved hub organization in all multiple sclerosis subtypes. However, there was reduced strength in some hubs in multiple sclerosis and the number of affected regions increased in more severe phenotypes. In healthy controls, the first principal network consisted of 10 fully-connected hubs and this organization was preserved in relapsing-remitting and primary progressive patients, while in secondary progressive group a loss of the right thalamo-cortical connections from this network was detected. The second principal network consisted of 10 hub regions with strong interhemispheric connections in healthy controls. In multiple sclerosis patients, this network did not include the right putamen compared to healthy controls, while secondary progressive patients had an additional reduction of the right thalamo-cortical connections. This exploratory analysis suggests that this technique may provide insights into the pattern

of progressive reduction of connectivity in more severe multiple sclerosis phenotypes and has potential utility as disease biomarkers.

Scientific contribution

The results presented in this chapter have been presented as a traditional poster: **Differential topological organisation of brain networks in multiple sclerosis.** *OHBM (2018).* Singapore. The manuscript is in preparation to be submitted in peer-reviewed *Multiple Sclerosis Journal*.

9.1. Introduction

As discussed in **chapter 4**, network-based approaches may offer new and useful insights into MS specific processes. For example, network studies have demonstrated the existence of a number regions that receive higher number of connections, known as network hubs, and that these are affected in MS (Shu et al., 2011). It has also been proposed that hub nodes have the tendency to be more densely connected with each other rather than with nodes that have lower number of connections (van den Heuvel and Sporns, 2011) and in fact such 'rich-club' organisation seems to be affected in PPMS (Stellmann et al., 2017). Recently, a data-driven framework has been proposed for network decomposition into stable, meaningful and reproducible subnetworks with strong internal connectivity (Clayden et al., 2013). Briefly, applying the principal components analysis-based technique, the full connectivity matrix is decomposed into partial connectivity matrices through a linear decomposition. Effectively, the full connectivity matrix is the sum of these component matrices, namely principal networks. **Fig. 9.1.** serves as an example of whole network decomposition to its principal networks. Although these principal networks are considered topological features depicting regions that are highly interconnected, their relevance to MS remains unknown. In this chapter, we aimed:

1. to characterise the principal networks and investigate their relationship with the well-defined network hubs
2. to explore whether principal network structures are sensitive to pathology in RRMS, PPMS and SPMS.

9.2. Methods

In this study, we used the same cohort and pre-processing and post-processing pipeline as in **chapter 5-6**. Below, we briefly describe the main steps:

9.2.1. Participants

Fifty-one HC (25 male, mean age (± SD) 41 ± 13 years), 58 RRMS (18 male, mean age 42 ± 10 years), 28 PPMS (10 male, mean age 52 ± 9 years) and 36 SPMS (8 male, mean age 57 ± 7 years) underwent MRI assessment. Demographics of the participants are summarised in **Table 9.1.** This work has been approved by the local institutional ethics committee and written consent was obtained from all the patients.

9.2.2. MRI data acquisition

MRI data were acquired on a Philips Achieva 3T MR scanner (Philips Healthcare, Best, Netherlands) with a 32-channel head coil using: (1) 3D sagittal T1-weighted scans with a fast-field echo scan, (2) whole brain HARDI scan with echo planar imaging consisted of a cardiac-gated SE sequence and (3) dual-echo proton density/T2-weighted axial oblique-scans.

9.2.3. Structural imaging processing

A non-rigid transformation was performed to register the subject's non-filled T1-weighted bias-field corrected image to the corresponding diffusion-weighting image (DWI) using BrainSuite v.15b (Bhushan et al., 2012). The target volume was the first b0 image after DWI pre-processing, resulting in a structural image of resolution 2x2x2 mm^3. T2-hyperintense lesions were manually delineated from the PD-T2-weighted scans using JIM (v6.0, Xinapse Systems, Aldwincle, UK), non-rigidly transformed to DWI space and then filled the T1-weighted images using a modality-agnostic patch-

based method. The filled T1-weighted images were then segmented into different tissue types and parcellated according to Desikan–Killiany–Tourville atlas protocol using GIF (Cardoso et al., 2015).

9.2.4. Diffusion-weighted imaging processing

The 7 b0 images were rigid registered to the 61 DWI correcting for eddy current, head motion (Andersson and Sotiropoulos, 2016) and EPI distortions (Bhushan et al., 2012). We generated 10^7 streamlines implementing the ACT framework (Smith et al., 2012) followed by SIFT2 to modulate the contribution of each streamline to the relevant edge (Smith et al., 2015b).

9.2.5. Network analysis

For the brain network, we defined as nodes the cortical and subcortical regions, and as edges the sum of the weights of streamlines connecting a pair of nodes (Smith et al., 2015b). We generated one brain network per subject and defined hubs as regions that exhibited higher strength (≥ mean + SD) (van den Heuvel and Sporns, 2013). Strength is defined as the sum of all weights connected to the node.

For principal network calculation, we first estimated the mean connectivity matrix for each group (HC, RRMS, PPMS, SPMS) and then derived the first and second principal networks in each group. The default loading threshold of 0.1 was applied. Loadings are the normalised eigenvectors of the association matrix (eigenvectors are special vectors that do not change directions when a linear transformation is applied to them). Their magnitude corresponds to the influence of each node to the principal network and the (relative) sign reflects their influence to the other nodes (i.e. nodes from the left or right hemisphere). Principal network decomposition method is fully supported in TractoR (http://www.tractor-mri.org.uk) (Clayden et al., 2011).

9.2.6. Statistical analysis

Statistical analysis was performed using R software (https://www.r-project.org/ v3.3.0). Student t-test was used to compare nodal strengths between subjects with MS and HC. P-values < 0.05 were considered statistically significant.

9.3. Results

Identification and comparison of network hubs between MS subtypes and healthy volunteers.

Table 9.2 shows the identified network hubs for HC, RRMS, PPMS and SPMS. There were 18 network hubs in both the control and disease groups indicating preserved hub organisation across all groups under investigation. Interestingly, we detected significantly reduced strength in some hubs in MS subtypes while the number of regions with reduced strength increased in more severe phenotypes as the highlighted values show in **Table 9.2**. For instance, in RRMS, 7 hub regions show decreased strength when compared to HC whereas in SPMS 16 out of 18 regions exhibit statistically reduced strength. (**Table 9.2**; $p < 0.05$). Remarkably, deep nuclei are affected in all MS subtypes.

Identification and comparison of the first principal network in healthy controls and MS subtypes

Fig. 9.2A. and **Table 9.3.** demonstrate first principal networks identified in HC. We identified 10 brain regions that composed the first principal network. These regions are a subset of the previously defined network hubs **Table 9.2**. and they include regions from the frontal parietal and subcortical grey matter. Additionally, **Fig 9.2A.** shows that the connectivity of the first principal network comprises but is not limited to inter-hemispheric connections.

We used the same threshold to identify the first principal network in each MS group. In RRMS and PPMS, the first principal network is the same as in the control

group, whereas in SPMS a loss of the right thalamo-cortical connections from this network was detected that resulted in the right thalamus to be excluded as a principal network node (**Fig. 9.2A**. and **Table 9.3.**).

Identification and comparison of the second principal network in healthy controls and MS subtypes

Fig. 9.2B. and **Table 9.4.** show that the second principal network in healthy controls is comprised of 10 brain regions which are very similar to the first principal network with the exception of right Putamen while left Thalamus did not qualify as node in the second principal network. Of note, right Putamen is still identified as network hub (**Table 9.2**). In addition, the second principal network is comprised of regions with strong interhemispheric connections **(Fig. 9.2B.)**.

In all MS subtypes, this network did not include the right putamen compared to healthy controls, while in SPMS group there was an additional loss of the right thalamo-cortical connections (**Fig. 9.2B**).

9.4. Discussion

Network hubs and principal network organisation have been recognised as important features of the brain networks (van den Heuvel and Sporns, 2013; Clayden et al., 2013). In this study, we investigated for the first-time a) how principal network organisation relates to the well-established hub organisation and b) whether principal network organisation is sensitive in RRMS, PPMS and SPMS. Generally, we observed distinct patterns of connectivity which indicates progressive weakening of connections which matched the severity of the MS phenotypes.

Within the framework of network science, nodes that are found to have a central role in the network are generally referred to as network hubs. There are many different graph measures that can be used to derive a network hub, most of which express facets of nodal centrality (van den Heuvel and Sporns, 2013; Yeh et al., 2016). The most commonly used measure is strength (for weighted networks) or degree (for binary networks), which were defined either as the sum of the weights or number of the connections respectively that are linked to each node (van den Heuvel and Sporns, 2011). In this study, we identified 18 hub nodes, including regions from frontal, temporal and parietal lobes and DGM structures. Despite methodological differences that exist between previous investigations and the present study (parcellation schemes and hub definitions) there was a great overlap of areas identified as hub nodes (Shu et al., 2016; Yeh et al., 2016; van den Heuvel and Sporns, 2013).

The relevance of network hubs has been previously studied in MS pathology. In general, network hub distribution is mostly preserved in RRMS compared to the control group (Shu et al., 2016; Llufriu et al., 2017). Here, we report for the first time preserved hub organisation not only in RRMS but also in PPMS and SPMS. Hubs with

decreased strength were detected in all MS subtypes and the reduced strength showed a disease specific pattern. For instance, in RRMS, a condition with little or no tissue loss (Frischer et al., 2009), reduced strength was detected in a subset of hubs when compared to controls whereas in SPMS, which is the condition with the highest neurogenerative component (Calabrese et al., 2015) reduced strength was exhibited in the majority of hubs. Interestingly, deep nuclei atrophy which is known to be the first areas affected in pathology and to drive disability in MS (Eshaghi et al., 2018) showed reduced strength in all MS subtypes.

Principal networks decomposition is a novel technique that allowed us to disentangle the different subnetworks based on brain's internal connectivity (Clayden et al., 2013). Applying this technique to our control data we identified a structural organisation of hub nodes forming the first principal network. Of note, the first principal network includes inter-hemispheric connections whereas the second principal network includes only intra-hemispheric connection while there is a great overlap of nodes in both networks. Functional neuroanatomy studies have demonstrated that one brain region can participate in more than one network. For instance, thalamus acts as a relay area for both motor and limbic circuit (Lapidus et al., 2014). This non-mutually exclusive participation of brain regions in networks can be detected by our technique constituting principal networks decomposition method a biologically relevant approach.

The number of nodes of the first principal network was the same in RRMS and PPMS but less in SPMS. As the exact same criteria were applied to identify principal networks in each of the MS subtypes, the smaller number of nodes in SPMS indicate reduced internal connectivity within that group. Notably, the node that was not included in SPMS was the right thalamus, indicating reduced thalamocortical connections,

which they are known to be affected in pathology especially in more progressive stages (Tovar-Moll et al., 2009).

For the second principal network, the number of nodes was reduced in all MS subtypes compared to controls while in SPMS there was an additional loss of a node from this network. Similar to the first principal network, weaker connections between deep nuclei with cortex in all MS subtypes resulted in the absence of right putamen as a principal network node compared to controls. In the principal network of the most progressive group, there were no deep nuclei nodes due to possibly the weakening of all cortical-subcortical connections (Tovar-Moll et al., 2009; Kipp et al., 2015). In fact, it is hypothesised that thalamic connections are affected due to and through their extensive connections with other brain regions (Kipp et al., 2015; Chard and Trip, 2017), a phenomenon that our technique can capture.

Reduced connection strength in hub nodes and altered principal network organisation in particular suggests widespread brain disconnection. This is consistent with previous studies that showed reduced network efficiencies in MS (Shu et al., 2016; Shu et al., 2011; Rocca et al., 2016; He et al., 2009) and that network disruption is associated with cognitive impairment (Llufriu et al., 2017). Pathological features of disconnection include neuroaxonal damage, inflammation and neurodegeneration (Ciccarelli et al., 2014) while recently GM damage has also been recognised as a pathological feature of MS, although the relationship between GM and WM damage remains to be elucidated (Calabrese et al., 2015).

Our principal network analysis captures the progressive weakening of connections in a layer specific manner. For instance, the first principal network corresponds to the most highly interconnected network and we only identified network changes in the most severe MS subtype. For the second most interconnected network,

we were able to detect connectivity changes between MS and controls. Thus, using our analysis framework we could highlight that disconnection occurs at different layers from the least to the most interconnected network. Based on our findings, we could hypothesise that the higher the severity of the disease, the higher layer of connectivity is affected. Although these findings should be validated to a bigger cohort, we could speculate that principal network analysis holds the potential to provide a connectivity fingerprint for each clinical phenotype.

Another brain organisation feature that has been studied in neurological disorders including MS is the rich-club organisation, that is the tendency of hub nodes to be more interconnected among themselves (van den Heuvel and Sporns, 2011). Disrupted rich-club organisation was reported in Alzheimer's disease (Lee et al., 2018) while decreased strength within rich-club was reported in CIS (Shu et al., 2018) and in PPMS (Stellmann et al., 2017). Recently, it has been demonstrated that there are nodes common to principal networks and to rich-club organisation (Powell et al., 2018), highlighting that there is a subset of nodes with specific role in the network independent of the choice of the decomposition method. Mapping out structural linkages of hub nodes and how these are affected in pathology could serve as a framework to identify disease progression.

Our findings are more of explorative nature and need further validation. There are several measures that can be used to define hubs each of which might influence the results (Rubinov and Sporns, 2010). In our analysis, we used strength as a metric to characterise hubs which is the most commonly used metric although other centrality metrics could be potentially used. Additionally, the nodes of the principal networks do not correspond to the previously reported work (Clayden et al., 2013). This could be accounted to differences in the methodological approach during network

reconstruction. For instance, Clayden et al. (2013) did not include DGM as nodes, which is possible to alter the distribution of streamlines to some nodes. Additionally, in our approach we reweighted the streamlines of the network using SIFT2 (Smith et al., 2015b) which could alter the internal connectivity as the decomposition depends on the applied weighting method. The effect of SIFT2 and other network reconstruction methods on principal network organisation was beyond the scope of this study. Furthermore, tractography method used to reconstruct the brain network shares some inherent limitations (Sotiropoulos and Zalesky, 2017). Especially, WM lesions are known to hamper connectivity and potentially influence the analysis. However, in this study, we used methods that aim to minimise tracking biases (Smith et al., 2012; Smith et al., 2015b), while we made sure that no streamlines were terminated incorrectly into the WM due to the lesions (**chapter 5; Fig. 5.8.**). However, we cannot exclude the possibility that lesions may alter the streamline distribution influencing in part our study outcomes.

The findings presented here could form the basis for future work. Future longitudinal studies could investigate how the patterns of connectivity change over time and if it changes in the same way in all MS subtypes. Moreover, it is hypothesised that hubs and their connections might be particularly vulnerable to pathogenic factors due their central role in the network (Crossley et al., 2014). Thus, future studies could investigate whether there is a higher probability of lesions being present in principal networks and/or whether the presence of lesions in the principal network is more detrimental for accumulation of disability.

9.5. Conclusion

Using a data-driven approach, we demonstrated that network hubs form principal networks that are sensitive to pathology. Importantly, we identified differential patterns of connectivity in MS compared to controls, while the weakening of cortico-subcortical connections was reasonably consistent across the MS spectrum. This technique, which considers multiple “layers” of connectivity separately, provides insights into the progressive reduction of connectivity which matches the severity of the MS phenotypes. Although these are preliminary findings and further is work is needed, we highlight the potential utility of the presented approach as imaging biomarkers for disease progression or treatment effects.

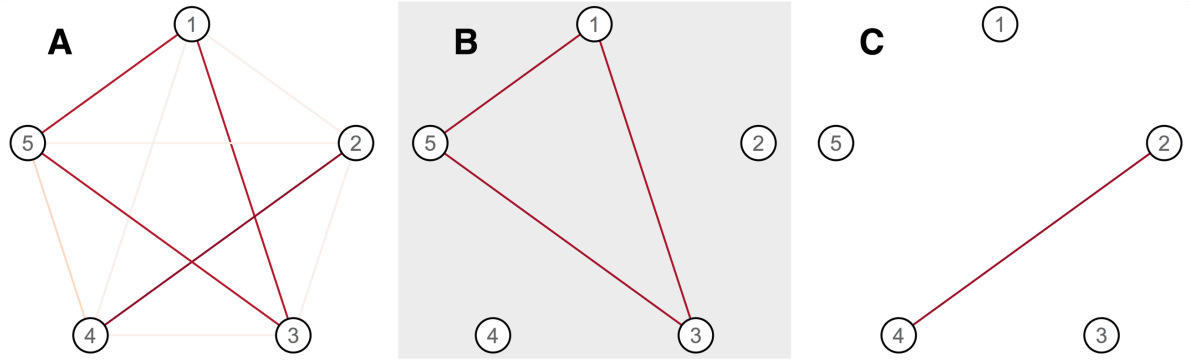

Figure 9.1. Example of a whole network and its decomposed subnetworks

Linear decomposition of the full network **(A)** results in two main subnetworks **(B)** and **(C)** such that the sum of these two subnetworks result in the full network **(A)**. The decomposition occurs based on their internal connectivity (Figure taken from Clayden et al. (2013)).

	HC (n = 51)	MS patients (n = 122)	RRMS (n = 58)	PPMS (n = 28)	SPMS (n = 36)
Age, years	41 ± 13	48 ± 11	49 ±cl 12	46 ± 9	52 ± 9
Gender (M/F)	25/26	36/86	18/40	10/18	8/28
Disease duration, years	-	15 ± 10	11 ± 8	14 ± 7	22 ± 10
EDSS, median	-	5.5 (0-8.5)	2 (0-7)	6 (3-8)	6.5 (4-8.5)
LL (mL)	-	14.37 ± 15.92	12.78 ± 15.72	16.56 ± 19.83	15.23 ± 12.73

Table 9.1. Demographics of the study participants

Abbreviations: HC = Healthy controls; MS = multiple sclerosis; RRMS = relapsing remitting MS; PPMS = primary progressive MS; SPMS = secondary progressive MS

Brain region	HC (x10^5)	RRMS (x10^5)	PPMS (x10^5)	SPMS (x10^5)
Frontal lobe				
Right precentral gyrus	3.39 (0.21)	3.34 (0.27)	3.27 (0.24)	**3.23 (0.23)**
Left precentral gyrus	3.53 (0.23)	**3.38 (0.28)**	**3.36 (0.30)**	**3.34 (0.32)**
Right superior frontal gyrus	3.37 (0.18)	**3.22 (0.23)**	**3.11 (0.26)**	**3.09 (0.25)**
Left superior frontal gyrus	3.28 (0.17)	3.20 (0.26)	**3.10 (0.03)**	**3.13 (0.24)**
Right middle frontal gyrus	2.88 (0.20)	2.78 (0.25)	2.75 (0.23)	**2.58 (0.22)**
Left middle frontal gyrus	3.04 (0.19)	**2.92 (0.27)**	**2.77 (0.23)**	**2.76 (0.22)**
Parietal lobe				
Right postcentral gyrus	2.25 (0.10)	2.28 (0.16)	2.20 (0.16)	2.16 (0.18)
Left postcentral gyrus	2.32 (0.12)	2.27 (0.14)	2.31 (0.19)	2.32 (0.18)
Right superior parietal lobule	2.26 (0.10)	2.21 (0.13)	**2.09 (0.16)**	**2.08 (0.15)**
Left superior parietal lobule	2.01 (0.10)	1.96 (0.12)	1.93 (0.13)	**1.85 (0.11)**
Right precuneus	2.20 (0.10)	2.14 (0.13)	2.10 (0.16)	**1.98 (0.13)**
Left precuneus	2.01 (0.10)	1.95 (0.12)	1.94 (0.13)	**1.85 (0.12)**
Temporal lobe				
Right middle temporal gyrus	2.06 (0.10)	**1.96 (0.13)**	**1.89 (0.12)**	**1.88 (0.12)**
Left middle temporal gyrus	1.85 (0.09)	1.78 (0.12)	**1.73 (0.10)**	**1.74 (0.11)**
Subcortical grey matter				
Right thalamus	2.67 (0.15)	**2.32 (0.02)**	**2.27 (0.19)**	**2.08 (0.15)**
Left thalamus	2.53 (0.15)	**2.22 (0.13)**	**2.23 (0.17)**	**2.06 (0.14)**
Right putamen	2.34 (0.13)	**2.13 (0.12)**	**2.11 (0.02)**	**2.03 (0.13)**
Left putamen	2.20 (0.09)	**2.03 (0.11)**	**2.04 (0.15)**	**1.94 (0.13)**

Table 9.2. Network hubs in healthy controls and multiple sclerosis subtypes

Average values and standard deviations (SD) of region-specific strength

Bold and highlighted values represent regions that exhibit significant decrease in nodal strength against healthy controls. The highlighted and underlined regions indicate regions that are belong to the first and second principal network in healthy controls respectively

Abbreviations: HC = healthy controls; RRMS = relapsing-remitting MS; PPMS = primary progressive MS; SPMS = secondary progressive MS

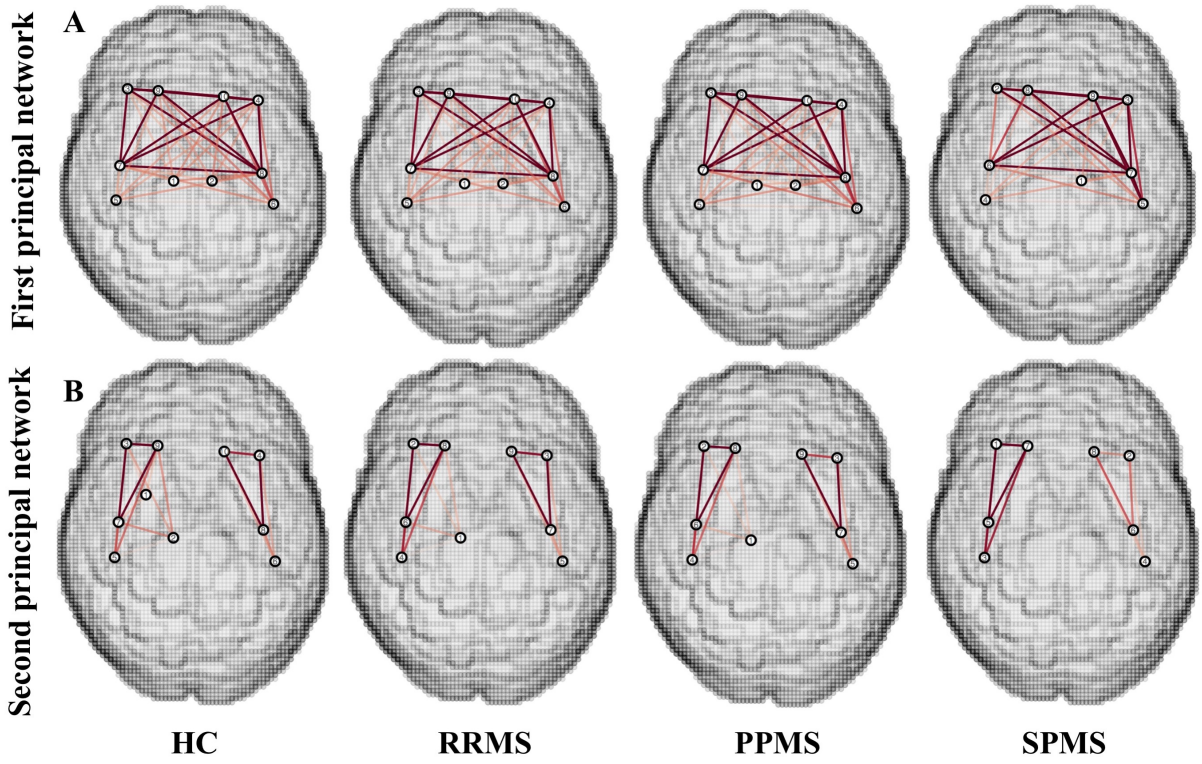

Figure 9.2. The first and second principal network in healthy controls and multiple sclerosis subtypes

(A) There is a loss of the right thalamo-cortical connections in the first principal network in SPMS.

(B) For the second principal network, there is a loss of the right putamen connections in all MS subtypes, and an additional loss of the right thalamo-cortical network in SPMS. Intensity of the edges' colour denotes the strength of the connection.

Abbreviations: HC = healthy controls; RRMS = relapsing-remitting MS; PPMS = primary progressive MS; SPMS = secondary progressive MS

1st principal network nodes			
HC	**RRMS**	**PPMS**	**SPMS**
Frontal lobe			
Right precentral gyrus	Right precentral gyrus	Right precentral gyrus	Right precentral gyrus
Left precentral gyrus	Left precentral gyrus	Left precentral gyrus	Left precentral gyrus
Right superior frontal gyrus	Right superior frontal gyrus	Right superior frontal gyrus	Right superior frontal gyrus
Left superior frontal gyrus	Left superior frontal gyrus	Left superior frontal gyrus	Left superior frontal gyrus
Right middle frontal gyrus	Right middle frontal gyrus	Right middle frontal gyrus	Right middle frontal gyrus
Left middle frontal gyrus	Left middle frontal gyrus	Left middle frontal gyrus	Left middle frontal gyrus
Parietal lobe			
Right postcentral gyrus	Right postcentral gyrus	Right postcentral gyrus	Right postcentral gyrus
Left postcentral gyrus	Left postcentral gyrus	Left postcentral gyrus	Left postcentral gyrus
Subcortical grey matter			
Right Thalamus Proper	Right Thalamus Proper	Right Thalamus Proper	
Left Thalamus Proper	Left Thalamus Proper	Left Thalamus Proper	Left Thalamus Proper

Table 9.3. First principal network nodes in healthy controls and multiple sclerosis subtypes

Abbreviations: HC = healthy controls; RRMS = relapsing-remitting MS; PPMS = primary progressive MS; SPMS = secondary progressive MS

2nd principal network nodes			
HC	**RRMS**	**PPMS**	**SPMS**
Frontal lobe			
Right precentral gyrus	Right precentral gyrus	Right precentral gyrus	Right precentral gyrus
Left precentral gyrus	Left precentral gyrus	Left precentral gyrus	Left precentral gyrus
Right superior frontal gyrus	Right superior frontal gyrus	Right superior frontal gyrus	Right superior frontal gyrus
Left superior frontal gyrus	Left superior frontal gyrus	Left superior frontal gyrus	Left superior frontal gyrus
Right middle frontal gyrus	Right middle frontal gyrus	Right middle frontal gyrus	Right middle frontal gyrus
Left middle frontal gyrus	Left middle frontal gyrus	Left middle frontal gyrus	Left middle frontal gyrus
Parietal lobe			
Right postcentral gyrus	Right postcentral gyrus	Right postcentral gyrus	Right postcentral gyrus
Left postcentral gyrus	Left postcentral gyrus	Left postcentral gyrus	Left postcentral gyrus
Subcortical grey matter			
Right Thalamus Proper	Right Thalamus Proper	Right Thalamus Proper	
Right Putamen			

Table 9.4. Second principal network nodes in healthy controls and multiple sclerosis subtypes

Abbreviations: HC = Healthy controls; RRMS = relapsing-remitting MS; PPMS = primary progressive MS; SPMS = secondary progressive MS

Bibliography

Andersson JL and Sotiropoulos SN. (2016) An integrated approach to correction for off-resonance effects and subject movement in diffusion MR imaging. *Neuroimage* 125: 1063-1078.

Bhushan C, Haldar JP, Joshi AA, et al. (2012) Correcting Susceptibility-Induced Distortion in Diffusion-Weighted MRI using Constrained Nonrigid Registration. *Signal Inf Process Assoc Annu Summit Conf APSIPA Asia Pac* 2012.

Calabrese M, Magliozzi R, Ciccarelli O, et al. (2015) Exploring the origins of grey matter damage in multiple sclerosis. *Nat Rev Neurosci* 16: 147-158.

Cardoso MJ, Modat M, Wolz R, et al. (2015) Geodesic Information Flows: Spatially-Variant Graphs and Their Application to Segmentation and Fusion. *IEEE Trans Med Imaging* 34: 1976-1988.

Chard D and Trip SA. (2017) Resolving the clinico-radiological paradox in multiple sclerosis. *F1000Res* 6: 1828.

Ciccarelli O, Barkhof F, Bodini B, et al. (2014) Pathogenesis of multiple sclerosis: insights from molecular and metabolic imaging. *The Lancet Neurology* 13: 807-822.

Clayden J, Maniega SM, Stokey AJ, et al. (2011) TractoR: Magnetic Resonance Imaging and Tractography with R. *JSS*.

Clayden JD, Dayan M and Clark CA. (2013) Principal networks. *PLoS ONE* 8: e60997.

Crossley NA, Mechelli A, Scott J, et al. (2014) The hubs of the human connectome are generally implicated in the anatomy of brain disorders. *Brain* 137: 2382-2395.

Eshaghi A, Prados F, Brownlee W, et al. (2018) Deep grey matter volume loss drives disability worsening in multiple sclerosis. *Ann Neurol*.

Frischer JM, Bramow S, Dal-Bianco A, et al. (2009) The relation between inflammation and neurodegeneration in multiple sclerosis brains. *Brain* 132: 1175-1189.

He Y, Dagher A, Chen Z, et al. (2009) Impaired small-world efficiency in structural cortical networks in multiple sclerosis associated with white matter lesion load. *Brain* 132: 3366-3379.

Kipp M, Wagenknecht N, Beyer C, et al. (2015) Thalamus pathology in multiple sclerosis: from biology to clinical application. *Cell Mol Life Sci* 72: 1127-1147.

Lapidus KA, Stern ER, Berlin HA, et al. (2014) Neuromodulation for obsessive-compulsive disorder. *Neurotherapeutics* 11: 485-495.

Lee WJ, Han CE, Aganj I, et al. (2018) Distinct Patterns of Rich Club Organization in Alzheimer's Disease and Subcortical Vascular Dementia: A White Matter Network Study. *J Alzheimers Dis*.

Llufriu S, Martinez-Heras E, Solana E, et al. (2017) Structural networks involved in attention and executive functions in multiple sclerosis. *Neuroimage Clin* 13: 288-296.

Powell E, Prados F, Brownlee W, et al. (2018) A Comparison of Subnetwork Classification Methods. *International Society of Magnetic Resonance in Medicine (ISMRM).* Paris, France.

Rocca MA, Valsasina P, Meani A, et al. (2016) Impaired functional integration in multiple sclerosis: a graph theory study. *Brain Struct Funct* 221: 115-131.

Rubinov M and Sporns O. (2010) Complex network measures of brain connectivity: uses and interpretations. *Neuroimage* 52: 1059-1069.

Shu N, Duan Y, Huang J, et al. (2018) Progressive brain rich-club network disruption from clinically isolated syndrome towards multiple sclerosis. *NeuroImage: Clinical* 19: 232-239.
Shu N, Duan Y, Xia M, et al. (2016) Disrupted topological organization of structural and functional brain connectomes in clinically isolated syndrome and multiple sclerosis. *Sci Rep* 6: 29383.
Shu N, Liu Y, Li K, et al. (2011) Diffusion tensor tractography reveals disrupted topological efficiency in white matter structural networks in multiple sclerosis. *Cereb Cortex* 21: 2565-2577.
Smith RE, Tournier JD, Calamante F, et al. (2012) Anatomically-constrained tractography: improved diffusion MRI streamlines tractography through effective use of anatomical information. *Neuroimage* 62: 1924-1938.
Smith RE, Tournier JD, Calamante F, et al. (2015b) SIFT2: Enabling dense quantitative assessment of brain white matter connectivity using streamlines tractography. *Neuroimage* 119: 338-351.
Sotiropoulos SN and Zalesky A. (2017) Building connectomes using diffusion MRI: why, how and but. *NMR Biomed*.
Stellmann JP, Hodecker S, Cheng B, et al. (2017) Reduced rich-club connectivity is related to disability in primary progressive MS. *Neurol Neuroimmunol Neuroinflamm* 4: e375.
Tovar-Moll F, Evangelou IE, Chiu AW, et al. (2009) Thalamic involvement and its impact on clinical disability in patients with multiple sclerosis: a diffusion tensor imaging study at 3T. *AJNR Am J Neuroradiol* 30: 1380-1386.
van den Heuvel MP and Sporns O. (2011) Rich-club organization of the human connectome. *J Neurosci* 31: 15775-15786.
van den Heuvel MP and Sporns O. (2013) Network hubs in the human brain. *Trends Cogn Sci* 17: 683-696.
Yeh CH, Smith RE, Liang X, et al. (2016) Correction for diffusion MRI fibre tracking biases: The consequences for structural connectomic metrics. *Neuroimage* 142: 150-162.

Chapter 10

10. Conclusions and future directions

The overarching aim of this work was to investigate structural network disruption in MS (taking into consideration the different disease subtypes), evaluating the potential of brain network analyses as new biomarkers in MS pathology. This is part of the more general goal of bridging the gap between MRI measures and clinical outcomes providing insights into underlying mechanisms and targeting treatments.

The major contributions of the thesis are summarised below:

Mapping connectomes with diffusion MRI is challenging. In this thesis, we developed and optimised a network reconstruction pipeline applying the latest methodological developments at the time which aimed to reduce some of the reconstruction biases discussed in earlier chapters. One of the limitations addressed in our optimised pipeline, was the improvement of the density of the reconstructed network pathways such that these pathways are more reflective of underlying biological white matter connectivity. This allowed more biologically relevant measures to be obtained. Despite the fact that network quantification is an active area of research and better techniques will be developed, our optimised pipeline was the first to apply these cutting-edge techniques in MS.

A few studies have investigated network disruption in pathology and MS specifically, but none explored the importance of network analysis in predicting disability over the conventional imaging metrics. In this thesis, we showed for the first time that network metrics explain disability better than non-network metrics such as lesion volume and tissue atrophy over and above. More specifically, the best model

for EDSS score showed that reduced network density and global network efficiency and older individuals were associated with increased clinical disability. Additionally, the best model for SDMT score showed that smaller deep grey matter volume, reduced global network efficiency and male gender were associated with worse information processing speed. These promising results highlight the clinical importance of network analysis and the potential of network metrics as biomarkers for disease diagnosis or for assessing treatment effects.

There have been very few longitudinal structural studies of brain networks and none in MS. From a network reconstruction perspective, specific techniques are required that take advantage of the longitudinal design without introducing any potential biases. In this thesis we proposed and validated a longitudinal network analysis pipeline that enables longitudinal studies on structural networks without affecting the derived metrics. Additionally, this pipeline appears sufficiently robust even in the presence of substantial brain abnormalities such as WM lesions. With the increasing need for longitudinal studies, we anticipate that this framework is transferable and will have a wide range of application not only in MS but also in many neurological conditions with imaging data.

Our longitudinal analysis demonstrated that network metrics can predict future tissue damage either at the macroscopic level (increased lesion volume), or at the microscopic level causing deep grey matter volume loss (atrophy). These results highlight the fact that network studies have the potential to be used as predictive markers for disease progression.

Finally, the last chapter demonstrated distinct patterns of connectivity which are indicative of connections weakening linked to the severity of the MS phenotypes. The main strength of this study is the data-driven nature of the network decomposition

method that allows automatic selection of brain regions with high internal connectivity. The results reported in this chapter suggest that connectivity fingerprinting for each phenotype might be possible with potential future application to disease prognosis and diagnosis.

Future directions

The results presented in this thesis form a robust framework that future investigations could build upon. One of the things that could be addressed that is directly related to this thesis is whether subnetwork-specific metrics can relate to disability even more, compared with whole-brain global network metrics and imaging measures. Additionally, for the longitudinal studies, future investigations could study whether subnetwork-specific metrics serve as predictors not only of whole-brain loss but also of more regional tissue atrophy. Finally, it would be of particular importance to study whether the identified principal networks change differently over time in different subtypes. The above investigations would shed light into the clinical importance of network approaches and help to appreciate brain network dynamics over time.

One outstanding question in MS pathology, is why not all MS patients progress at the same rate or convert at the time into the progressive phenotypes. Perhaps future network-based analyses could address this. For instance, longitudinal studies with long follow-up time, could investigate if specific network patterns exist such that disruption of these (due to lesions, neurodegeneration) predispose certain individuals to worsen at a faster rate or convert to more severe phenotypes. These network analyses would help not only to gain insights into the disease processes in order to help develop neuroprotective strategies for the affected individual.

From a methodological perspective, current approaches could be further improved. Algorithms for modelling tissue microstructure, whole brain tractography and brain parcellation belong to some of the research themes that are very active at the moment. Therefore, we anticipate more techniques to be developed that could address some of the limitations discussed in this thesis. In addition, connectivity studies could be validated histologically with post-mortem tissue as this could provide the gold standard for our *in vivo* investigations. Moreover, the application of multimodal approaches is essential to appreciate the pathological substrates of changes in network topology and function. For instance, magnetisation transfer techniques to measure myelin content, sodium imaging to estimate sodium concentration or fMRI to study brain activation either at rest or during task are some of the MRI modalities that could offer complementary information with respect to brain networks and better understand how these are affected in MS.

Final thoughts

Human brain integrity is crucial for normal functioning and human brain pathology can result in a wide range of disorders including MS. Despite its importance, understating brain structure and function has been limited due to the current *in vivo* imaging tools. The efforts in this thesis aim to explore further approaches that could help address clinically relevant questions. We demonstrated that our methods may provide additional information with respect to pathology highlighting the importance of expanding the analyses methods available. We hope that the work here may provide a framework for future work to finally bridge the gap between imaging and symptomatology.